

Università degli Studi di Napoli Federico II
Ph.D. Program in Industrial Products and Processes Engineering
XXXVII Cycle

Thesis for the Degree of Doctor of Philosophy

Nikolaos Kolezakis

Charged Vesicle Gels in Consumer Goods: An Experimental and Numerical Study of Structure, Dynamics, and Rheology

Scuola Politecnica e delle Scienze di Base
Dipartimento di Ingegneria Chimica, dei Materiali e della Produzione Industriale

Charged Vesicle Gels in Consumer Goods: An Experimental and Numerical Study of Structure, Dynamics, and Rheology

Ph.D. Thesis presented
for the fulfillment of the Degree of Doctor of Philosophy
in Industrial Products and Processes Engineering
by

Nikolaos Kolezakis

October 2024

Approved as to style and content by

Advisors: Prof. Gaetano D'Avino, Prof. Pier Luca Maffettone

Co-advisors: Dr. Vincenzo Guida

Università degli Studi di Napoli Federico II
Ph.D. Program in Industrial Products and Processes Engineering
XXXVII cycle - Chairman: Prof. Andrea D'Anna

Candidate's declaration

I hereby declare that this thesis submitted to obtain the academic degree of Philosophiæ Doctor (Ph.D.) in Industrial Products and Processes Engineering is my own unaided work, that I have not used other than the sources indicated, and that all direct and indirect sources are acknowledged as references.

Napoli, December 11, 2024

_____

Nikolaos Kolezakis

Abstract

Liquid formulations like liquid detergents and fabric softeners are of significant interest in the consumer product industry. These products are characterized by the complexity of their composition, which derives from the presence of several additives to enhance user experience. However, this complexity also makes the formulations prone to instabilities that impact both their appearance and performance. Gaining insights into their microscopic dynamics and flow behavior is therefore crucial, as is developing frameworks to model their response to various flows and stresses. Such models are essential for designing formulations with longer shelf-life and enhanced mechanical properties.

The thesis aims to develop a simulation framework that accurately characterizes the rheological behavior of liquid fabric enhancers and link these properties to their microscopic dynamics. To achieve this, we will combine Brownian Dynamics simulations with experimental techniques, such as Differential Dynamic Microscopy and rheometry, to validate our model predictions. This validation will be carried out through various rheological tests, including steady and oscillatory shear flows, as well as shear stress applications. The study will focus on both the basis of fabric enhancers, particularly charged vesicle suspensions, and their mixtures with a non-adsorbing polymer that form the structural network in fabric softeners.

Keywords: Liquid Fabric Enhancer, Brownian Dynamics simulations, rheology, microscopic dynamics

Contents

Acknowledgements

First and foremost, I would like to express my sincere gratitude to my advisors, Gaetano D'Avino and Pier Luca Maffettone, for their expert guidance and support throughout my PhD, as well as their assistance in taking the next step. I am also grateful to Raffaele Pastore and Francesco Greco for their support and valuable insights into my work. Special thanks go to Vincenzo Guida for his help during my secondments in Brussels, but especially during the early stages of my PhD project. I greatly enjoyed my discussions on research and non research topics with Francesco Rusciano.

I am particularly thankful to Paolo Edera and Stefano Aime for their invaluable help with the DDM experiments during my time in ESPCI and beyond. I also appreciate the insightful discussions and assistance from the researchers at Procter & Gamble during my time there.

I would like to extend my gratitude to my colleagues from the YIELDGAP Project, with whom I shared memorable moments during our schools. Many special thanks go to my lab mates for their wholehearted support: Christos, Hongwei, Davide, Stefano, Maurizio, Alie, Shagufta, Claudio, Massimiliano, Marco, Nouman, Lorenzo, Giuseppe, Ciro, Nicola, Igino, Nadia, Ilaria, Annarita, Federica, Michele, Pietro, and Vincenzo.

I would like to truly thank the members of my committee for their evaluation of this thesis.

This project has received funding from the European Union's Horizon 2020 research and innovation programme under the Marie Sklodowska-Curie Grant Agreement No. 955605. I acknowledge the computational resources provided by the IBISCO cluster, and thank Procter & Gamble for kindly providing the materials needed for our experiments.

As a final note, I would like to express my deepest gratitude to my parents, Antonios and Ioanna, as well as my sister Giorgia, for their support and understanding throughout my academic journey.

List of Acronyms

LFE	Liquid Fabric Enhancer
EDL	Electrical Double Layer
BD	Brownian Dynamics
DDM	Differential Dynamic Microscopy
ISF	Intermediate Scattering Function
SISF	Self Intermediate Scattering Function
CISF	Coherent Intermediate Scattering Function
MSD	Mean Square Displacement
LS	Light Scattering
MRI	Magnetic Resonance Imaging
HS	Hard Sphere
std	standard deviation
HI	Hydrodynamic Interactions

List of Figures

List of Tables

Introduction

Liquid fabric enhancers are complex mixtures of charged particles and polymers designed to soften fabrics and add fragrance during the washing process. Due to the large number of additives and their intricate composition, these products pose significant challenges for manufacturers, both in creating formulations, and maintaining their stability throughout their shelf life. As a result, developing simulation frameworks that can accurately model the rheological behavior and yielding properties of fabric enhancers, as well as link these behaviors to their microscopic dynamics, is crucial. This dissertation focuses on addressing this challenge, and it is organized as follows:

In chapter 1, we begin by introducing the yield stress materials and their various applications. We discuss the components of Liquid Fabric Enhancers and the potential instabilities they may face. Additionally, we provide a general overview of colloidal interactions, the phase diagram of colloids, gel microstructure, and their linear mechanical properties. Lastly, we explore the flow behavior and the yielding properties of colloidal depletion gels.

In chapter 2, we describe the materials used in this study, the sample preparation process, and the methods employed. The experimental methods include rheometry and Differential Dynamic Microscopy (DDM), while the computational approach is limited to Brownian Dynamics (BD) simulations. The chapter concludes with potential methods for the analysis of the structure.

In chapter 3, we investigate the microscopic dynamics of charged vesicle suspensions. First, we use simulations to study the impact of parameters

such as volume fraction and ionic concentration on the system's dynamics. Then, we conduct experimental studies using DDM to measure these systems. The DDM analysis yields decorrelation functions across a wide range of wavevectors in concentrated and dilute regimes, providing insights into the different processes involved in the thermal dynamics of vesicles.

In chapter 4, we use BD simulations to track the quiescent evolution of a gel made of charged particles over time. By analyzing various structural and dynamic quantities, we gain information about the gel's morphology, revealing a continuous coarsening process as the system explores lower energy states.

In chapter 5, we present a simulation framework developed to model the rheological behavior of fabric softeners. The model is validated against rheometry data through various tests, including steady and oscillatory shear flows, as well as creep tests. In addition to this validation, we examine how shear rates and stresses affect the gel's morphology, based on the microstructure under different flow conditions.

This dissertation concludes with chapter 6, where we summarize the results of this work.

Chapter 1

Background and related work

The chapter begins by providing information on yield-stress materials, offering insights into their history and diverse applications. Consequently, the industrial system under investigation—a Liquid Fabric Enhancer (LFE)—is introduced, along with a description of the potential instability scenarios it may encounter. The chapter then explores the possible colloidal interactions, phase diagrams, and linear mechanical properties, while also examining the relationship between macroscopic properties and microstructural details. Finally, the yielding and flow behavior of attractive suspensions, which are comparable to LFE formulations, are discussed.

1.1 Yield-stress materials

Yield stress materials are a unique class of materials that exhibit both solid-like and fluid-like behavior depending on the applied stress. These materials remain solid under stresses below a certain threshold, called the yield stress, but flow like a fluid when the applied stress exceeds this critical value. Such behavior is observed in a wide variety of complex fluids, including suspensions, emulsions, foams, and biological tissues, making them essential in both fundamental research and industrial applications. Their distinct rheological characteristics have attracted significant attention in fields such as food processing, cosmetics, pharmaceuticals, construction materials, and even geological phenomena, like landslides and lava flows

[5, 24].

The concept of yield stress was first formalized by Bingham [30], who introduced a simple model known as Bingham plastic to describe materials with a linear relationship between stress and strain rate above the yield point. Since then, more sophisticated models have emerged to better capture the nonlinear and often time-dependent behavior of yield stress materials, including Herschel-Bulkley model and viscoelastic frameworks [40, 64]. These advancements in modeling have been critical for predicting the performance of yield stress materials under various flow conditions, which is crucial for optimizing their use in real-world applications.

In recent years, the study of yield stress materials has expanded to in-

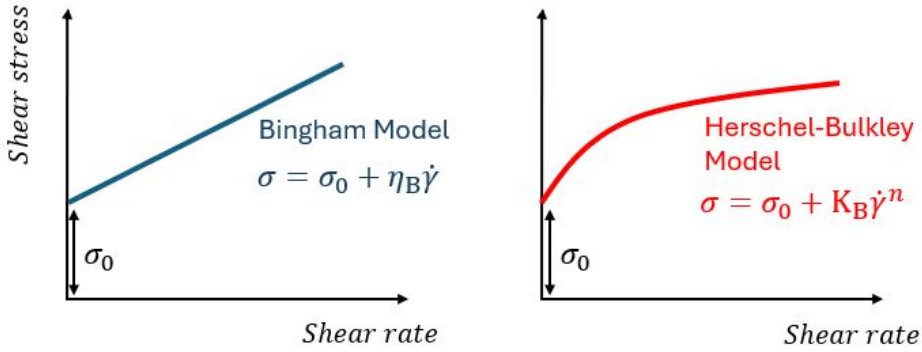

Figure 1.1. Bingham and Herschel-Bulkley constitutive equations.

clude not only traditional yield stress fluids, like pastes and gels, but also more complex materials such as thixotropic fluids and soft glasses [45]. These materials exhibit a wide range of mechanical properties depending on their microstructure and external conditions, including time-dependent phenomena like aging and stress-induced shear banding [9, 32]. Understanding the yield stress behavior at both macroscopic and microscopic scales has become increasingly important for designing materials with tailored properties for specific applications, from 3D printing to biomedical devices [23].

Despite the progress in this field, several challenges remain. One of the main issues is the accurate determination of yield stress, as it is influenced by various factors such as material composition, deformation history, and

the testing method used. Different testing methods can give different values for the yield stress, making standardization difficult. Furthermore, yield stress materials may exhibit unstable or non-homogeneous flow patterns, such as plug flow, where the material can move as a solid block in the center, while the liquid surrounding it moves faster, leading to inefficient and unpredictable flow behavior [24].

1.2 Liquid Fabric Enhancers (LFE) formulation

Yield-stress materials are of particular interest to home-care companies, which dedicate considerable resources into the development of formulated products. In the present study, we are focusing on Liquid Fabric Enhancers (LFEs), which are materials used to deliver active ingredients to fabrics in a controlled and effective manner, often enhancing softness, fragrance, or other desired properties. They are derived from the mixing of charged colloidal particles with soluble polymers. These particles, which are composed of surfactant bilayers are commonly known as *vesicles* [37]. Solutions of vesicles form the basis for numerous products in fabric care and healthcare industries, mainly because of their encapsulating properties. They can be used as carriers for drugs or other substances, depending on the solvent they are dispersed into [96, 17]. During the washing process, vesicles interact with fabric surfaces, and their amphiphilic nature allows them to adhere to dirt and fabric fibers, solubilizing hydrophobic dirt by surrounding and encapsulating it.

Our vesicles have a wide size distribution (polydispersity), and are dispersed into water and salt. The amphiphilic molecules composing the vesicles are made of charged headgroups, causing dissociation of the charged species when placed into water, and, in turn, the formation of an Electrical Double Layer (EDL) around the vesicles' circumference [3]. This specific type of vesicular suspension forms the foundation of LFEs, and is industrially known as *white base*.

In a fabric enhancer, we also incorporate non-adsorbing linear polymer chains into the charged vesicle solution. This addition induces depletion-attractive interactions between the vesicles, leading to particle aggregation, and, ultimately resulting in the formation of a space-spanning gel network. This network is responsible for the stability of the final product,

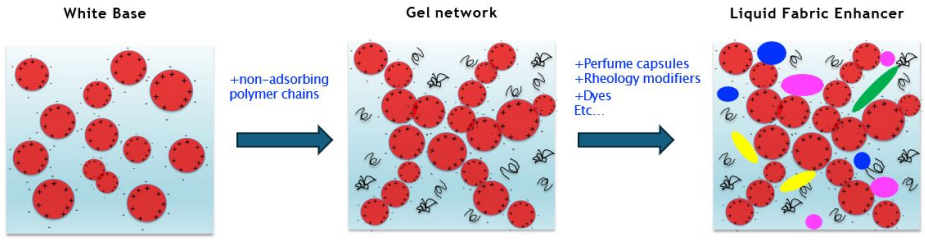

Figure 1.2. Schematic representation of the added components until the derivation of the final product.

as it holds in place and homogeneously distributes throughout the solution many other components added into a fabric enhancer. These components include perfume microcapsules, liquid crystals, rheology modifiers, dyes, halide salts, as well as entrapped air bubbles. Together, they improve the properties of the final product, such as the solubility in the washing machine, the appearance, the aroma, the fabric texture, and overall the consumer experience.

1.3 LFE instabilities

A fabric enhancer, however, can experience different types of instabilities. The most common one is *phase separation*, where the liquid phase, consisting of the solvent and the polymer, is visually distinguished from the gel phase. This can happen when there are large density differences between the continuous and the vesicular phases. In this scenario, gel compression and collapse cause the two phases to layer on top of each other, a phenomenon explained by the balance between gravitational and elastic forces [61]. According to the poro-elastic model, gravity compresses the colloidal gel, forcing the continuous phase out via filtration flow. The same type of failure mode (*poroelastic compression*) can occur when the gel is subjected to excessive weight. If the gel network's elastic modulus is insufficient to support the added components that are incorporated into an LFE, the gel may eventually collapse in a sponge-like way.

The presence of air bubbles can also have an effect on the stability of an LFE. Thompson et al. [91] investigated the differences in phase separation

Figure 1.3. Vials of gels followed through time lapse photography over a period of one month. The particle volume fractions (DPV) and the polymer concentration (C_p) are reported below each image, which are labeled according to their instability.

between aerated and non-aerated samples in density matched suspensions. The instability mechanism associated with air bubbles is called *tunneling*, and it includes the movement of air bubbles within the gel network, when the buoyancy force that dictates their motion, exceeds the yield stress of the network. Vesicle-poor regions are formed at the wake of the rising bubbles, leading to local density differences. It was found that in the presence of air bubbles, phase separation occurs rapidly, following poroelastic consolidation and is driven by density differences between the bubbles and the surrounding fluid. On the other hand, in the absence of air bubbles, phase separation is a slow process due to small density differences between the vesicles and the continuous phase. In this case, phase separation can be described as viscoelastic, where the volume-shrinking of the transient gel is most likely driven by the depletion attraction between the vesicles [89, 52].

In the system without bubbles, Magnetic Resonance Imaging (MRI) [91] showed that phase separation begins with very small vesicle-poor regions forming in the sample. This type of instability represents the last one presented here, and it is usually mentioned in the literature as *cracking*. These local vesicle-poor regions within the gel network can be either vertical or horizontal and they are influenced by the interplay between gravity,

viscous drag, and attractive forces within the gel. In MRI [91], they started appearing on the sample way before phase separation becomes visually detectable, and their formation, close to the container walls, is consistent with volume shrinking of the gel [89, 52].

Designing and manufacturing these complex materials with the appropriate rheological properties, such as yield stress, viscosity, or gel network elasticity is vital for ensuring their stability throughout shelf life. Therefore, it's crucial to understand their microscopic dynamics and how these are connected to the rheological behavior of LFEs, as well as develop a framework to effectively monitor this rheological response. By achieving these objectives, we can improve the design and production of liquid formulations with extended shelf life.

1.4 Colloidal interactions

The type of interactions between colloidal particles significantly influences their structural arrangement, which in turn affects the rheological properties of the materials composed of these particles. For instance, van der Waals forces lead to the formation of strong, rigid bonds [68]. On the other hand, depletion attractions create flexible bonds that continuously break and reform due to thermal fluctuations, like in our materials. In this section, we will explore the various types of inter-particle interactions that can be met in fabric enhancers, such as van der Waals, electrostatic, and depletion forces.

1.4.1 Van der Waals interactions

Van der Waals or dispersion interactions are short-range attractive forces that arise from the polarization of atoms in one colloidal particle by the atoms in another [64]. The magnitude of this interaction between two particles, each with a radius R, as a function of the center-to-center distance r, can be determined using the following equation:

$$U_{vdw}(r) = -\frac{AR}{(r-2R)} \tag{1.1}$$

where A represents the Hamaker constant, material-specific property influenced by the polarizability of both the particles and the solvent. It can be approximated using the following formula [41, 54]:

$$A = \frac{3}{4} k_B T \left(\frac{\epsilon_p - \epsilon_s}{\epsilon_p + \epsilon_s} \right)^2 + \frac{3 h v_e}{16\sqrt{2}} \frac{(n_p^2 - n_s^2)^2}{(n_p^2 + n_s^2)^{3/2}} \tag{1.2}$$

where the subscripts p and s refer to the particle and solvent, respectively. Here, ϵ is the dielectric constant, n stands for the refractive index, h is the Planck's constant and v_e is the ultraviolet absorption frequency. The attractive potential that arises from these interactions often leads to particle aggregation, destabilizing the colloidal suspension—a phenomenon typically considered undesirable. To prevent coagulation, particles must be stabilized by introducing a repulsive force that serves as a barrier to aggregation. This repulsion can be achieved through either electrostatic stabilization, which utilizes electrical charges, or steric stabilization, which depends on the configurational entropy of polymers.

1.4.2 Electrostatic interactions

Colloidal particles in a polar medium can acquire charge through various mechanisms, including surface acid-base reactions, adsorption of free ions, or surfactant adsorption. In the bulk of the solution, ions are uniformly distributed, but counterions with charges opposite to that of the particle accumulate near the particle's surface. A stationary layer of these counterions forms what is called the Stern layer. Beyond this, a diffuse layer of counterions extends outwards, where the ion concentration gradually decreases with distance from the particle's surface. Together, these layers make up the electrostatic double layer. When the electric double layers of two particles come into contact, a repulsive force is generated. The potential of this electrostatic repulsion can be calculated as follows [82]:

$$U_{el}(r) = \frac{4\pi\epsilon_r\epsilon_0 R^2 \psi_s^2}{r} exp[-k(r - 2R)] \tag{1.3}$$

where ϵ_0 is the permittivity of free space, ϵ_r is the relative dielectric constant, ψ_0 is the surface potential, and k is the inverse of Debye screening

length which is calculated as follows:

$$k^{-1} = \sqrt{\frac{\epsilon_r \epsilon_0 k_B T}{2 N_A e^2 I}} \tag{1.4}$$

with k_B being the Boltzmann's constant, T the absolute temperature, e the elementary charge, N_A the Avogadro's number, and I the ionic strength of the electrolyte. The Debye length provides a useful estimation for the thickness of the diffuse layer. According to eq. 1.4, the screening length is inversely related to the square root of the concentration of ions. As a result, the thickness of the diffuse layer can be adjusted by varying the ionic concentration.

1.4.3 DLVO theory and Electrostatic stabilization

A theory known as DLVO theory, developed by Derjaguin [26] and independently by Verwey et al. [95], explains the total interaction potential between two charged particles as the sum of van der Waals attraction and electrostatic repulsion resulting from the overlap of their double layers. Consequently, the overall DLVO potential is the combination of equations 1.1 and 1.3 . This combined potential creates a positive energy barrier, as shown in fig. 1.4. If the barrier height exceeds a few $k_B T$,

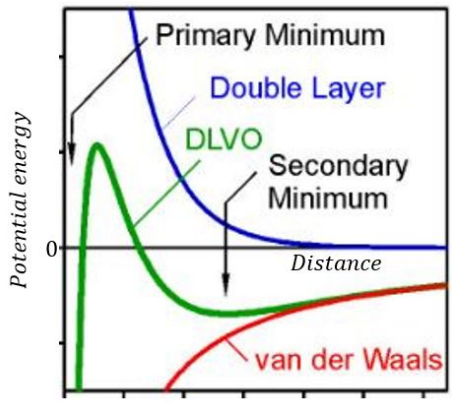

Figure 1.4. Potential energy as a function of distance for the DLVO potential as a linear combination of van der Waals attraction and electrostatic repulsion.

particles are prevented from coming close enough to feel the attractive forces, keeping the dispersion stable. This interaction can be adjusted by introducing salt or surfactant into the suspension, which screens the electrostatic interactions. By adding sufficient electrolyte, the electrostatic repulsive barrier diminishes, allowing van der Waals force to become dominant.

1.4.4 Depletion-attraction interactions

Depletion interactions occur between colloidal particles, when a smaller species, such as smaller hard/soft spheres or a non-adsorbing polymer, is introduced into the suspension [2]. As illustrated in fig. 1.5(a), adding the depletant creates an excluded volume around each particle, with a size roughly equal to the radius of gyration (R_g) of the depletant, within which the depletant cannot penetrate. When two particles approach each other and their excluded volumes begin to overlap, the total free volume available to the depletant increases, resulting in an increase of their entropy. Consequently, configurations where the excluded volumes overlap are en-

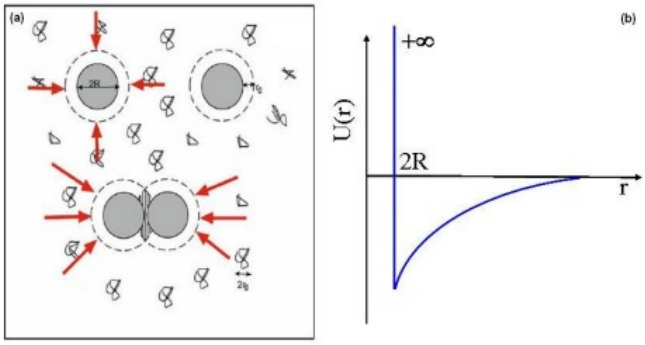

Figure 1.5. (a) Schematic representation of the excluded volume and osmotic pressure applied on the colloidal particles, (b) Asakura and Oosawa potential as a function of the interparticle distance.

tropically favored, leading to an attractive force between the particles. This effect can also be explained by considering the osmotic pressure of the depletant. When a single particle is surrounded solely by the polymer, the depletant exerts isotropic pressure on the particle's surface. However,

when particles come close enough for their excluded volumes to overlap, a region forms between them where the depletant cannot access, causing a higher concentration of depletant around the particles compared to the space between them. This difference creates an anisotropic osmotic pressure, resulting in an attractive depletion force that draws the particles together.

The attractive potential generated by depletants can be derived from the idealized model proposed by Asakura and Oosawa [1, 2]. This model assumes that there are no direct interactions between the particles or between the particles and the polymers. It predicts the effective attractive potential between colloidal particles as follows:

$$\frac{U_{dep}(R)}{k_B T} = \begin{cases} +\infty & r \leq 2R \\ -\frac{\Pi}{k_B T} V_{overlap}(r) & 2R < r \leq 2R(1+q_s) \\ 0 & r > 2R(1+q_s) \end{cases} \tag{1.5}$$

where Π is the osmotic pressure of the polymer solution, q_s is the attraction range where in the ideal theory is reduced to size ration $\xi = R_g/R$, which is the ratio of the polymer to the colloid radius. The depletion potential is illustrated in figure 1.5(b). The overlap volume between colloids is determined by the geometric overlap volume of two spheres and can be expressed as:

$$V_{overlap}(r) = \left[1 - \frac{3r}{4R(1+\xi)} + \frac{1}{2}\left(\frac{r}{2R(1+\xi)}\right)^3\right] \frac{\pi}{6}\left[2R(1+\xi)\right]^3 \tag{1.6}$$

Pressure is calculated by treating the polymer as an ideal gas. In this case, the polymer pressure depends on the concentration of the polymer in the free volume, denoted as c_p^{free}, and is calculated using the following formula [1]:

$$\frac{\Pi}{k_B T} = \left(\frac{4}{3}\pi R^3\right)^{-1} \int_0^y \frac{\partial \Pi}{\partial y} dy \tag{1.7}$$

with $y = \frac{c_p^{free}}{c_p^*} = (c_p/c_p^*)/\alpha$, where c_p is the polymer concentration (g/ml) and $c_p^* = \frac{3M_w}{4\pi N_A R_g^3}$, the overlap concentration of the polymer coils. The α parameter is the ratio of the free volume available for the polymer to the

total volume ($V_{free} = \alpha V$ given by Aarts et al. [1]):

$$\alpha = (1 - \phi)exp[-(Ad + Bd^2 + Cd^3)] \tag{1.8}$$

$$A = 3q_s + 3q_s^2 + 3q_s^3 \tag{1.9}$$

$$B = \frac{9}{2}q_s^2 + 2q_s^3 \tag{1.10}$$

$$C = 3q_s^3 \tag{1.11}$$

$$d = \frac{\phi}{1 - \phi} \tag{1.12}$$

For ideal polymers, considering the interactions between polymer coils, the range of attraction and the derivative of polymer pressure are calculated as follows [1]:

$$q_s = \left(1 + \frac{6}{\sqrt{\pi}}\xi + 3\xi^2\right)^{1/3} - 1 \tag{1.13}$$

$$\frac{\partial \Pi}{\partial y} = \xi^{-3} \tag{1.14}$$

In the semi-dilute regime, the generalized free volume theory (GFVT) [33] provides more precise results by accounting for the compression of the depletion zone around each particle in such solutions and incorporating non-ideal effects into the polymer osmotic pressure. This theory calculates the variations in the interaction range and polymer pressure as follows [33]:

$$q_s = 0.865\left(\frac{\xi}{\sqrt{1 + 3.95y^{2\gamma}}}\right)^{0.88} \tag{1.15}$$

$$\frac{\partial \Pi}{\partial y} = \xi^{-3}[1 + 3.77y^{3y-1}] \tag{1.16}$$

with γ being the de Gennes exponent, equal to 0.77.

1.5 Phase Diagram

1.5.1 Glass transition of HS systems

A fundamental soft matter model system consists of suspensions of hard spheres, where the particles undergo Brownian motion and interact solely via a hard-core excluded volume interaction [78]. These particles do not experience any attraction or long-range repulsion. As a result, the free energy and, consequently, the phase diagram, are entirely governed by entropy, which depends on the particle volume fraction, $\phi = (4/3)\pi R^3\rho$. Here, R represents the particle radius, and ρ denotes the particle number density. Based on the volume fraction, the suspension of hard-spheres can exhibit different responses, from liquid-like behavior ($\phi < 0.494$) to coexisting fluid and crystalline phases ($0.494 < \phi < 0.545$) with the crystallites becoming more and more compact until they reach a maximum close packed configuration at $\phi = 0.74$. These are the so called equilibrium

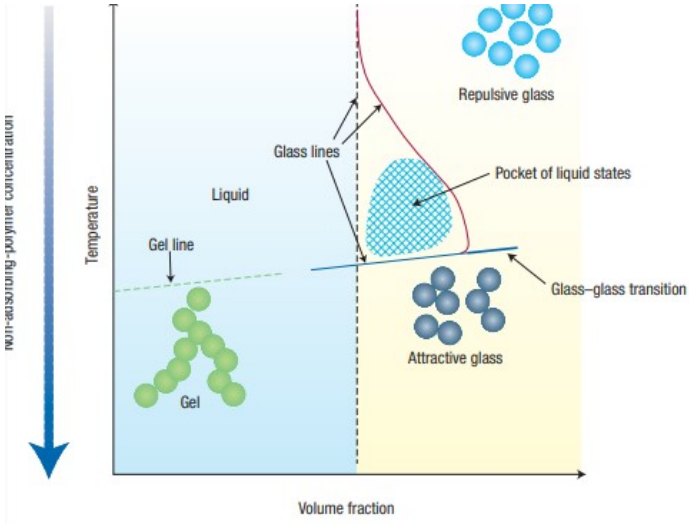

Figure 1.6. Phase diagram of HS system depicting the attractive and repulsive glass transitions. Adapted from Sciortino [83].

phases. However, hard sphere systems can also display non-equilibrium behavior. When the particles volume fraction exceeds $\phi = 0.58$, crys-

tallization is halted, and the particles become confined by their neighbors, only able to rattle within these "cages", while long-range movement beyond cages is restricted. This metastable, kinetically arrested state is referred to as the glass, with $\phi = 0.58$ representing the glass transition volume fraction. This state endures until ϕ reaches approximately 0.64, known as the random close-packed volume fraction, which is the highest density that hard spheres can achieve without forming a crystalline structure.

In the glassy state, where particles are confined by their neighbors, they can only move within their cages, with displacements typically limited to about $10 - 20\%$ of their size. This maximum displacement is known as the localization length or cage size. Now, let's consider the influence of a short-range attractive interaction in addition to the hard-core repulsion. Figure 1.6 illustrates this effect, revealing new and unexpected characteristics, as predicted by mode coupling theory (MCT) [7, 25, 31], numerical simulations [76, 99], and confirmed experiments [28, 72, 74]. At high particle volume fractions, two distinct glassy states are identified. At high temperatures, where attractive forces are negligible, a repulsive glass forms. At low temperatures, a different type of glass, known as attractive glass, appears. Between these two glassy states, at intermediate temperatures, a reentrant pocket of liquid states is found, occurring at higher ϕ compared to a hard sphere (HS) glass. Upon cooling, some particles begin to cluster, creating space for others to diffuse, causing the material to melt. However, further cooling results in most particles becoming confined within the attractive range, slowing down the system's dynamics and leading to another structural arrest called attractive glass. In contrast to the entropy-driven arrest of repulsive glass, the structural arrest in attractive glass is driven by energy. The interplay between these two glasses results in reentrance in the glassy phase diagram.

1.5.2 Gelation

At volume fractions below the glass transition and with sufficiently high polymer concentrations, mixtures of particles and polymers form gels, consisting of particle networks that extend throughout the volume and are capable of supporting their own weight, even with low particle packing fractions. In the case of strong attractions and very small ϕ, gelation occurs through diffusion-limited cluster aggregation (DLCA) of fractal clusters of

colloidal particles [13, 98]. At weaker attraction strengths, a homogeneous fluid phase separates into coexisting gas (colloid-poor) and liquid (colloid-rich) phases, where the particles in both phases remain ergodic. However, as the attraction strength increases, the dense phase becomes arrested in a non-equilibrium glassy state. Various mechanisms have been proposed to explain gelation, including percolation [36, 86], mode coupling theory (MCT) for attractive glasses [8], cluster MCT [14], fluid-crystal transition [78], spinodal-induced gelation [93], viscoelastic phase separation [89], and bond-arrested phase separation [60]. Two main classes of colloidal gels have been proposed: "equilibrium gels", which form without phase separation, and gels formed through spinodal decomposition, leading to an arrested glass phase at high volume fractions [60].

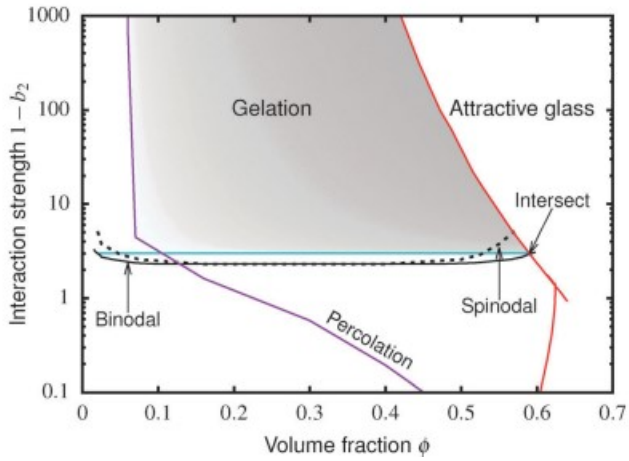

Figure 1.7. Phase diagram of non-crystallizing particles with short-range attractions in reduced second virial coefficient (β_2) - particle volume fraction (ϕ) space. Adapted from Harich et al. [39].

1.6 Gel microstructure

Before discussing the rheology of colloidal gels, it is essential to understand their microstructure in a quiescent state, as the mechanical properties are directly linked to structural details. Therefore, we begin by ex-

plaining the influence of interparticle potential on the microstructure. Figure 1.8 presents two-dimensional confocal images of the structure at different attraction strengths. At the lowest polymer concentration (fig. 1.8(a)), the suspension consists of dispersed, mobile particles. As the attraction increases, mobile clusters form, coexisting with free particles (fig. 1.8(b)). With further increases in polymer concentration, the clusters become less mobile, eventually forming a network of clusters (Fig. 1.8(d)-(g)). In this regime, large-scale motion is arrested, and significant voids or inhomogeneities develop. The structure with the largest clusters and voids occurs at $c_p/c_p^* = 0.46$. Beyond this polymer concentration, the heterogeneity decreases, resulting in more homogeneous structures. Structural analysis reveals that maximum heterogeneity is observed at the gelation point [27, 51, 56].

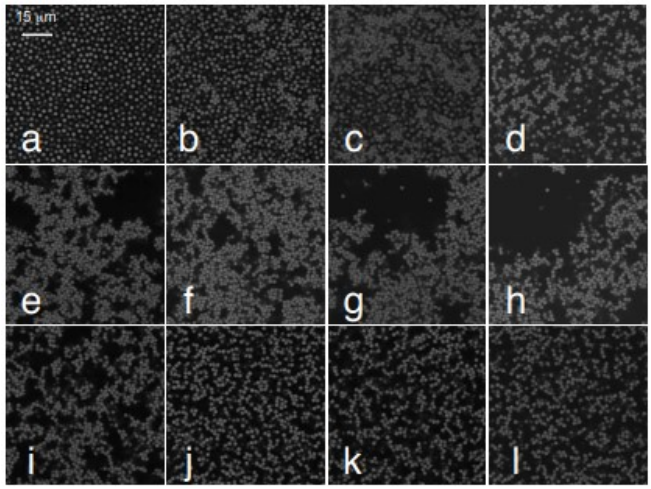

Figure 1.8. Confocal images of a colloidal suspension with particle volume fraction $\phi = 0.2$ and varying depletant concentration c_p/c_p^* = (a)0.15, (b)0.21, (c)0.26, (d)0.31, (e)0.33, (f)0.37, (g)0.41, (h)0.46, (i)0.49, (j)0.64, (k)1.03, (l)1.54. Adapted from Dibble et al. [27].

1.7 Rheology

1.7.1 Linear viscoelastic response

The linear viscoelastic behavior of colloidal gels formed by short-range attractions depends on several factors, including the particle volume fraction, the strength and range of the attractions, and the quality of the solvent, as these variables significantly influence the structural details of the gels. In addition to these thermodynamic factors, the pre-shear history and the waiting time (aging) after ceasing shear or cooling the gel from the liquid state are crucial in determining the mechanical properties of these out-of-equilibrium materials. This section provides a detailed review of experimental studies and theories that predict the elasticity of colloidal depletion gels.

Effect of particle volume fraction

Koumakis and Petekidis [49] investigated the linear viscoelastic properties of attractive suspensions by varying the particle volume fraction (ϕ) while keeping the attraction strength constant. Their study ranged from an attractive glass at $\phi = 0.6$ to a low volume fraction cluster fluid at $\phi = 0.2$. Since the attraction strength was held constant, their research reveals the direct effect of particle volume fraction on the viscoelastic characteristics of attractive colloids (fig. 1.9(a)). At low volume fractions, the behavior resembles that seen with low polymer concentrations, such as the crossover between G' and G'', which indicates the formation of a transient gel network with structural relaxation times observable within the experimental time window. For $\phi > 0.3$, the system displays a solid-like response with no detectable relaxation time within the measurement period. In this regime, G' increases slowly with the frequency, and G'' reaches a minimum. The elastic modulus G' grows with the volume fraction according to two distinct patterns depending on ϕ, as illustrated in fig. 1.9(b). At lower ϕ, the increase in G' follows an exponential trend, characteristic of cluster liquids or transient gel networks [56]. For $\phi > 0.3$, the elastic modulus G' is described by $G' = (\phi_{RCP} - \phi)^{\nu}$, similar to hard spheres (HS) glasses, where the power-law exponent ν shows weak frequency dependence, ranging from 2.4 at low frequencies to to 2.1 at higher frequencies, which is

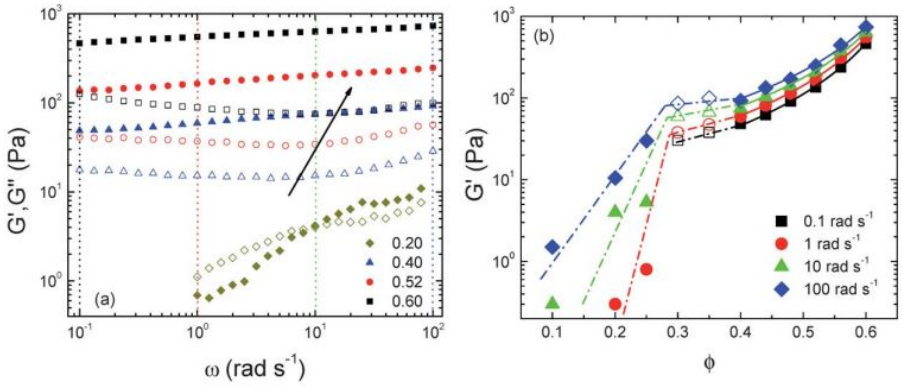

Figure 1.9. Dynamic frequency sweeps for four different volume fractions of equal attraction strength, i) 0.20, ii) 0.40, iii) 0.52, iv) 0.60, with G' as solid and G'' as open symbols. The arrow notes the direction of the minimum of G''. (b) Values of G' as a function of volume fraction at $\omega = 0.1, 1, 10$ and $100 rad/s$ specified by the vertical dashed lines in (a). Solid lines ($\phi = 0.40$ to 0.60) are fits to $G' = G_0(\phi_{RCP} - \phi)^{-c}$. Dash-dot lines are guides for the eye. Adapted from Koumakis and Petekidis [49].

lower than the value of approximately 4 observed for hard sphere glasses [50]. At lower ϕ, the elastic modulus can be represented as $G' = (\phi_{gel} - \phi)^{\delta}$, where ϕ_{gel} denotes the gel transition volume fraction [92].

Effect of attraction strength

The influence of attraction strength on the linear viscoelastic properties of colloidal gels has been extensively reviewed in studies by Laurati et al. [56], Ramakrishnan et al. [81], and Shah et al. [86]. Here, we summarize the key findings from Laurati et al. [56], who conducted a systematic investigation into how attraction strength affects the rheological properties of a gel with an intermediate volume fraction of particles (ϕ=0.4). Their results, illustrated in fig. 1.10, reveal that for polymer concentrations less than $c_p/c_p^* < 0.2$ (where c_p is the polymer concentration and c_P^* the overlap polymer concentration), the system exhibits a viscous response, with the viscous modulus G'' exceeding the elastic modulus G' across all frequencies. The low-frequency behavior of the moduli resem-

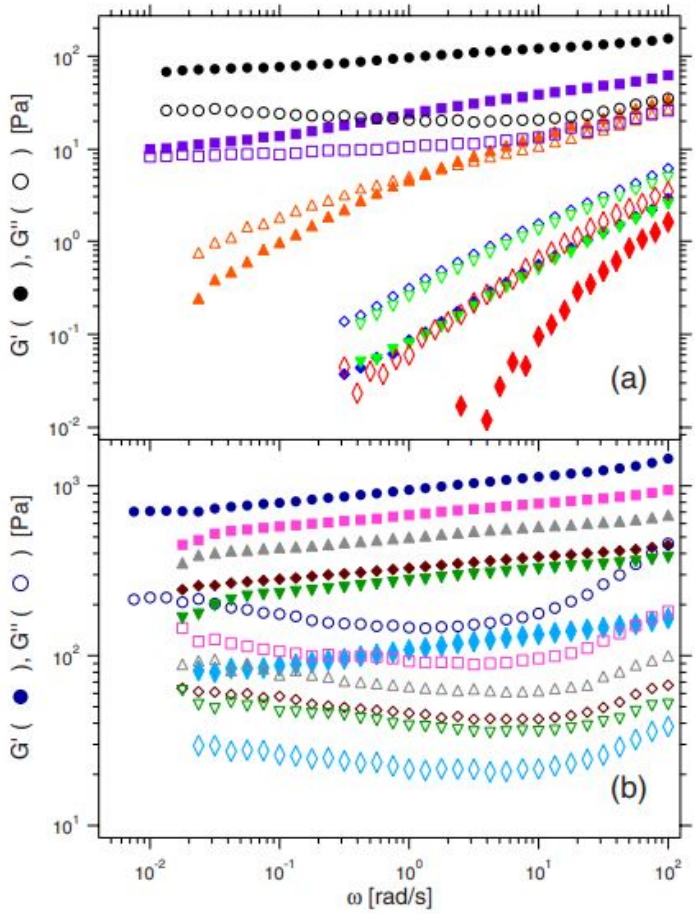

Figure 1.10. Dynamic Frequency Sweeps with elastic modulus G' (filled symbols) and loss modulus G'' (open symbols) as function of frequency. (a) Samples below the macroscopic gelation boundary ($c_p/c_p^* = 0.4$), (b) samples above the gelation boundary. $c_p/c_p^* = 0(\blacklozenge), 0.1(\blacktriangledown), 0.2(\blacklozenge), 0.25(\blacktriangle), 0.32(\blacksquare), 0.4(\bullet), 0.5(\blacklozenge), 0.7(\blacktriangledown), 0.8(\blacklozenge), 1.0(\blacktriangle), 1.5(\blacksquare)$, and $2(\bullet)$. Adapted from Laurati et al. [55].

bles that of simple hard spheres with no interactions, where $G'' \sim \omega$ and $G' \sim \omega^2$. As the polymer concentration increases to $0.25 < c_p/c_p^* < 0.4$, a crossover between G' and G'' is observed, shifting to lower frequencies

with higher c_p. This crossover signifies the development of a percolated gel network with structural relaxation times within the experimental time window. This crossover frequency corresponds to a characteristic time, known as the "bond" lifetime, which represents the duration particles need to overcome their interparticle attractions. In the gel region ($c_p/c_p^* \geq 0.5$), the elastic modulus G' exceeds the viscous modulus G'' across the entire frequency range, indicating the formation of a network with structural relaxation time out of the experimental time frame. In this regime, G' shows only a slight increase with frequency, while G'' reaches a minimum. This minimum has been linked to a transition from α to β relaxation, according to the MCT approach, or to the characteristic time a particle requires to explore its cage [49]. Increasing c_p or decreasing the particle volume fraction [49] shifts this minimum to lower frequencies, thus extending the time scales. As the system approaches the gelation boundary ($0.25 < c_p/c_p^* < 0.4$), G' increases rapidly with c_p, following a power-law with an exponent ranging from 6.2 to about 8.3 at decreasing frequencies. However, within the gel region ($c_p/c_p^* \geq 0.5$), G' increases linearly with polymer concentration, indicating that the elasticity in the gel regime is primarily governed by the strength of the attractions.

Effect of attraction range

Experimental studies on colloidal gels and attractive glasses indicate that increasing the range of attraction leads to a decrease in both the elastic modulus G' and the viscous modulus G'', which suggests the formation of weaker materials [49, 86]. This effect has been anticipated by MCT-PRISM calculations for colloidal gels [19]. The theory predicts a scaling of G' with the localization length as $G' \sim r_{loc}^{-2}$, where $r_{loc} \sim \xi R$. Thus, as the attraction range ξ increases, particles become less localized, leading to a reduction in the elastic modulus. Alternatively, for a constant attraction strength, a larger range of attraction ξ results in a decrease in the attractive force between particles, as represented by $F_{dep} = -\frac{dUdep}{dr}$.

Effect of aging

The life cycle of a colloidal gel can be divided into three stages [103]: the first is gelation, or the formation of the gel; the second is aging, where

the gel undergoes mechanical or structural changes; and finally, the failure or collapse of the gel network, often referred to as its "death". After shear is stopped or the gel is quenched from its equilibrium liquid state, significant structural changes occur over time due to bond formation, leading to gel coarsening. As a result, the rheological properties of colloidal gels are expected to vary over time. The process by which colloidal gels age has been a long-standing issue in materials science. However, it is widely accepted that aging is driven by thermal motion as the system explores minimum energy landscapes [70, 42, 103].

Zia et al. [103] demonstrated that aging and coarsening occur as individual particles migrate along the surface of the gel network. Coarsening follows a three-step process: first, particles move along the network surface and bond with neighboring particles (cage building); next, they travel between cages (cage hopping); and finally, they become embedded within the network strands (cage trapping). This complex interaction between bond kinetics, particle dynamics, and microscopic structure is closely linked to the macroscopic mechanical properties of colloidal gels. Coarsening leads to an increase in the elastic modulus over time, as demonstrated in both experimental studies [4, 51, 49] and simulations [103]. Drawing from the Rouse model and its previous application to reversibly networked polymer chains, Zia et al. [103] derived an analytical expression that relates the age-dependent stiffening in linear rheological response to the dominant network size, a key microscopic structural property. $L_s(q)$ which corresponds to the length scale set by the peak of the static structure function (fig. 1.11), grows over time as a result of the coarsening process.

$$G' \sim G'' \sim (\omega R^2/D)^{0.5} L_{s(q)} \tag{1.17}$$

According to this model, the dominant length scale is the sole structural parameter responsible for the age-related increase in elasticity. As a result, when both the elastic and viscous moduli at any given age are scaled by the dominant length scale at that age, all curves collapse into a single universal curve, regardless of the gel's age (fig. 1.12).

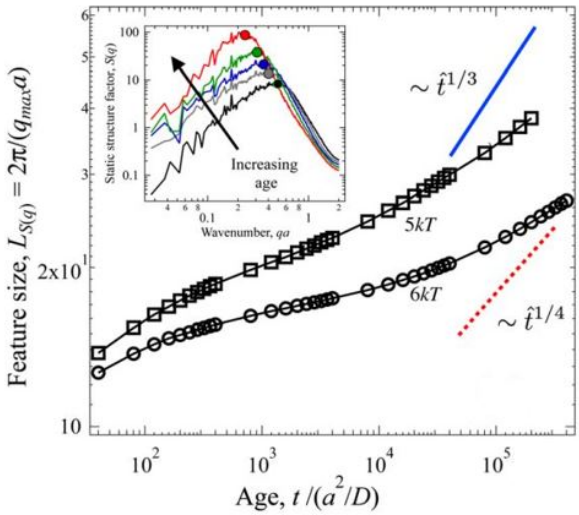

Figure 1.11. Coarsening with age. The dominant structural length scale set by the peak of the static structure factor (inset) as a function of gel age for the $5kT$ and $6kT$ gels. Power-laws correspond to bulk diffusion ($\hat{t}^{1/3}$) and surface migration $\hat{t}^{1/4}$. Adapted from Zia et al. [103].

1.8 Yielding and flow behavior

Colloidal glasses and gels are considered as soft-solid materials. However, under high enough stress or shear rate, they yield and flow often in multiple steps due to the existence of spatial heterogeneities [18, 46, 49, 55, 71, 87], which results in flow-induced structural anisotropy [94], thixotropy, and aging [9]. In this section, we will explain the transient and steady state shear flow response of glasses and colloidal gels in both start-up and oscillatory shear flow, as well as their behavior during creep tests.

1.8.1 Start-up shear flow response

In start-up shear flow, a constant shear rate is applied, and the stress is measured as a function of time or accumulated strain. As depicted in fig. 1.13, hard sphere (HS) repulsive glasses exhibit a single stress over-

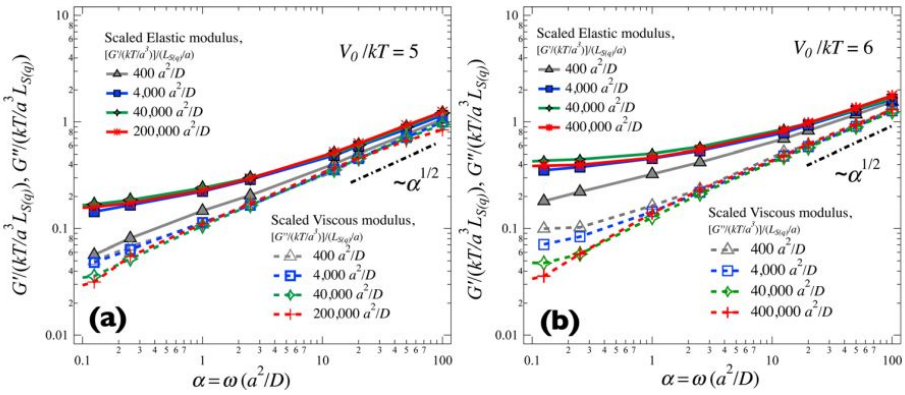

Figure 1.12. Scaling of linear-response elastic moduli with the dominant structural length scale at each age, plotted over a range of frequencies for (a) $5kT$ and (b) $6kT$ gel. Solid lines/filled symbols: Elastic modulus. Dashed lines/open symbols: Viscous modulus $G''/(kT/\alpha^3)$. Adapted from Zia et al. [103].

shoot, indicative of one-step yielding. For HS glasses, the stress response is attributed to an elastic energy storage mechanism that increases stress up to the peak, followed by a dissipative energy release mechanism after the peak, leading to shear-induced flow and structural anisotropy [47, 48]. This anisotropy appears along the extensional axis, where the pair-distribution function reaches a minimum during the stress overshoot.

In contrast, both attractive glasses [49] and colloidal gels [49, 55] display two distinct peaks, as shown by the vertical arrows in fig. 1.13. In the case of attractive glasses, the first yield is associated with bond breaking on a short length scale, while the second yield is linked to the rupture of the cages. For colloidal gels, the first yield corresponds to the breaking of bonds connecting clusters, and the second yield involves breaking the clusters into smaller fragments [49, 55].

Despite these theoretical insights, direct observations confirming this microscopic behavior in attractive suspensions are still lacking. Experimental imaging of the transient response of colloidal gels during start-up shear flow, particularly using rheo-confocal microscopy, remains challenging due to significant wall-slip issues [4]. Brownian dynamics (BD) simu-

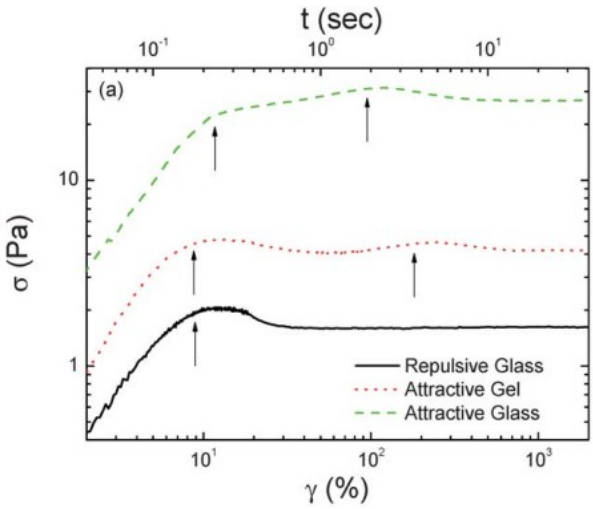

Figure 1.13. Step rate experiments showing stress response as a function of strain/time performed at a shear rate of $0.5s^{-1}$ for a repulsive glass of $\phi = 0.60$, an attractive glass at $\phi = 0.60$, and a gel at $\phi = 0.44$ with attraction strength at contact $U_{dep}(2R) = -23.5k_BT$. Arrows indicate single and double yielding for repulsive and attractive glass/gel, respectively. Adapted from Koumakis and Petekidis [49].

lations offer an incomplete picture, detecting only a single yielding process [49, 43]. However, in the case of attractive glasses, BD simulations successfully capture two stress peaks, consistent with experimental observations across a wide range of attraction strengths and shear rates. Colloidal gels, due to their highly heterogeneous structure, exhibit a variety of structural transformations under shear, resulting in diverse mechanical properties, as evidenced by both experiments and simulations [51, 44].

At high shear rates, gel structures experience significant cluster breakup, while at low shear rates, shear-induced cluster densification occurs, as observed in bulk systems [4, 51, 102], two-dimensional systems [63], and microchannel flows [21]. These shear-induced structural changes have a significant impact on yield stress, viscoelastic moduli [51, 87, 67], delayed yielding [53, 59], slip [4], and even collapse of the gel network [84].

1.8.2 Oscillatory shear flow response

Similar to the start-up shear flow, dynamic strain sweep experiments on colloidal gels and attractive glasses also reveal two-step yielding, evidenced by two distinct peaks in the loss modulus (G'') (fig. 1.14) [49, 55, 87]. It's worth noting that hard spheres (HS) glasses exhibit a complex response to oscillatory shear flow, which varies depending on the frequency of oscillation. At certain frequencies, HS glasses also undergo two-step yielding. The first step is related to cage escape assisted by Brownian motion, while the second is due to shear-induced collisions [47].

For monodisperse particles, under specific conditions of frequency and

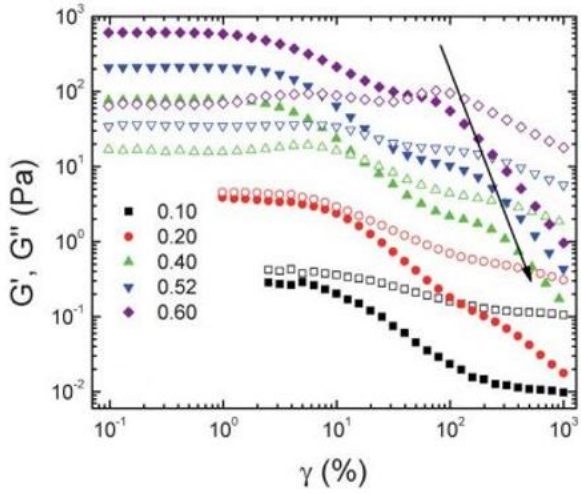

Figure 1.14. Dynamic strain sweep at $\omega = 10 rad/s$ for five different volume fractions with equal attraction strength as indicated. The arrow shows the approximate shift of the second G'' peak with decreasing volume fractions. Adapted from Koumakis and Petekidis [49].

strain amplitude, oscillatory shear flow in HS glasses and colloidal gels can induce shear-driven crystallization, as the shear helps particles find their minimum energy configurations [50]. In attractive suspensions, such as silica suspensions [79], and microgel particles [87], oscillatory shear flow significantly affects the elastic modulus (G') after shear cessation, depending on the preshear strain amplitude [65].

1.8.3 Creep tests

In a creep test, a constant shear stress σ is applied and the evolution of the strain $\gamma(t)$ or the creep compliance $J(\Delta t) = \frac{\gamma}{\sigma}$ are probed over time. Moghimi et al. [66] investigated the macroscopic deformation of a depletion gel subjected to a step shear stress, where three different regimes emerged, depending on the magnitude of the applied stress: i) for stresses below the yield stress, the gel undergoes a weak creep with a sublinearly increasing bulk deformation, while for stresses above the yield stress, the sublinear deformation growth gives way to a superlinear increase, which signals the onset of yielding. However, the long-time creep exhibits two distinct behaviors: ii) under strong stresses, a viscous flow is reached, indicative of the complete yielding and flow of the gel, while iii) under weak stresses, after yielding, the gel starts to resolidify [53].

Figure 1.15 presents these regimes based on different levels of applied

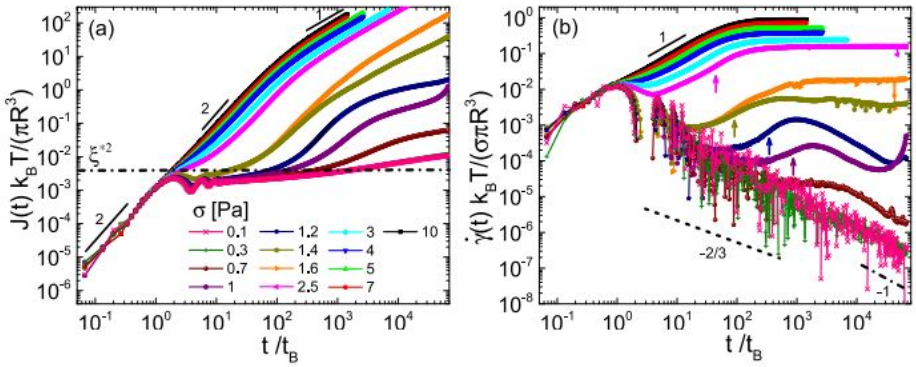

Figure 1.15. (a) Creep compliance and (b) the shear rate as a functin of time at different applied shear stresses as shown in the legend. Results are for the gel with $\phi = 0.3$, $U_{dep}(2R) == 12.7k_BT$ and $\xi^* = 0.058$. The gel has been shear rejuvenated with $\gamma_0 = 1000\%$ and $\omega = 10rad/s$ and aged for the duration of 1000s before the stress application. Adapted from Moghimi et al. [66].

stress. In the creep compliance plot, the yield stress corresponds to the stress value, at which the curves begin to diverge, indicating a shift from linear to nonlinear behavior. The sharp increase in creep compliance marks the onset of gel yielding, while a linear time dependence suggests viscous

flow. Similarly, in the rate of deformation plot, a decrease over time reflects solid-like creeping behavior, which transitions to a change in slope, marking the yielding point, when the applied stress exceeds the yield stress. A constant rate of deformation indicates viscous behavior, while a decrease following the plateau signals the resolidification process.

Creep tests, along with start-up shear flow measurements, can be used to estimate the yield stress of our materials, a critical property of our LFEs, as previously stressed. In the same work by Moghimi et al. [66], the results from both types of measurements were plotted together (fig. 1.16). Above the dynamic yield stress, determined from the plateau value of the flow curve at low shear rates, the gel exhibits viscous behavior. In this regime, the steady state values from both creep tests (steady state shear rate response) and constant shear rate measurements (steady state shear stress response) collapse with one another. Between the dynamic yield stress and the yield stress predicted by the creep tests, the gel eventually undergoes resolidification. Finally, at lower stress levels, the solid-like deformation will never transition to yielding.

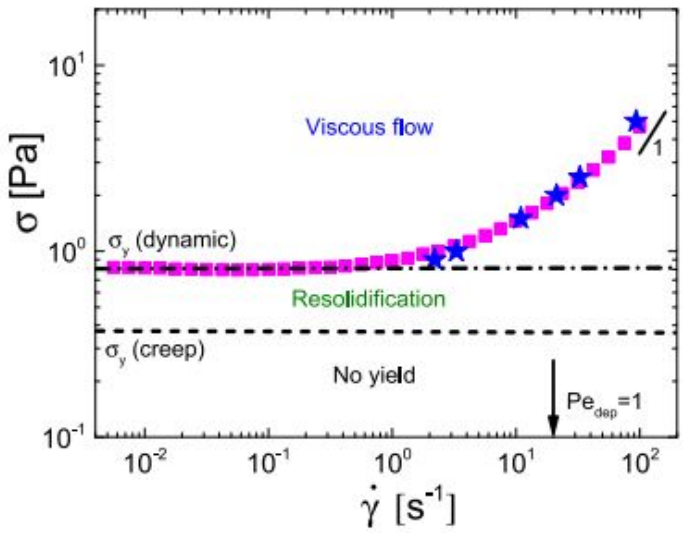

Figure 1.16. Steady state shear stress as a function of the applied shear rate (pink squares). Blue star symbols are the steady state values taken from creep experiments. The horizontal dashed-dotted line shows the dynamic yield stress (the stress plateau) whereas the dashed line represents the yield stress measured from creep experiments. Results are for the gel with $\phi = 0.3$, $U_{dep}(2R) = -5.7k_BT$, and $\xi^* = 0.09$. Adapted from Moghimi et al. [66].

Chapter 2

Materials and methods

This chapter examines the materials and methods used in both experiments and simulations to study the dynamics and rheology of LFEs. It provides detailed information on the experimental techniques employed, such as rheometry and Differential Dynamic Microscopy, as well as the models and methods implemented in our simulations.

2.1 Materials

We used vesicular dispersions, where vesicles are spherical particles composed of surfactants organized into bilayers, creating an onion-like morphology. These dispersions are composed of the cationic surfactant diethylester dimethylammonium chloride, which is made of ionized headgroups resulting in the formation of EDLs around the vesicles' circumference. A visual representation of how surfactants construct a vesicle is given in figure 2.1. These dispersions are polydisperse, encompassing a wide range of sizes, with particle diameters approximately ranging from $0.1\mu m$ to $10\mu m$. The particles are dispersed in water with a fixed ionic concentration of $450ppm\ CaCl_2$. Although vesicles are generally rigid structures, the presence of EDLs softens their interactions. Additionally, they have the ability to encapsulate significant amounts of the surrounding solvent, which in this case is water. The pure vesicle solutions, also referred to as *white bases*, form the basis of LFEs, and they are repulsive systems. Depletion attractions are achieved by adding non-adsorbing lin-

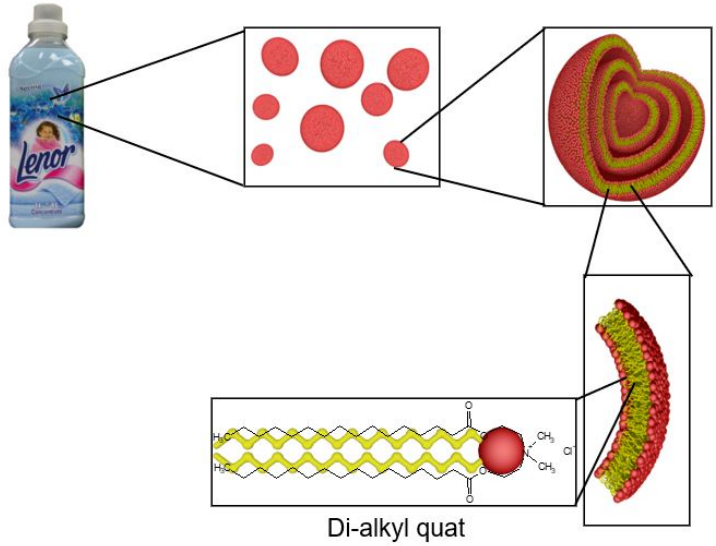

Figure 2.1. Schematic representation of the morphology of a vesicle and the type of the surfactant used.

ear chains of a copolymer with molecular weight $M_w = 150\ 000 gr/mol$, and radius of gyration $R_g = 40nm$. This copolymer consists of the monomers acrylamide, which contributes the hydrophylic and neutral properties, and DMA3 (dimethylaminoethyl methacrylate), which provides cationic sites, making the copolymer capable of interacting with negatively charged substances.

2.2 Sample preparation

The white bases were prepared at different surfactant concentrations, corresponding to different particle volume fractions. A 13% w/w aqueous dispersion of vesicles of a double-tailed cationic surfactant (diethylesterdimethyl ammonium chloride, diC18:0 DEEDMAC, mol wt = 697.5), in presence of 450 ppm of calcium chloride, was prepared according to an extrusion process with an apparatus similar to the one described by

Corominas et al. [22]. This mother dispersion is then isotonically diluted and the samples at $0.1, 1, 4, 6$, and $11\%wt/wt$ are obtained. The vesicle volume fraction that corresponds to each surfactant concentration was calculated by *Procter & Gamble* with a custom method involving a device called Float-A-Lyzer according to the method described by Seth et al. [85]. This device is a type of dialysis tool that separates the components of a solution based on their molecular size. It features a semi-permeable membrane that allows smaller molecules (salts, small ions, or water) to pass through, while retaining larger particles (vesicles) within the chamber. By measuring the volume of the vesicle suspension before and after dialysis, as well as a few other parameters of our systems, the particle volume fraction in the concentrated vesicle samples can be estimated. The corresponding particle volume fractions are $0.4, 0.5$, and 0.55, for the $4, 6$, and $11\%wt/wt$ dispersions, respectively. For the samples with the polymer, based on the desired attraction strength between the particles, we added the analogous quantity, following fig. 2.2. In particular, we selected a polymer level of $1.6\%wt/wt$ to induce weak and reversible bonds in our solution, allowing us, at the same time, to maintain particle connectivity. This concentration corresponds to a minimum attraction energy of approximately $-4k_BT$ in the total potential [41].

2.3 Rheology

Rheology is the study of deformation and flow of materials in response to an applied stress or strain. Ideal solids exhibit a spring-like, elastic response, storing energy in the process. In contrast, liquids dissipate energy through viscous flow. However, for more complex viscoelastic materials, the behavior can be both solid-like and liquid-like. This dual nature depends on the experiment's time scale and the material's structural relaxation time.

Materials exhibit displacement d when subjected to an external force (fig. 2.3). Consider two parallel plates separated by a simple liquid layer of thickness h. If these plates are moved relative to each other at velocity v by a force F, Newton's law states that the resulting shear stress $\sigma(=F/A)$ is proportional to the shear strain rate $\dot{\gamma}(=v/h)$. The constant of propor-

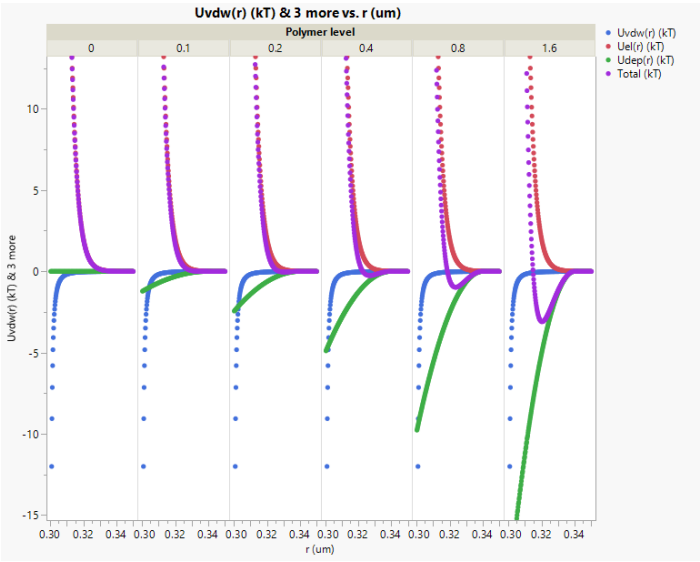

Figure 2.2. Potential energy as a function of particle distance for the potentials derived from the van der Waals, electrostatic repulsive and depletion attractive potentials. The total potential is derived from the superposition of the aforementioned. On top of each plot the corresponding polymer level in $\%w/w$ is reported. Data provided by *Procter and Gamble*.

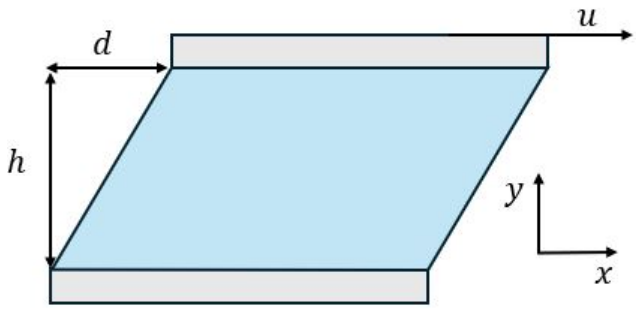

Figure 2.3. Schematic representation of shear deformation.

tionality is called dynamic viscosity η:

$$\eta \equiv \frac{\sigma}{\dot{\gamma}} \tag{2.1}$$

On the other hand, when a shear stress is applied to an ideal solid, it causes an instantaneous deformation d/h. Once a certain strain is achieved, no further movement occurs, but the deformation remains as long as the stress is maintained. According to Hooke's law, the shear stress is proportional to the strain ($\gamma \equiv d/h$), with the proportionality constant known as the shear modulus G:

$$G \equiv \frac{\sigma}{\gamma} \tag{2.2}$$

The rheological behavior of a system can be characterized by measuring the rate of deformation (steady measurements) or by determining the shear modulus as a function of frequency (dynamic measurements). Another method to investigate the rates of structural rearrangements within a complex dispersion, without significantly deforming the fluid's microstructure, is to apply small amplitude oscillatory shear. This type of deformation can be achieved using cone and plate geometries, where one plate is rotated around its axis with an angular velocity that oscillates periodically, defined as $\Omega = \Omega_0 \sin(\omega t)$, with ω being the frequency of oscillation in radians per second. The resulting shear rate $\dot{\gamma}$ is a sinusoidal function of time, given by $\dot{\gamma} = \frac{\Omega r}{h}$, leading to a shear strain $\gamma = \frac{\Omega_0 r}{\omega h} \sin(\omega t) = \gamma_0 \sin(\omega t)$, where $\gamma_0 = \frac{\Omega_0 r}{h}$ represents the strain amplitude. Cone and plate geometries are commonly used to ensure a uniform shear rate throughout the sample.

If the strain amplitude γ_0 is kept sufficiently small to avoid disrupting the structure, the stress observed during oscillatory deformation reflects the rate of spontaneous rearrangements or relaxations occurring in the dispersion's quiescent state. The shear stress $\sigma(t)$ generated by this small amplitude deformation is proportional to the applied strain amplitude γ_0 and varies sinusoidally over time. Generally, this sinusoidal stress can be expressed as:

$$\sigma(t) = \gamma_0 [G'(\omega) \sin(\omega t) + G''(\omega) \cos(\omega t)] \tag{2.3}$$

where G' is the storage modulus and G'' the loss modulus. The storage modulus G' reflects a material's elastic properties, while the loss modulus G'' indicates its capacity to dissipate energy. A solid-like response is observed when $G' > G''$, whereas a liquid-like response dominates when $G' < G''$. Soft solid materials typically show $G' > G''$ within the experi-

mental time window, with the storage modulus increasing gradually with frequency, while the loss modulus exhibits a minimum, as noted by Mason and Weitz [62]. In contrast, a liquid-like response is well described by the simple Maxwell model, which accurately captures the linear viscoelastic behavior. In this model, the storage modulus scales with frequency as $G' \sim \omega^2$, and the loss modulus scales as $G'' \sim \omega$. The crossover frequency ω_c, where $G' = G''$, marks an internal long time relaxation process within the system. The low-frequency liquid-like region, where G' and G'' follow these power laws, is known as the terminal regime.

To quantify the impact of shear on colloidal systems, a dimensionless number called the Peclet number is introduced. This number describes the relative importance of the applied shear rate compared to Brownian motion. The Peclet number, $Pe = \dot{\gamma}\tau_B = \dot{\gamma}R^2/D$, is defined as the product of the shear rate $\dot{\gamma}$ and the Brownian time $\tau_B = R^2/D$, which represents the time required for a particle to diffuse over a distance equal to its own size. For dilute suspensions, the Brownian time τ_B can be expressed as $\frac{6\pi\eta R^3}{k_B T}$, leading to $Pe = \dot{\gamma}\frac{6\pi\eta R^2}{k_B T}$.

In concentrated suspensions, hydrodynamic interactions reduce the short-time self-diffusion coefficient compared to that in the dilute regime, depending on the particle volume fraction (as described by Sierou and Brady [88]). Since the actual Brownian time of the sample influences all other relevant timescales, it is crucial to account for hydrodynamic effects when examining the influence of shear. Thus, we distinguish between two types of Brownian times and Peclet numbers. The "bare" Peclet number refers to the dilute regime, where Brownian time can be calculated using the particle radius and solvent viscosity. The "dressed " Peclet number accounts for hydrodynamic interactions between particles, reflecting the reduced short-time self-diffusion coefficients $D_s(\phi)$. While calculating the bare Peclet number is straightforward, determining the dressed Peclet number requires understanding how $D_s(\phi)/D_0$ varies with the particle volume fraction ϕ. In our BD simulations, which will be discussed in the following section, we use the bare dimensionless numbers referring to the dilute regime. However, when comparing simulations with experimental data, we apply shifting factors to account for the effects of hydrodynamic interactions.

Experimental setup for rheometry

In our rheological measurements, we used an Anton-Paar MCR302 rheometer with cone-plate geometry (50mm and 0.01 rad angle). All measurements were conducted at $T = 20°C$ using a Peltier system. A solvent trap was employed during the experiments to prevent solvent evaporation.

2.4 Differential Dynamic Microscopy

Differential Dynamic Microscopy (DDM) is a powerful analytical technique used to study the dynamics of microscopic particles in a sample, by analyzing fluctuations in the intensity of light scattered by the sample over time [16]. DDM combines the principles of dynamic light scattering (DLS), and microscopy. Below, we outline the series of steps involved in a DDM analysis, accompanied by the typical workflow (fig. 2.4), which visually illustrates these steps.

We start by capturing a sequence of images of our sample using a microscope at specific acquisition rate. Each image gives an intensity signal $I(\mathbf{x}, t) = I_{BG}(\mathbf{x}) + \delta i(\mathbf{x}, t)$ acquired at time t, with $\delta i(\mathbf{x}, t)$ the scattered light due to temporal and spatial fluctuation of the particles, and $I_{BG}(\mathbf{x})$ the contribution from the time-independent background. In order to eliminate the effect of the static background and bring the particles into light, we calculate the image difference:

$$\Delta I_n(\mathbf{x}, \Delta t) = I(\mathbf{x}, t_n) - I(\mathbf{x}, t_n + \Delta t) \tag{2.4}$$

However, the limited spatial resolution of the optical microscope, making difficult to distinguish objects that are very close to one another, does not allow for a simple analysis of the signal in direct space. Due to this reason, we calculate the Fourier power spectrum of each image difference and successively average over all the results obtained with the same time delay Δt, but different initial times t_n. The result of this average is the image structure function $D(\mathbf{q}, t)$:

$$D(\mathbf{q}, \Delta t) = \left\langle \mid \hat{I}(\mathbf{q}, t + \Delta t) - \hat{I}(\mathbf{q}, t) \mid^2 \right\rangle \tag{2.5}$$

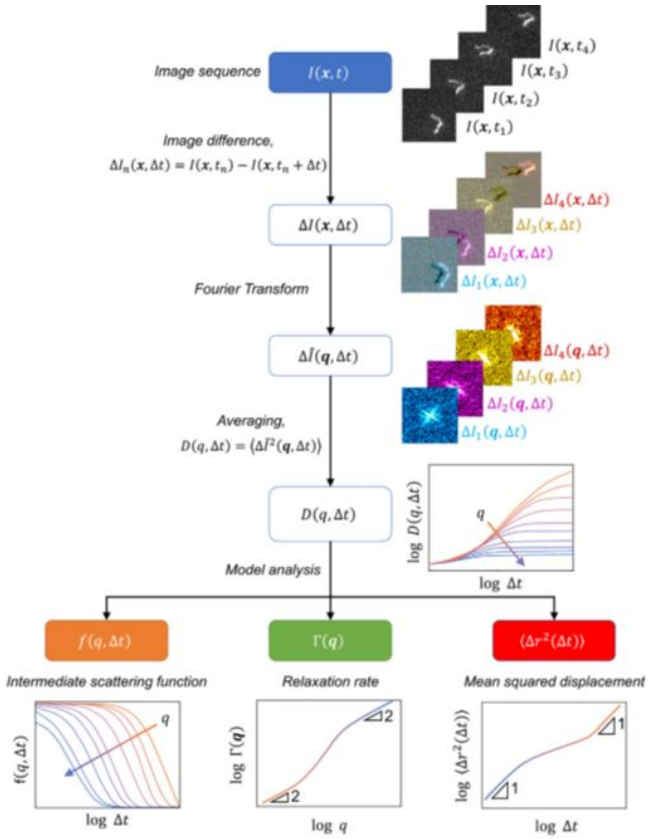

Figure 2.4. Typical workflow for DDM analysis of image sequences. Adapted from Cerbino et al. [15].

where $\hat{I}(\mathbf{q},t) = FFT\{I(\mathbf{x},t)\}$ is the Fast Fourier Transform of the image at time t, $\mathbf{q}$ is the wavevector, and the symbol $\langle\cdot\rangle$ indicates an average over the initial time t. This calculation is iterated for all time delays Δt that are needed to properly follow the sample relaxation. The interpretation of the results is based on the fact that $D(\mathbf{q},t)$ can be written in terms of the real part $f(\mathbf{q},\Delta t)$ of the intermediate scattering function (ISF), which is the quantity encoding information on the relaxation of the density Fourier modes, and whose squared amplitude is typically measured with

DLS experiments:

$$D(\mathbf{q}, \Delta t) = A(\mathbf{q}) \left[1 - f(\mathbf{q}, \Delta t)\right] + B(\mathbf{q}) \tag{2.6}$$

where $A(\mathbf{q})$ is an amplitude term that depends on the spatial intensity correlations present in the images, $B(\mathbf{q})$ accounts for the noise of the detection chain, and $f(\mathbf{q}, \Delta t)$ represents the intermediate scattering function. Starting from equation 2.6, the usual strategy in DDM analysis is based on assuming a suitable functional form describing the time dependence of $f(\mathbf{q}, \Delta t)$, and then through a fitting procedure, derive the q-dependent parameters $A(\mathbf{q})$ and $B(\mathbf{q})$, since the image structure function $D(\mathbf{q}, t)$ is already known. However, in our case, the functional form of the $f(\mathbf{q}, \Delta t)$ is not known *a priori*, but rather than it should be extracted from equation 2.6. Therefore, we first calculate the parameters $A(\mathbf{q})$ and $B(\mathbf{q})$ in a way described below [29].

As already mentioned, the amplitude term $A(\mathbf{q})$ is influenced by the scattering properties of the sample, while the additive term $B(\mathbf{q})$ accounts for the noise in the detection chain. Since $f(\mathbf{q}, \Delta t \to 0) = 1$, $B(\mathbf{q})$ could theoretically be estimated as the limit of $D(\mathbf{q}, \Delta t)$ as Δt approaches zero. In practice, we fit a quadratic function to the image structure function over a short time interval near the origin and estimate $B(\mathbf{q})$ as the intercept of the best-fitting curve. However, it's important to note that due to the strong signal coming from the vesicles in our concentrated samples, the choice of the $B(\mathbf{q})$ parameter has little impact on the final results. Similarly, given that $f(\mathbf{q}, \Delta t \to \infty) = 0$, one might consider extracting $A(\mathbf{q})$ from the long-time plateau of $D(\mathbf{q}, \Delta t)$. Unfortunately, due to the finite acquisition time imposed by experimental constraints, we often cannot capture the full relaxation of $D(\mathbf{q}, \Delta t)$ for all wavevectors.

To address this, we adopted an alternative approach: identifying a background image $I_0(\mathbf{x})$ that incorporates all the static, sample-independent contributions to the images. We then estimate the amplitude $A(\mathbf{q})$ directly from the power spectrum of the raw images, corrected for this background, using the formula:

$$A(\mathbf{q}) = 2 \left\langle \mid \hat{I}(\mathbf{q}, t) - \hat{I}_0(\mathbf{q}) \mid^2 \right\rangle - B(\mathbf{q}) \tag{2.7}$$

where the first right-hand term will be referred to as $D_0(\mathbf{q})$ or as the sample's *static* power spectrum. The image structure function $D(\mathbf{q}, \Delta t)$ reflects the *dynamic* power spectrum of the system. With both $A(\mathbf{q})$ and $B(\mathbf{q})$ determined, we can now invert equation 2.6 to obtain the intermediate scattering function.

To validate this methodology, as well as overcome any possible issues that may appear, we used a monodisperse solution of $500nm$ latex particles dispersed in water. We start by obtaining a sequence of images of our solution with an acquisition rate of $1Hz$. In figure 2.5, one can recognize the particles as small white or dark spots, while other larger spots correspond to objects of the background, such as dust particles on the camera sensor or the optics.

After collecting the sequence of images for a period of time suffi-

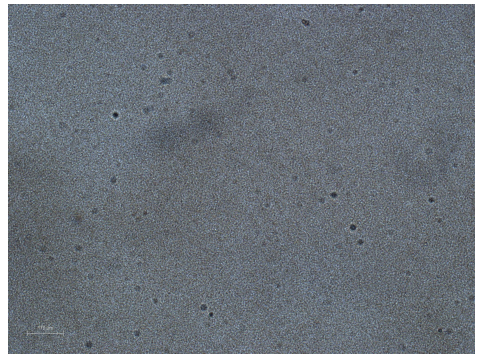

Figure 2.5. Image taken with a microscope at $t = 0$ for a monodisperse solution of latex particles.

cient for the decorrelation of the particle dynamics (this system is highly mobile), we compute the image structure function using eq. 2.5. Its 2D representation for $\Delta t = 100s$ is illustrated in figure 2.6. On this image two artifacts of different origin are visible. The first one corresponds to the quarter of a ring appeared at each corner of the image (highlighted in magenta), indicating a correlation between diagonally adjacent pixels, typical of color cameras. The second artifact is represented by the vertical and horizontal stripes (highlighted in green) and is attributed to spectral leakage [35]. To prevent the former issue, the analysis has been limited to selecting non-adjacent pixels by skipping one pixel in each row and col-

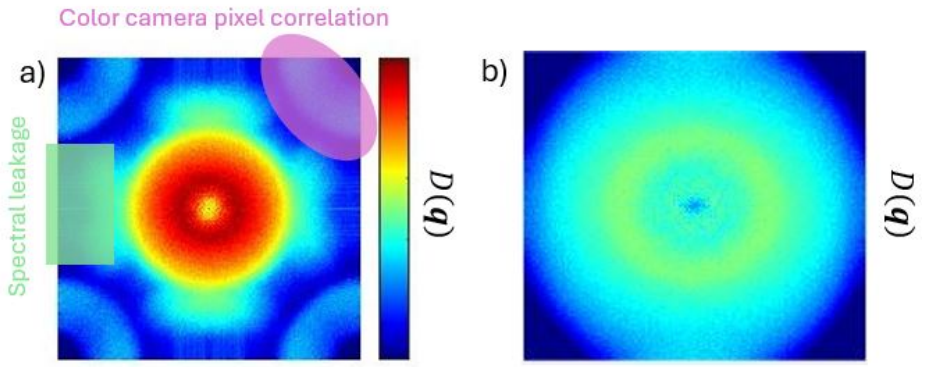

Figure 2.6. a) 2D image structure function $D(\mathbf{q}, \Delta t = 100s)$ *without* windowing for the latex particles suspension. The artifacts of the spectral leakage and the color camera pixel correlation are illustrated in green and magenta color respectively. b) 2D image structure function $D(\mathbf{q}, \Delta t = 100s)$ *with* windowing and after skipping adjacent pixels for the same suspension.

umn. The latter artifact has been addressed by including windowing [29] in the DDM algorithm.

After the computation of the image structure function eliminating these artifacts, we estimate $A(\mathbf{q})$ according to eq. 2.7. Initially, we evaluate the static background contribution, $\hat{I}_0(\mathbf{q})$, which is normally estimated as the temporal average $\hat{I}_0(\mathbf{q}) = \langle \hat{I}(\mathbf{q}) \rangle_t$ of an experimental acquisition performed by imposing to the sample a deformation amplitude. This amplitude should be large enough, so that the signal associated with the particles is completely averaged out, and only static features of the optical path, such as dust particles, remain. Since our system is highly mobile, we don't need to apply an extra deformation, but rather than average over the intensity signal of a large enough time span ($450sec$ in this case). The estimation of $\hat{I}(\mathbf{q}, t)$ is straightforward, and we can finally derive $D_0(\mathbf{q})$. In figure 2.7(a), we plot the normalized $D(\mathbf{q}, \Delta t)$ computed according to:

$$D_{norm}(\mathbf{q}, \Delta t) = \frac{D(\mathbf{q}, \Delta t) - B}{D_0(\mathbf{q}) - B} \tag{2.8}$$

B is a q-independent value accounting for the noise, and it is estimated so that the normalized image structure functions receive values between 0 and 1. Finally, the intermediate scattering functions (fig. 2.7(b)) are computed following:

$$f(\mathbf{q}, \Delta t) = 1 - \frac{D(\mathbf{q}, \Delta t) - B}{D_0(\mathbf{q}) - B} \tag{2.9}$$

The ISFs are then fitted to single exponential decays $f = exp(-(\Delta t/\tau))$.

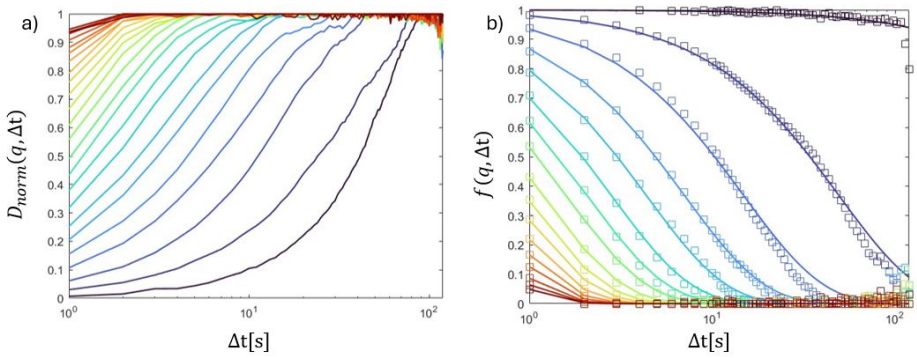

Figure 2.7. a) Image structure function normalized with the statics according to eq. 2.8. b) Intermediate self scattering functions as a function of time for different wavevectors. DDM data are shown with squares and the fits to $exp(-(\Delta t/\tau))$ as solid lines. The wavevectors increase from blue to red color.

The derived relaxation times are plotted in fig. 2.8, where we compare their q dependence with the analytical prediction for this system. For a dilute suspension of particles of known size in a solvent of known viscosity, the relaxation time is related to the wavevector through the following equation:

$$\tau(q) = \frac{1}{Dq^2} \tag{2.10}$$

where τ is the relaxation time, D the diffusivity of a single colloid, and q the wavevector. In the dilute regime, D can be calculated using the Stokes-Einstein formula $D = \frac{k_B T}{6\pi\eta R}$, where η is the solvent viscosity and R the particles radius. Figure 2.8 demonstrates that our DDM method

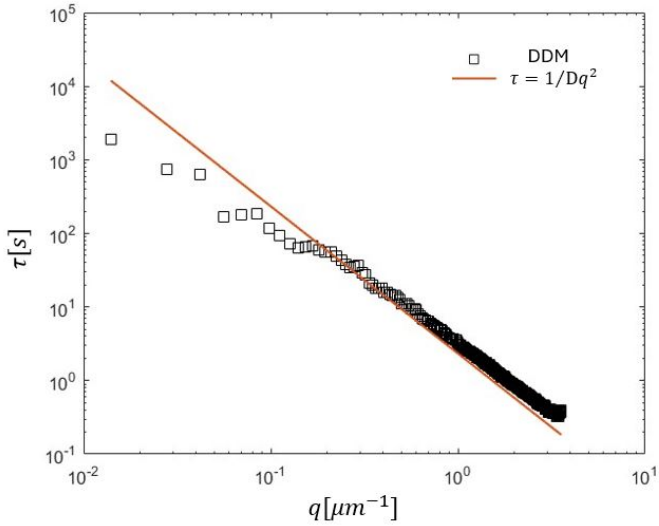

Figure 2.8. Relaxation times derived from an exponential fitting to the DDM data compared with a diffusive scaling using Stokes-Einstein formula, as a function of the wavevector.

closely matches the analytical solution for this system, confirming the accuracy of our methodology.

For our DDM measurements, we used a Zeiss AXIO Scope.A1 microscope with a Sony XCD-U100CR camera attached on it. The image structure function is calculated using a MATLAB script from the repository of the Helgeson Lab [6], while the rest of the computations are conducted with custom MATLAB scripts. All DDM experiments were conducted in the lab of Molecular, Macromolecular Chemistry, and Materials (C3M) at ESPCI University in Paris.

2.5 Brownian Dynamics (BD) Simulations

2.5.1 Simulation methods

Particle dynamics equations

Our simulation model consists of N neutrally buoyant particles (hard spheres) of radius α, suspended in an implicit Newtonian solvent of viscosity η and density ρ. The ratio between the fluid inertia and the viscous forces defines a Reynolds number $Re = \frac{\rho U a}{\eta}$, where U is the characteristic particle velocity. Due to the small size of the particles, which is of the order of $nm - \mu m$, $Re \ll 1$, meaning that inertia is negligible, and particle motion is governed by the Stokes equation. The motion of the fluid is governed by the Navier-Stokes equations, while the particle dynamics in Stokes flow is described by the Langevin equation, shown in eq. 2.11. The particle motion in a continuum solvent is dictated by hydrodynamic, Brownian, and interparticle forces.

$$\mathbf{m}\frac{d\mathbf{U}}{dt} = \mathbf{F}^H + \mathbf{F}^B + \mathbf{F}^P \tag{2.11}$$

where $\mathbf{m}$ is a generalized mass/moment matrix, $\mathbf{U}$ is the particle translational/rotational velocity vector, $\mathbf{F}^H$ is the hydrodynamic force exerted on the particles due to their motion relative to the fluid, $\mathbf{F}^B$ is the stochastic force that implements the thermal motion, and $\mathbf{F}^P$ is the deterministic non-hydrodynamic force which can be either interparticle or external. Since in BD simulations hydrodynamic interactions between particles are neglected, the hydrodynamic drag force is given only by the Stokes drag on an isolated particle, which is proportional to the particle velocity $\mathbf{U}_i$ relative to the fluid motion $\langle \mathbf{u} \rangle$, and for a particle i, is given by:

$$\mathbf{F}_i^H = -6\pi\eta\alpha_i[\mathbf{U}_i - \langle \mathbf{u} \rangle] \tag{2.12}$$

The stochastic Brownian force stems from the thermal agitation of the solvent molecules, and is given by the fluctuation-dissipation theorem:

$$\begin{aligned} \overline{\mathbf{F}_i^B} &= 0 \\ \overline{\mathbf{F}_i^B(0)\mathbf{F}_i^B(t)} &= 2k_BT(6\pi\eta\alpha_i)\mathbf{I}\delta(t) \end{aligned} \tag{2.13}$$

where the overbar denotes an average over the thermal fluctuations in the fluid, k_BT is the thermal energy, $\mathbf{I}$ is the unit isotropic tensor, and $\delta(t)$ the Dirac delta function. The interparticle force is derived from a potential which is selected based on the nature of the particle interactions that is simulated, and it can be either repulsive or attractive. A particle i will experience this force as a pairwise sum over all nearby particles,

$$\mathbf{F}_i^P = -\sum_j \frac{\partial V_{ij}(r_{ij})}{\partial r_{ij}} \hat{\mathbf{r}}_{ij} \tag{2.14}$$

where $\hat{\mathbf{r}}_{ij}$ is the unit vector pointing from the center of particle j to the center of particle i.

Interaction Potential

In the system where the vesicles are mixed with the polymer, the particles interact through both electrostatic repulsive and attractive interactions, and the total interaction potential is derived from the summation of the two individual ones. The Morse potential models the attractive interactions, while the Yukawa potential accounts for the EDL interactions:

$$E_{MORSE}(r) = E_0 \left(2e^{-\Delta[r-(\alpha_i+\alpha_j)]} - e^{-2\Delta[r-(\alpha_i+\alpha_j)]}\right) \tag{2.15}$$

where E_0 is the attraction energy set by the potential minimum, Δ^{-1} the attraction range, and α_i the radius of particle i.

$$E_{EDL}(r) = \frac{A}{\kappa} e^{-\kappa[r-(\alpha_i+\alpha_j)]} \tag{2.16}$$

where $A = 2\pi\epsilon\epsilon_0\psi_0^2 a\kappa$, with ϵ the relative permittivity of the fluid medium, ϵ_0 the permittivity of free space, ψ_0 the surface potential, κ the inverse of the Debye length. The Debye length and the surface potential values were taken from the work of Leivers et al. [57], where they conducted measurements of the electrostatic forces between interacting surfactant bilayers.

Figure 2.9 provides a schematic representation of the potentials, while in table 2.1, we report the values of the simulation parameters corresponding to the experimental ones. From top to bottom, we present the sur-

factant concentration translated to particle volume fraction, the polymer concentration to potential attraction strength, the polymer radius of gyration to attraction range, the ionic strength to the Debye length, and finally the polydispersity to the range of particles radii.

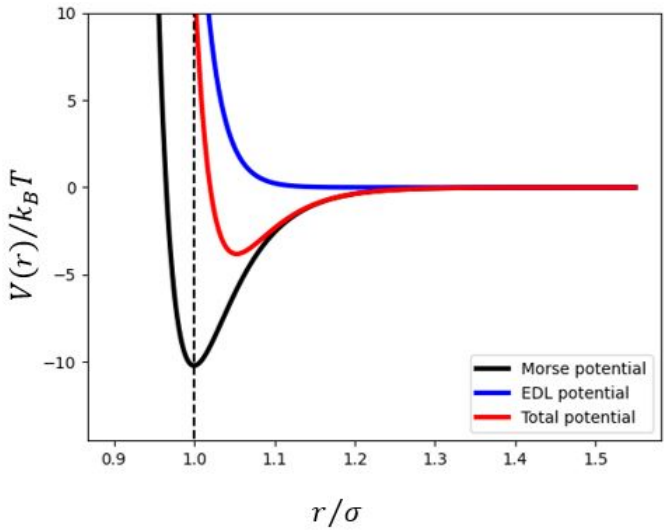

Figure 2.9. Potential energy as a function of particle distance. Three interaction potentials are illustrated, one for the attractive interactions (Morse), one for the electrostatic repulsive ones (EDL), and their summation (Total).

Experiments	Simulations
4, 11%wt/wt [surfactant]	$\phi = 0.4, 0.55$
1.6%wt/wt [polymer]	$U_{dep} = -4k_BT$
$R_g = 40nm$, $\xi(=\frac{Rg}{R}) = 0.27$	$\Delta = 10\alpha$
$[CaCl_2] = 450ppm$	$\kappa^{-1} = 0.044\alpha$
Polydisperse	5 particles radii with 7% std

Table 2.1. Correspondence between experimental and simulations parameters. From top to bottom: Particle volume fraction-Surfactant concentration, Polymer concentration-Attraction strength, Polymer radius of gyration-Attraction range, Salt concentration-Debye length of EDL interactions, Polydispersity-Selection of particles radii.

Numerical scheme and stress tensor

In the LAMMPS molecular dynamics software package [90], that we use for our simulations, the velocity is integrated forward in time via the velocity Verlet algorithm, where a Langevin thermostat enforces Brownian statistics. In Verlet integration, the importance of particle inertia is defined by the ratio of the Stokes number to the Peclet number, $\frac{St}{Pe} \ll 1$. In this scheme, while we cannot set this value to zero, we can reduce it enough to accurately model Stokesian physics. This is done by choosing a high thermostatting rate and a small time step. A high thermostatting rate ensures that the thermostat quickly adjusts the particles' kinetic energy based on the temperature difference from the desired temperature, so that the overall kinetic energy remains relatively constant between consecutive time steps. This rate, also known as the momentum relaxation time of the colloidal system, reflects how quickly the solvent molecules can relax a change in the Brownian particle's velocity back to its initial value.

In a solution of particles suspended within a medium, the bulk stress is computed as an average stress over the volume V containing N particles and is given by:

$$\langle \Sigma \rangle = -\langle p_f \rangle \mathbf{I} - nk_BT\mathbf{I} - nk_BT \left\langle \nabla \cdot (\mathbf{R}_{SU} \cdot \mathbf{R}_{FU}^{-1}) \right\rangle - n \left\langle \mathbf{R}_{SU} \cdot \mathbf{R}_{FU}^{-1} \cdot \mathbf{F}^P \right\rangle - n \left\langle \mathbf{x}\mathbf{I} \cdot \mathbf{F}^P \right\rangle \tag{2.17}$$

where the first term corresponds to the contribution of the fluid to the stresses, with $\langle p_f \rangle$ being the average fluid pressure, while the rest of the terms stem from the particle interactions. $nk_BT\mathbf{I}$ is the isotropic stress associated with the thermal motion of the particles, with n the number of particles, k_BT the thermal energy, and $\mathbf{I}$ the identity tensor. The next two terms are contributions to the stress coming from the hydrodynamic interactions of the particles and they are transmitted through the intervening medium. In particular, the former accounts for the disturbance flows produced by the Brownian motion of nearby particles, while the latter models the dissipative contributions from interparticle forces, with $\mathbf{R}_{SU}$ and $\mathbf{R}_{FU}$ being the hydrodynamic tensors. The final term considers the elastic stresses coming directly from the particle interactions, either repulsive or attractive, with $\mathbf{x}$ the interparticle distance between a pair of particles. $\mathbf{F}^P$ is calculated from the potential functional form, that is obtained based on the particle interactions.

In our freely draining simulations, the third and fourth terms are neglected, while the fluid pressure is also ignored, since we only consider the stresses coming from the particle phase. The medium is implicitly modeled as a background solvent and its effect is considered through the hydrodynamic drag and Brownian forces presented in eq. 2.11. After removing these terms, equation 2.17 is reduced to:

$$\left\langle \Sigma^P \right\rangle = -nk_BT\mathbf{I} + n\left\langle \mathbf{x}\mathbf{I} \cdot \mathbf{F}^P \right\rangle \tag{2.18}$$

This is the sole contribution of the stresses reported in this work.

2.5.2 Structural analysis

Apart from quantities that give us information about the macroscopic response of our system, like stresses and deformations, equally important is the characterization of the suspension microstructure. Microstructural changes can be monitored by both static and dynamic quantities and can play a significant role in determining the rheological properties.

When it comes to structural characterization, the pair distribution function, $g(\overrightarrow{r})$, measures the probability of finding a particle center at

relative position $\overrightarrow{r}$ in real space. It's given by the following function:

$$g(\overrightarrow{r}) = \frac{N}{V^2} \left\langle \sum_{i=1} \sum_{j \neq 1} \delta(\overrightarrow{r} - \overrightarrow{r}_{ij}) \right\rangle \tag{2.19}$$

where N and V are the number of particles and the volume of the simulation cell respectively, while $\overrightarrow{r}_{ij}$ is the vector pointing from the center of particle i to the center of particle j. However, the incapability of the pair distribution function to capture well enough the structural heterogeneity due to statistical averaging, leads us to the reciprocal space. The squared amplitude of the Fourier transform of density correlations is the static structure function:

$$S(q) = \frac{\langle \rho(\mathbf{q}) \rho(-\mathbf{q}) \rangle_{\mathbf{q} \cdot \mathbf{q} = q^2}}{N} \tag{2.20}$$

where N is the number of particles, and the wave number q is the magnitude of the scattering wave vector $\mathbf{q}$. The static structure is very handy in providing information about characteristic length scales in the particle configuration.

Apart from $S(q)$, another quantity that gives a measure of particles connectivity, and therefore is only applicable to attractive systems, is the average number of bonds or contacts. It is, essentially, the number of particles within the attraction range from their neighbors set at $r_{ij} = \alpha_i + \alpha_j + 2\frac{\kappa}{R}\alpha + 2\xi\alpha$, averaged over all particles. When it's normalized with its initial value and followed over time, we can conclude based on its value, if there is bond formation (> 1) or bond loss (< 1) in the system. The average potential energy, $\langle V \rangle$, normalized with its initial value, provides similar information, but distinguishes bond stretching (< 1) from bond compression/relaxation (> 1).

Proceeding, now, to the dynamic quantities, the Mean Square Displacement (MSD) gives a statistical measure of the distance, over which a particle has moved, in a specific time with respect to a reference position. If r_i is the position of the particle in the r direction and N is the total number of particles, then the MSD is generally calculated using the

following equation:

$$\left\langle \Delta r^2(\tau) \right\rangle_{N,t} = \left\langle \frac{1}{N} \sum_{i=1}^{N} [r_i(t+\tau) - r_i(t)]^2 \right\rangle_t \tag{2.21}$$

Note that when we apply a flow to our system, we should either remove the affine motion at every time step or just calculate the MSD in the vorticity direction, where no correction is needed.

Finally, another function that considers dynamic correlations in the reciprocal space, as well as tracks decorrelations of particles at different length scales, is the intermediate scattering function. It can be distinguished to the coherent- and self- intermediate scattering function, $F(q,t)$ (CISF) and $F_s(q,t)$ (SISF) respectively, which can be computed using the following formulas:

$$F(q,t) = \frac{1}{N} \left\langle \sum_j \sum_k exp[-i\mathbf{q} \cdot (\mathbf{X}_j(t) - \mathbf{X}_k(0))] \right\rangle_{\mathbf{q}\cdot\mathbf{q}=q^2} \tag{2.22}$$

$$F_s(q,t) = \frac{1}{N} \left\langle \sum_j exp[-i\mathbf{q} \cdot (\mathbf{X}_j(t) - \mathbf{X}_j(0))] \right\rangle_{\mathbf{q}\cdot\mathbf{q}=q^2} \tag{2.23}$$

where N is the number of particles, $\mathbf{q}$ is all wavevectors of magnitude $q = 2\pi/L$, L is the probed length scale, and $\mathbf{X}_j$ is the absolute position of a particle j. Physically, the SISF describes single-particle diffusion over the length scale $L \sim 2\pi/q\alpha$, while the CISF represents collective dynamics of a particle "cluster" of $L \sim 2\pi/q\alpha$, with α being the particle radius.

Chapter 3

Microscopic dynamics of charged vesicle suspensions

This chapter marks the beginning of the results section, focusing on the microscopic dynamics of charged vesicle suspensions. After a brief overview of the specific methods used for this system, we present our analysis of the thermal dynamics of white bases, utilizing both BD simulations and DDM experiments.

3.1 Methods

3.1.1 Samples and experimental methods

The measured samples, 11, 6, 4, 1, and 0.1%wt/wt [surfactant] were obtained by isotonic dilution of the initial white base, which has a concentration of 13%wt/wt with an ionic concentration of $[CaCl_2] = 450ppm$.

We performed DDM measurements of the aforementioned white bases. For the concentrated samples ($c \geq 4\%$), we acquired two image series, each consisting of 120 images, at two different frame rates ($f_1 = 0.1\ Hz$, and $f_2 = 1\ Hz$), while the dilute samples ($c = 1, 0.1\%$) were recorded at three distinct acquisition rates of 0.1, 1, and $5fps$. The distinct steps of this DDM analysis will be presented in section 3.2.2.

3.1.2 Simulation methods

We also conducted Brownian dynamics (BD) simulations to get information about the dynamics of the system under quiescent conditions. The electrostatic repulsive interactions between particles were implemented through the Yukawa potential given by the following relationship:

$$E_{EDL}(r) = \frac{A}{\kappa} e^{-\kappa[r-(\alpha_i+\alpha_j)]} \tag{3.1}$$

where $A = 2\pi\epsilon\epsilon_0\psi_0^2 a\kappa$, with ϵ the relative permittivity of the fluid medium, ϵ_0 the permittivity of free space, ψ_0 the surface potential, κ the inverse of the Debye length, and α_i the radius of particle i. The Debye length and the surface potential values were taken from the work of Leivers et al. [57].

Equilibration protocol

Initially, 50 000 particles are inserted in the simulation cell, and an energy minimization algorithm is applied to separate any overlapping particles, which could lead to excessively large forces. Following this, the particles begin to undergo thermal motion and interact with one another. The system is aged for a duration of 40-1000 Brownian times, t_B, depending on the volume fraction. This aging period is sufficient to reach quasi-equilibrium conditions, which is verified by monitoring the osmotic pressure until it reaches a constant value over time. The contribution of interparticle interactions to the osmotic pressure, denoted as Π^P, is a scalar quantity related to the trace of the stress tensor arising from these interactions:

$$\Pi^P = -\mathbf{I} : \mathbf{\Sigma}^P/3 \tag{3.2}$$

When the osmotic pressure remains constant, it suggests an isotropic distribution of stresses in all directions, which indicates that the system is in equilibrium. With the end of the equilibration protocol, the computational study commences, which includes passive evolution of the particles under the influence of electrostatic repulsive forces, and Brownian diffusion, in the absence of any external flow or stress. The configuration of particles, along with the particle-phase stress, are monitored continuously and recorded at high frequency throughout the simulation.

3.2 Results and Discussion

3.2.1 BD simulations

In figure 3.1, we present the particle MSD $\langle \Delta r^2(\Delta t) \rangle$. Each panel depicts the MSD as a function of time for different ionic concentration, varied by the particle volume fraction. Across all salt concentrations and volume fractions, an initial ballistic regime is observed, where the MSD scales with the time squared. This ballistic behavior aligns with previous works on hard-sphere systems [100, 78], while other studies of similar systems reported that the initial regime was diffusive [75]. We believe that polydispersity played a role in influencing the early diffusion, as Porpora et al. [75] simulated a bidisperse system, while in our simulations we included a wider distribution of sizes. For $\phi = 0.1$, this ballistic regime is quickly followed by a Fickian diffusive regime, where the MSD scales linearly with time. In the leftmost panel, corresponding to the highest ionic concentration, increasing the volume fraction leads to noticeable deviations from the linear behavior, manifesting as a sub-diffusive regime at intermediate times. The duration of this sub-diffusive regime extends with higher volume fraction, spanning up to three orders of magnitude in time. We expect that, at even higher salt concentrations, this type of glassy dynamics emerges at volume fractions comparable to those of hard-sphere colloids [11].

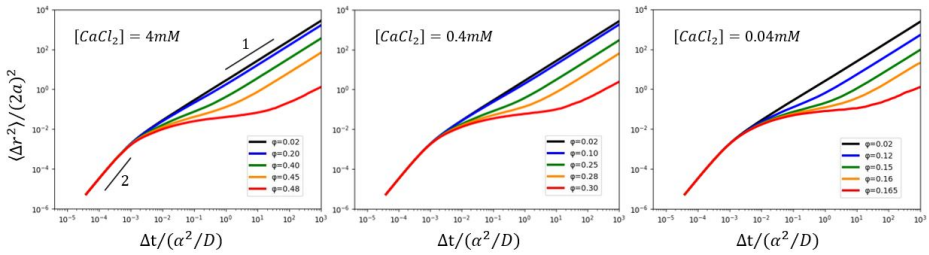

Figure 3.1. Temporal evolution of the Mean Square Displacement for three different ionic concentrations, parametric on the particle volume fraction as indicated in the legend.

At smaller ionic concentrations, the onset of glassy dynamics becomes evident at relatively low values of ϕ. For instance, at $[CaCl_2] = 0.04mM$,

a noticeable MSD plateau emerges already at volume fractions as low as $\phi = 0.15$. Moreover, this slowing-down occurs in a very narrow range of $\phi = 0.12$ to 0.15. This observation suggests that charged vesicle suspensions can be considered as Wigner glasses, where the transition to a glassy state can occur even in low-density suspensions, due to the presence of long-range repulsive interactions [58, 101, 10, 75].

Next, we turn our focus to the relaxation dynamics of such glassy systems, by computing the self-part of the intermediate scattering function (SISF). We define SISF as:

$$F_s(\Delta t) = \frac{1}{N} \left\langle \sum_{j=1}^{N} exp[-i\mathbf{q} \cdot (\mathbf{r}_j(\Delta t) - \mathbf{r}_j(0))] \right\rangle \tag{3.3}$$

where N is the number of particles, $\mathbf{q}$ is the wavevector, and $\mathbf{r}_j(t)$ is the displacement of a particle j. Figure 3.2 shows the SISF as a function of time

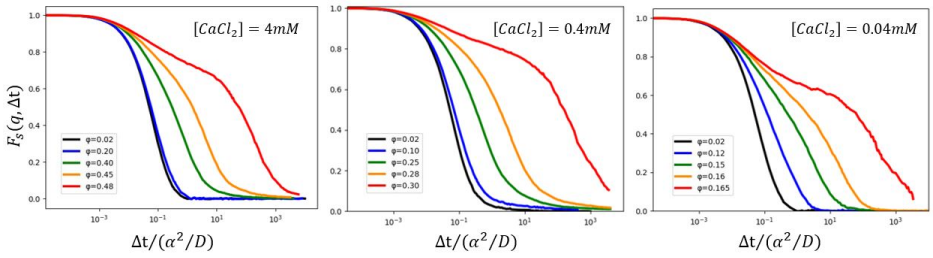

Figure 3.2. Temporal evolution of the intermediate self-scattering function for three different ionic concentrations, parametric on the particle volume fraction.

for the same systems presented in fig. 3.1, at wavenumber $q = 2\pi/\sigma$, where σ represents the average particle diameter (set to unity in the BD simulations). The SISF trend closely mirrors that of the MSD. Across all salt contents and low volume fractions, curves exhibit a single decay, well fitted by a pure exponential. However, as the volume fraction increases, similar to the MSD behavior, the SISF develops a two-step decay, characterized by a plateau at intermediate times. This plateau that is observed across all ionic concentrations, indicates a slowing down of the dynamics, a hallmark of glassy behavior. This type of relaxation is commonly explained using

the cage-jump picture [97, 20, 69]. In this framework, the initial decay, or β-relaxation, corresponds to particles rattling within the cage formed by their neighbors, while the later decay, or α-relaxation, occurs when the particles escape from the cage. Notably, the onset of the two-step decay in the SISF closely parallels the emergence of the intermediate-time sub-diffusion in the MSD, both of which can be rationalized within the same cage-jump picture.

3.2.2 DDM measurements

The system of charged vesicle suspensions was also studied through experiments, which aim at gaining insights into their microscopic dynamics. However, the high volume fractions of the concentrated samples and the significant difference in the refractive indices between vesicles and water make the suspensions optically dense, posing challenges to their characterization through Light Scattering (LS) techniques. In this study, we apply the method of Differential Dynamic Microscopy (DDM) to characterize the thermal dynamics of our system at different length scales. Thanks to the optical contrast mechanism, based on incoherent light scattering, we can access the high concentrations, typical of LFE formulations, remaining in the single scattering regime. This preserves a one to one correspondence between the image intensity fluctuations and the sample concentration fluctuations, so that from the image correlation functions we can extract the intermediate scattering function associated with the sample dynamics.

As explained in section 2.4, the DDM technique follows a series of computations until the final derivation of the intermediate scattering functions. We start by obtaining a sequence of images for all samples at specified acquisition rates (see section 3.1). As an indication, figure 3.3 shows two snapshots of the sample with $c = 4\%$ at two different time instants separated by $\Delta t = 1200s$. One can recognize the vesicles as white or dark spots, and that the second image differs from the first one, as an indication of the thermal motion of the vesicles. However, apart from our particle solution also the background contributes to the intensity signal of the images. Therefore, in order to eliminate its effect and consider only the particles contribution to the intensity, we calculate the image difference, as already analyzed (see section 2.4).

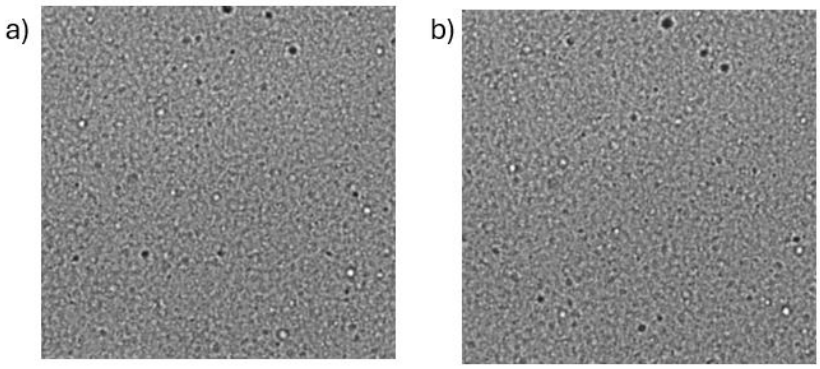

Figure 3.3. (a) Microscope snapshot at time t_n for a solution of $4\%w/w$ surfactant concentration, (b) Microscope snapshot at time $t_n + 1200s$ for the same sample.

The image differences are then subjected to Fourier transformations, and averaging over realizations of the same Δt, but different initial time t. Finally, the primary output of a DDM experiment is obtained, an image structure function $D(\mathbf{q}, \Delta t)$ for a q range going from $\frac{2\pi}{L}$, with L being the image size, to $\frac{\pi}{pix}$, with pix being the pixel size; and for a temporal range going from the inverse of the frame rate, to the maximum delay considered (typically one tenth of the full acquisition duration). This process is applied for all different concentrations $c \in [0.1\%, 11\%]$. As an indication, the 2D representation of the $D(\mathbf{q}, \Delta t)$ of $c = 4\%$ for two different time instants is illustrated in figure 3.4. These images are derived after including windowing and excluding adjacent pixels in our computations, in order to prevent the emergence of the artifacts seen in the solution of latex particles (section 2.4).

For the concentrated samples $c = 4, 6$, and 11%, the image structure function $D(q, \Delta t)$ and the static power spectrum $D_0(q)$ are obtained for two distinct frame rates, namely 1 and $0.1Hz$. Similarly, for the dilute samples ($c = 1, 0.1\%$), the dynamic and static power spectrums are derived from image series of $5, 1$, and $0.1Hz$. No background subtraction is applied to the static power spectrum of the samples. In the concentrated samples ($c \geq 4\%$) the signal is dominated by the particles, and hence no correction is needed, while in the dilute regime, two q-dependent param-

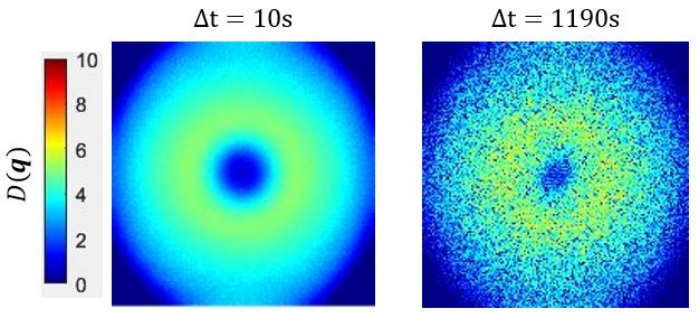

Figure 3.4. 2D image structure functions for two different time instants.

eters are used later on, in the fitting procedure, namely $A(q)$ and $B(q)$, implicitly accounting for the signal contrast between particles and background, as well as for the noise. The noise of the concentrated samples is subtracted from the power spectrum using a baseline value, so that the curves are normalized between 0 and 1 across the entire q range.

The intermediate scattering functions of the dilute samples are then computed according to

$$f(q, \Delta t) = 1 - \frac{D(q, \Delta t) - B}{D_0(q) - B} \tag{3.4}$$

for the two distinct acquisition rates, and are fitted to a single stretched exponential decay function $f = (A(q) - B(q)) \cdot exp\{-(t/\tau(q))^{0.8}\}$. The ISFs of the concentrated samples are obtained through merging of the curves calculated for each frame rate. This merging process employs a function $F(fps, \Delta t) = -log(f(q, \Delta t))$, where fps denotes the frame rate. For time delays $t < 10s$, we scale $F(1, t)$ with the factor $\kappa = F(0.1, t = 10s)/F(1, t = 10s)$, using this adjustment up to $t = 10s$. For delays $t > 10s$, we use $F(0.1, t)$ directly without adjustment. The merged ISF is then defined as follows:

- For $t \leq 10s$, it is given by $exp(-F(1, t) \cdot \kappa)$
- For $t > 10s$, it is simply $f(q, \Delta t)$ from the $0.1fps$ acquisition rate.

The ISF curves are, finally, fitted with either a single or double stretched exponential decay function, depending on the number of distinct processes

observed at each Q value. This is determined by identifying the number of different slopes in $-log(f(Q, \Delta t))$, as will be explained.

Below, we present the image structure function $D(\mathbf{q}, \Delta t)$ as a function of both time and wavevector (fig. 3.5) after the merging of the curves for the sample with $c = 4\%$. The image structure function exhibits a behavior

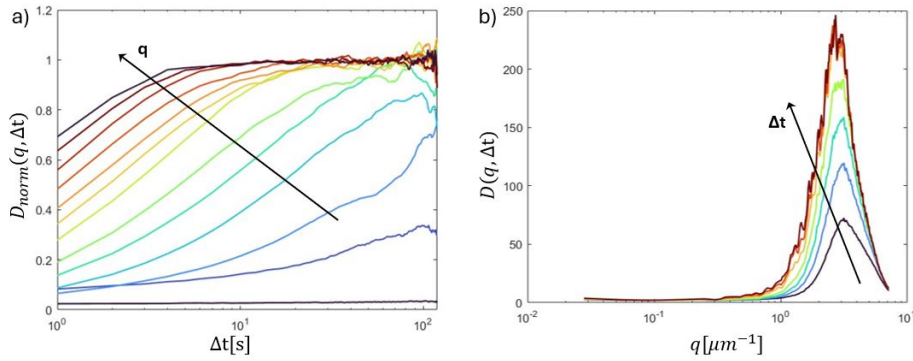

Figure 3.5. (a) Normalized image structure function as a function of Δt for the same system, parametric in the wavevector, (b) Image structure function $D(\mathbf{q}, \Delta t)$ as a function of q for a solution of $4\% w/w$ surfactant concentration, parametric in Δt. $D(\mathbf{q}, \Delta t)$ is calculated from the image sequence of $1Hz$ frame rate, while q and Δt increase in the direction indicated by the arrows.

consistent with the 2D contour plots of fig. 3.4. An initial growth at small wavevectors takes place, that gives way to a peak value, and then decreases to zero. As Δt increases, this peak value rises, reflecting the growing difference in intensity signals over time (see equation 2.5). Panel (a) of fig. 3.5 shows the temporal evolution of the normalized structure function (see eq. 2.8) for different q values. Initially, the function grows until it reaches a plateau, indicative of the decorrelation of particle dynamics. As expected, this plateau is attained more quickly for larger wavevector values (smaller probed length scales).

We start by examining the dynamics of the dilute suspensions with surfactant concentrations of 0.1% and $1\% wt/wt$. In this dilute regime, two distinct diffusive processes are observed according to fig. 3.6(b). Given the low concentration, particle interactions are expected to be negligible, so we attribute these two regimes to two different particle families with

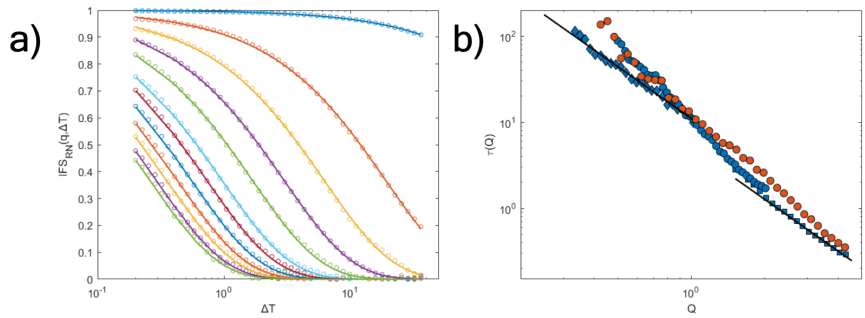

Figure 3.6. (a) ISFs in the dilute regime (open circles) fitted with single stretched exponential functions (solid curves) for the 0.1% sample. Different colors correspond to different wavevectors. (b) $\tau(q)$ derived from the fitting for both dilute samples. Red circles illustrate the relaxation times of $c = 1\%$, while the blue symbols correspond to the $c = 0.1\%$ sample. Squares are the results from the DDM analysis of image series at frame rate of $5Hz$, the circles at $1Hz$, and the diamonds at $0.1Hz$.

estimated radii of $R_1 \simeq 1\mu m$, and $R_2 \simeq 2\mu m$, based on their diffusion coefficients. Consistent with scattering theory, larger particles dominate the signal at lower wavevectors, in the interval $q \in [0.2, 0.9]\ \mu m^{-1}$. As q increases, we enter a transition range where the contributions from both larger and smaller particles merge and become indistinguishable. At higher q values, smaller particles dominate the intensity signal in a range of $q \in [1.5, 4]\ \mu m^{-1}$.

As we increase the concentration of vesicles, we expect crowding to start affecting the dynamics. In other words, the thermal diffusion of each particle is hindered by a temporary cage formed by its neighbors. The ISFs $f(q, \Delta t)$ show two distinct processes. This is clearly visible for low qs plotting:

$$-log(f(q, \Delta t)) \tag{3.5}$$

where we can observe a change of slope (fig. 3.7(b)). To capture these two processes, we fit the ISFs with a double stretched exponential decay:

$$f = \alpha(q) \cdot exp\{-(t/\tau_1(q))^{\beta_1}\} + (1 - \alpha(q)) \cdot exp\{-(t/\tau_2(q))^{\beta_2}\} \tag{3.6}$$

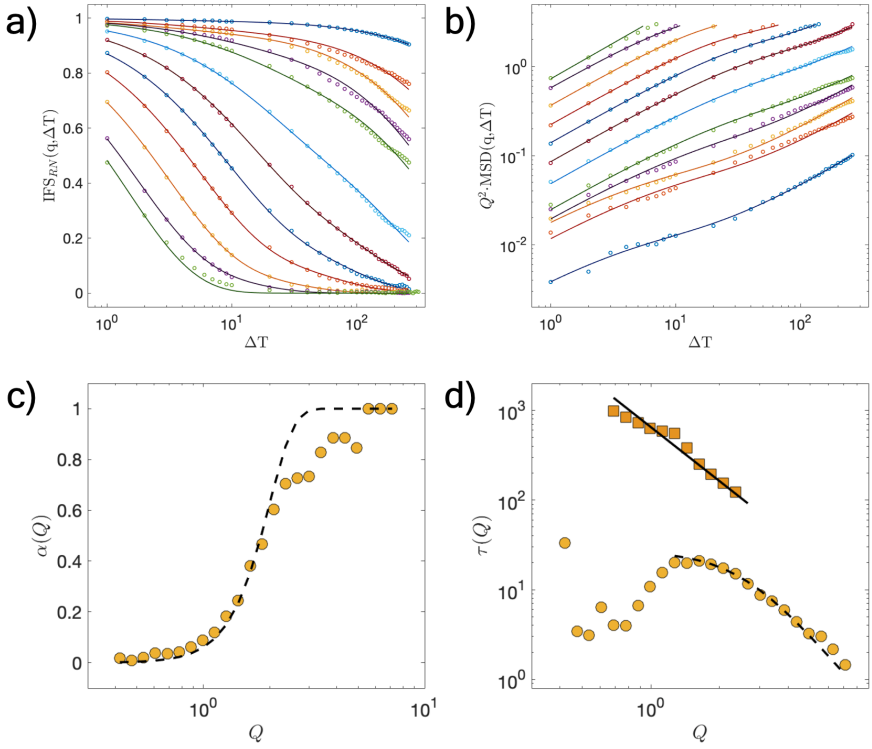

Figure 3.7. (a) ISFs for the sample $c = 4\%$. Different colors correspond to different wavevectors. (b) Plot of $-log(f(q, \Delta t))$ as a function of time. The continuous lines are the fits of the ISF with a sum of two stretched exponential decays (eq. 3.6). (c) Amplitude of the fast process as function of the wavevector. The dashed line corresponds to a $\alpha(q) = 1 - exp(-(q/q^{\star})^4)$ fit. (d) Relaxation times as a function of q for both processes. The solid black curve illustrates a sub-diffusive scaling $\tau \propto q^{-2.5}$.

where the relative magnitude α, and the relaxation times τ_1 and τ_2 are functions of the wavevector q, while the stretching exponents are fixed to $\beta_1 = 0.75$ and $\beta_2 = 0.65$ (for $c = 4\%$). By definition we take $\tau_1 > \tau_2$. The fast process dominates the dynamics at the largest qs and becomes progressively less important at smaller qs ($\alpha(q)$, symbols in (c)). This transition is phenomenologically captured by $\alpha(q) = 1 - exp(-(q/q^{\star})^4)$ (dashed line

in (c)). The associated relaxation time (circles in (d)) changes from being roughly q-independent at small qs to a subdiffusive scaling at high qs. This transition is described by $\tau_1(q) = \frac{\tau_c}{1+(q/q^\star)^b}$. These features suggest that the fast process can be interpreted as the in cage motion, where $q^\star$ is the wavevector associated with the cage size, and τ_c the lifetime of the cage. Inside the cage, the dynamics is sub-diffusive with an exponent $b \simeq 3$, and with a coefficient $K = \frac{1}{\tau_c(q^\star)^b}$. The slower relaxation process (squares in (d)) dominates the low q regime and it is not visible for $q \gg q^\star$, where the dynamics are dominated by the in-cage motion ($\alpha(q) = 1$). This second process is roughly diffusive $\tau_2 \propto q^{-2}$, and it's likely linked to the terminal relaxation of the system, as it corresponds to length scales way larger than the colloidal particles.

The same picture with two relaxation processes is recognized in samples $c = 6\%, 11\%$ (fig. 3.8), despite the fact that for the highest concentration studied, the range of accessible qs is limited by multiple scattering. The dependence of the two relaxation times τ_1 and τ_2 and their relative magnitude α on the wavevector q is also compatible with the in-cage/out-of-cage picture illustrated for $c = 4\%$. In fig. 3.9, the dynamic's parameters are compared for the three samples in the concentrated regime.

The cage size can be estimated with two different methods. We can consider the amplitude of the fast decay α and the characteristic $q^\star_\alpha$ for which we have the transition from out-of-cage dominated to in-cage dominated dynamics. Alternatively, we can take into account the fast relaxation time τ_1 and the wavevector $q^\star_\tau$ at which we have the transition from q-independent to sub-diffusive dynamics.

If we assumed that the signal originated from independent particles undergoing Gaussian dynamics, with in-cage regime, a plateau, and an out-of-cage diffusive regime, we would expect the fast relaxation time to strictly follow the model. Additionally, we would anticipate the amplitude α to follow an exponential decay as $\alpha(Q) = 1 - \exp(-(Q/Q^*)^2)$. However, our data aligns more closely with the phenomenological model $\alpha(Q) = 1 - \exp(-(Q/Q^*)^4)$. The primary reason for deviations in τ and α from the expected values is that, in our experiments, particle dynamics are strongly correlated. Furthermore, the parameters α and τ are not independent, which may also explained the observed difference between q^*_α (squares) and q^*_τ (diamonds). We report both values separately in

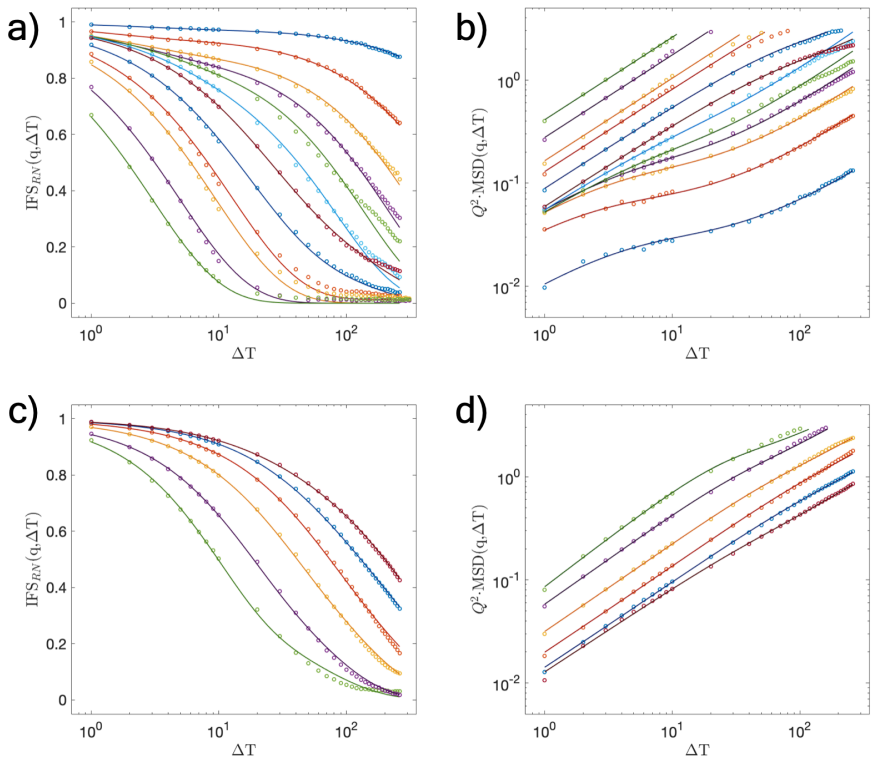

Figure 3.8. Intermediate scattering functions f and $-log(f)$ for $c = 6\%$ (a-b) and $c = 11\%$ (c-d). The range of accessible wavevectors for 6% is the same as for $c = 4\%$. For $c = 11\%$, the accessible range of qs is limited to $q > 1.8\mu m^{-1}$, because of multiple scattering. The color code is the same of fig. 3.7 and in particular the highest q shown for 6% corresponds to the higher q for 11% (in green).

fig. 3.9(e), confirming the same monotonic behavior as function of ϕ.

From the fastest relaxation times in the high q regime, we estimate the sub-diffusion coefficient K_{in}, and the lifetime of the cage τ_c. As the concentration increases, the in cage dynamics becomes slightly slower and the cage lifetime increases. Quite surprisingly, the out of cage dynamics display a non monotonic dependence on the concentration, with the diffusivity at 6% being larger than the one at 4%. Systematic studies on

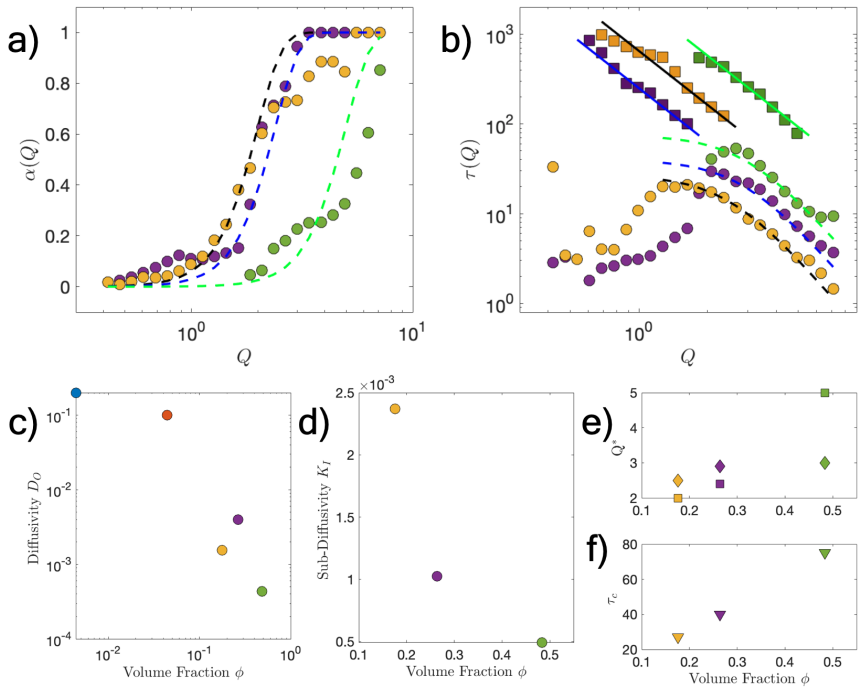

Figure 3.9. Microscopic dynamics fitting parameters. (a) Amplitude of the faster relaxation process $\alpha(q)$ for $c = 4\%$ (yellow), 6% (violet), and 11% (green). The dashed lines illustrated the associated fits to $\alpha(Q) = 1 - \exp(-(Q/Q^*)^4)$. (b) Relaxation times for $c = 4\%$ (yellow), $c = 6\%$ (purple), and $c = 11\%$ (green). The dashed lines are fits of the faster relaxation process (circles) to $\tau_1(Q) = \frac{\tau_c}{1+(Q/Q^*)^3}$. The solid curves are fits of the slow relaxation process (squares) to $\tau_2(Q) = 1/(D_{Out} \cdot Q^2)$. (c) Out-of-cage diffusivity $D_{(out)}(\phi)$ for all samples investigated in diluted and concentrated regime. (d) Sub-diffusion coefficient $K_{in}(\phi) = q^{\star 3}/\tau_c$. (e) Cage associated with the wavevector $q^{\star}(\phi)$ as estimated from the dependence of the fast decay amplitude $\alpha(q)$ (squares), and from the dependence of the fast decay (diamonds). (f) Cage lifetime $\tau_c(\phi)$ estimated from (b).

the dynamics of soft particles have shown an unexpected non-monotonic behavior in the relaxation rate as a function of the volume fraction [73]. In our observations, the terminal behavior slows dramatically compared to the dilute regime, with dynamics in the concentrated regime being ap-

proximately 2 orders of magnitude slower.

Chapter 4

Charged vesicle gels under quiescent conditions

In this section, we explore the second system under investigation: charged vesicle suspensions mixed with a non-adsorbing linear polymer. Using Brownian Dynamics simulations, we study how the gels evolve under quiescent conditions. Furthermore, through the calculation of various structural and dynamic properties, we gain insights into the gel morphology and the processes that drive microscopic changes over time.

4.1 Methods

4.1.1 Simulation methods

We performed Brownian Dynamics simulations of our colloidal depletion gels composed of charged particles, focusing on the evolving structure and particle dynamics under quiescent conditions. Initially, 500 000 particles are randomly distributed within the simulation cell which is periodically replicated. We selected a high number of particles for this study to ensure that the system's size adequately captures the structural and dynamic features being investigated. The gels exhibit a wide range of length scales and relaxation times, which can be significantly influenced by the size of the simulation cell. Using a smaller finite simulation cell could distort the dynamics and affect the accuracy of the measured properties. To

prevent overlapping particles that could generate excessively large forces, we employ an energy minimization algorithm to separate them. Following this, the particles start interacting through repulsive and attractive forces, while also experiencing hydrodynamic and Brownian forces. The gel is aged for three distinct times: $40, 400$, and $4000 t_B$, before the measurement of various structural and dynamical quantities. The simulation methods and the model used to simulate such a system are detailed in section 2.5.1.

4.2 Results and Discussion

4.2.1 Structure

It has been observed both experimentally [34] and by simulations [103] that in colloidal depletion gels, where particles form weak bonds, restructuring occurs over time, leading to coarsening. In these gels, thermal fluctuations are sufficiently strong to break existing bonds and reform new ones, resulting in thicker particle strands, and larger particle-poor voids between them. Figure 4.1 illustrates this bond mechanics, where a bond initially forms in a stretched state when two particles approach within the attraction range defined by the interaction potential. Based on the interplay between Brownian motion and attractive forces, the bond may either relax (when $V_0 > k_B T$ with V_0 the attraction strength) or rupture (when $V_0 < k_B T$), leading to a new bond formation, since the particles continue performing thermal motion.

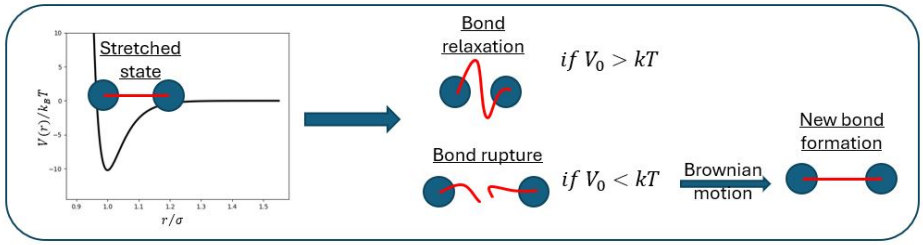

Figure 4.1. Schematic representation of the bond mechanics based on the interplay between Brownian motion and attractive forces.

This ongoing restructuring process is further evidenced by the temporal evolution of the potential energy, which becomes increasingly negative over time—a clear indication that the particles are settling deeper into the potential well in an effort to minimize their free energy. Figure 4.2 shows the temporal evolution of the average potential energy, normalized to its initial value. Its increase above unity for two different attraction strengths supports this view. In this section, we discuss this coarsening

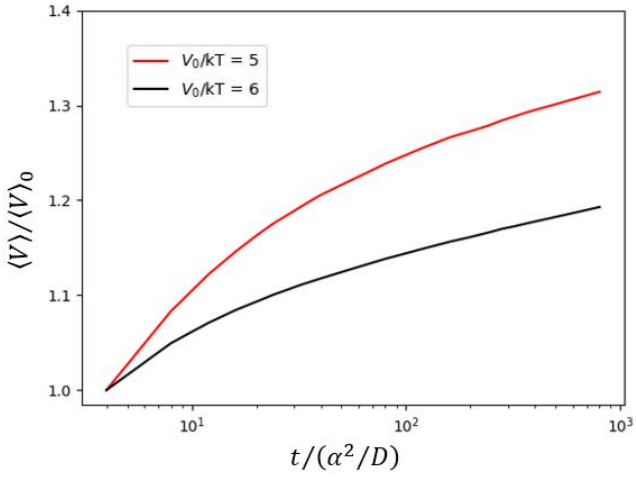

Figure 4.2. Temporal evolution of the average potential energy normalized to its initial value for two different attraction strengths.

process on our charged particle gels using parameters that model an LFE. In the current computational study, the passive evolution of the particle configuration takes place under the influence of short-range attractions, long-range electrostatic repulsion, and Brownian diffusion, in the absence of external flows or stresses.

Figure 4.3 shows the static structure factor for three different aging times over a wide range of wave vectors with two distinct peaks appearing in all curves. The first and higher peak, at the lower q limit, corresponds to the length scales with the highest particle correlation. For all ages, the peak appears within the range $0.6 \leq q\sigma \leq 0.9$, where σ is the average particle diameter, corresponding to fluctuations over length scales $7 \leq l\sigma \leq 10.5$. This range signifies the existence of length scales larger

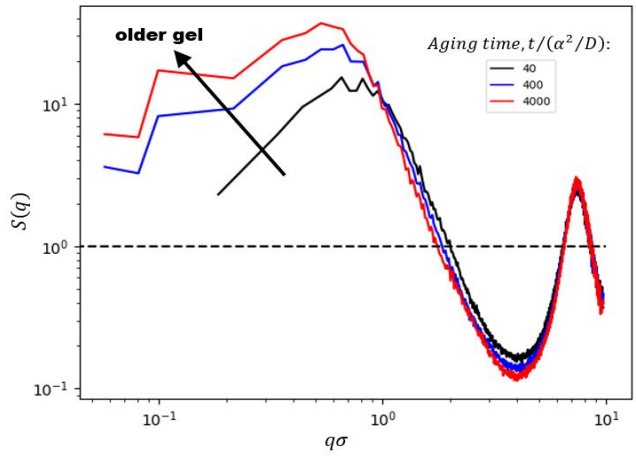

Figure 4.3. Static structure factor as a function of the wavevector, normalized with the average particle size, for 3 different aging times. The gel has a volume fraction of $\phi = 0.4$, and $U_{dep} = -4k_BT$ attraction strength.

than the particle size, equivalent to aggregates and network structure. This peak shifts towards lower q values as the gel ages, suggesting that the characteristic length scales, either strands or network pores, grow with age, as restructuring takes place. A second age-independent peak appears in the high q region. It corresponds to a length scale equal to two particles radii plus their electrical double layers, similar to what is expected also for HS systems [38].

The BD simulations can also provide us with snapshots of the microstructure, so we can directly visualize how this changes with time, and thus verify what we have observed from the static structure function. The subsequent snapshots (fig. 4.4), corresponding to the same aging times as in figure 4.3, show an increase in the heterogeneity of the gel structure over time, with the clusters becoming thicker and the interstitial voids larger. The color of the particles corresponds to a coordination number, and specifically to the number of neighboring particles within the bond range. This "bonded" state is set at $r_{ij} \leq \alpha_i + \alpha_j + 2\alpha\kappa_{DL} + 2\alpha\kappa_{EDL}$, where α_i and α_j are the particle radii, κ_{DL} is the dimensionless depletion layer thickness, and κ_{EDL} is the dimensionless electric double layer thickness, while this coordination number is also called number of contacts or

bonds. It is evident that, over time, more particles become red, signifying an increase in the average number of contacts. This number of bonds has been plotted also as a probability distribution function for the different aging times in fig 4.5. The curves shift to the right with gel age as the particles gain bonds with time, again an indication of the restructuring process. With continued aging, the distribution narrows and sharpens at $N_c = 11$ as strands grow thicker. Examination of the tails shows that there are few free diffusers and little crystalline structure.

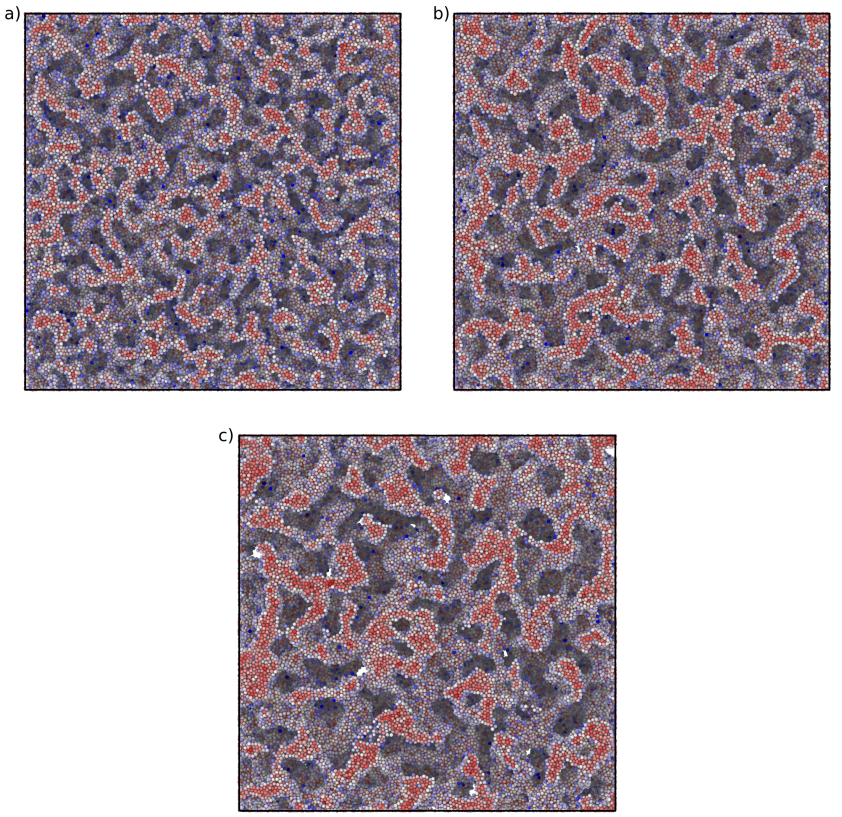

Figure 4.4. 2D images of the structure for a gel of $\phi = 0.2$ and $U_{dep} = -4k_BT$ as it evolves under quiescent conditions for different aging times of a) $40t_B$, b) $400t_B$ and c) $4000t_B$ taken from BD simulations.

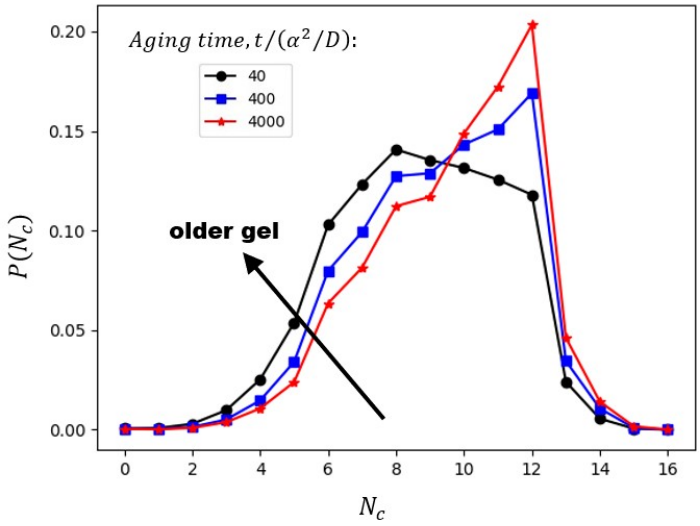

Figure 4.5. Distribution of contact number at different ages. The gel has a volume fraction of $\phi = 0.2$ and an attraction strength of $U_{dep} = -4k_BT$.

4.2.2 Dynamics

Let us now consider the dynamics of the system and the kinetic processes that cause it to evolve. It is well known that in glasses, the correlation of particles can last for long periods, whereas in dispersions, the structural relaxation goes to zero on Brownian time scales [80]. Moreover, in glassy systems, we can observe a rapid short-time "β-relaxation" corresponding to in-cage diffusion, which gives way to a long-time "α-relaxation" indicating out-of-cage motion, as already observed for the white bases. Our reversible colloidal gel exhibits the characteristics of both systems, having clusters consisting of particles confined in steric cages, and a particle-poor solvent penetrating these strands. The self-intermediate scattering function, depicted on fig. 4.6, reveals the diffusive dynamics of a particle, as it decorrelates from its initial position, over a wave number that corresponds to the dominant length scale of each age (1^{st} peak of the static structure function plot).

In a gel system like ours, the relaxation of dynamics at length scales comparable to cluster sizes requires significant time, making it computationally demanding in a simulation environment. While we can only observe the early decorrelation dynamics after the initial plateau, our findings indicate that relaxation slows down with age, suggesting that the structure becomes increasingly glassy over time. We have demonstrated that as coarsening occurs, the particle clusters grow longer and thicker. This thickening process leads to an increase in particles with higher contact numbers and low mobility, ultimately resulting in a slowdown of particle dynamics. Figure 4.6 supports this view.

So far, we have examined the relaxation dynamics at the network length scale; now we turn our attention to larger wavevectors, which correspond to length scales comparable to the sizes of the particles and their cages. Figure 4.7 illustrates the temporal evolution of the SISF at length scales ranging from 0.5 to 10 particle diameters, as indicated in the legend. Fitting these data to either a single or a double stretched exponential decay allows us to identify the presence of one or two processes in the relaxation dynamics of our gel, similar to what we did in the DDM analysis of vesicular dispersions.

The curves corresponding to 0.5σ and 1σ (where σ is the average particle diameter) are captured by a single stretched exponential, suggesting

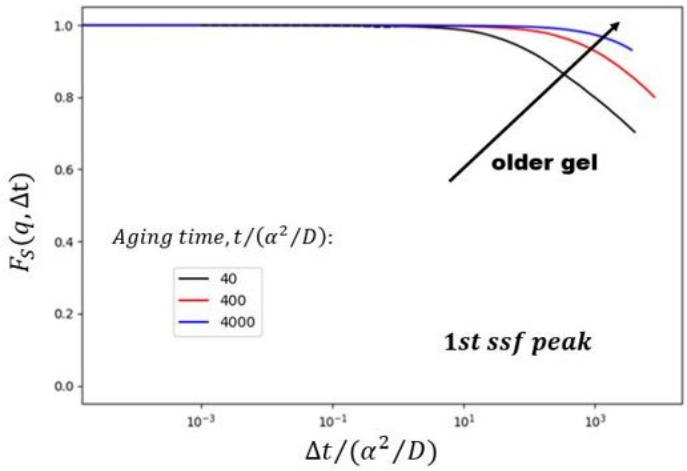

Figure 4.6. Temporal evolution of the intermediate self-scattering function at the wavevector of the 1st static structure function peak for 3 different aging times. The gel has a volume fraction of $\phi = 0.2$ and an attraction strength of $U_{dep} = -4k_BT$.

that at length scales comparable to the cage size, the decorrelation function reflects a single process: in-cage motion. As we move to decreasing wavevectors corresponding to length scales of $2 - 10\sigma$, the data cannot be adequately fitted by a single stretched exponential, indicating the involvement of a second process, namely out-of-cage motion. This behavior aligns with our observations in the DDM analysis of concentrated pure vesicular suspensions in section 3.2, where only a single process (in-cage motion) was captured in the high-q limit, while smaller wavevectors revealed a second process related to out-of-cage particle motion. This implies that, indeed, our charged vesicle gels show also characteristics of a glassy system.

Another dynamic quantity that can provide insights into the mobility of particles at the surface of the network strands, as well as deeper in them, is the mean square displacement. In colloidal dispersions, the short-time diffusivity reflects the thermal motion of a particle within a local cage formed by its nearest neighbors. This motion occurs over time scales that are too short to significantly alter the microstructure. Over longer times, the colloidal particles exchange neighbors and, in time, engage in

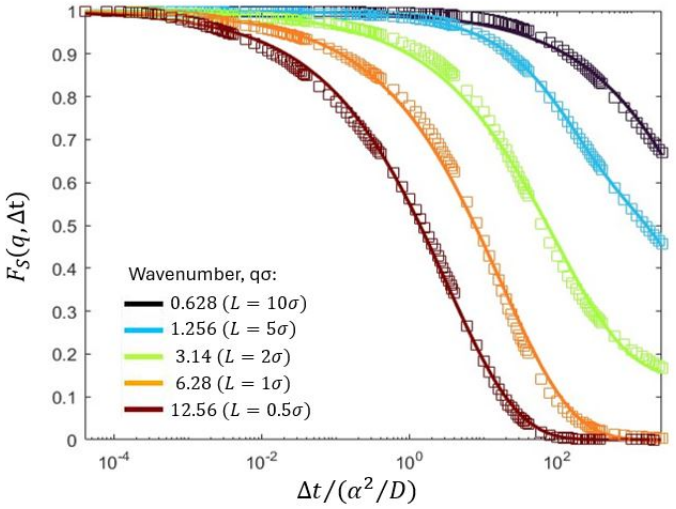

Figure 4.7. Decorrelation of the self intermediate scattering function at different wavevectors indicated in the legend. The squares correspond to the data derived from the simulations, while the solid lines to the fitting curves using single or double stretched exponential functions. The gel has a volume fraction of $\phi = 0.2$, an attraction strength of $U_{dep} = -4k_BT$, and an aging time of $40t_B$.

a random walk throughout the suspension, a process known as long-time self-diffusion. Previous studies [77, 27] have also examined diffusive migration in gels, as well as in the context of aging [103].

We computed the particles MSD to study how particle dynamics depend on caging. This dependence is revealed by binning the MSD according to the contact number, resulting in a "binned MSD", as introduced by Zia et al. [103]. In figure 4.8, we present the temporal evolution of this binned MSD over a time span of $100t_B$, which is sufficient to observe individual particle dynamics while remaining short enough to avoid significant structural change. Each curve in the plot represents the average MSD for particles within a specific contact number group, with the contact number N_c indicated next to the curves. The gels studied correspond to three different ages, as noted in the plot legend.

It is not surprising that particle mobility decreases with increasing

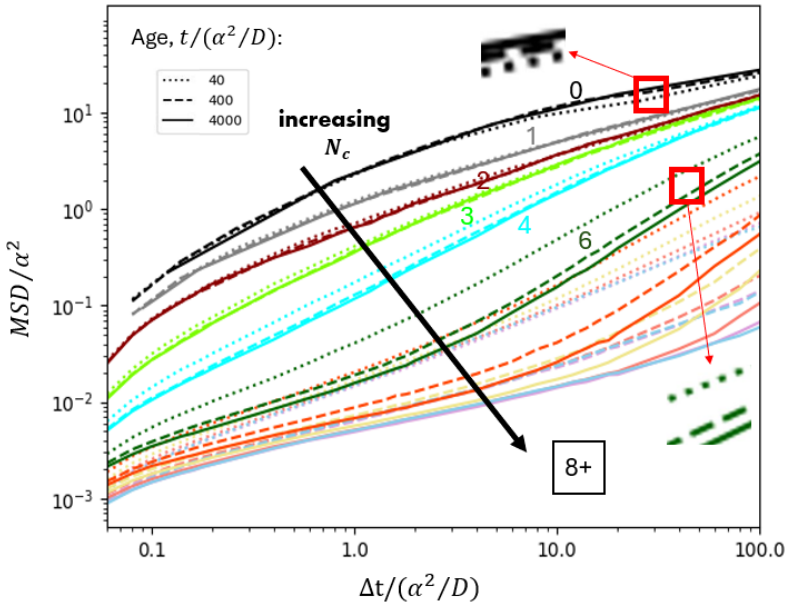

Figure 4.8. Mean Square Displacement as a function of time for each number of contact and three different aging times. The colored numbers match with the curves of the same color, indicating the corresponding number of contacts. The magnified snapshots show the sequence of curves of different age.

contact number at any given age. One might also expect that, for a specific contact number, particle mobility would decrease with age as the gel coarsens. This trend holds true for particles with four or more contacts, establishing a clear relationship between structural coarsening and a deepening dynamic arrest. Interestingly, however, the most mobile particles located on the outer surface of the gel do not exhibit this reduction in mobility with age. In fact, free diffusers ($N_c = 0$) demonstrate a marked increase in mobility, as indicated by the magnified snapshot, which is a result of the increasing pore size.

Chapter 5

Rheology and yielding of charged vesicle gels

The final chapter presents the main focus of this dissertation, demonstrating the effectiveness of our modeling framework in capturing the rheological behavior of LFEs. Both simulations and rheological measurements were carried out on the basis of various tests, including steady and oscillatory shear flows, as well as the application of shear stresses. By combining macroscopic rheological data with detailed structural images derived from simulations, we gain valuable insights into the relationship between rheology and microstructural morphology.

5.1 Methods

5.1.1 Experimental methods

Samples

For our rheological experiments, we used polydisperse suspensions of vesicles, with an average diameter of $0.3\mu m$, dispersed in water with a fixed ionic concentration, $[CaCl_2] = 450ppm$. We prepared vesicular solutions at two different surfactant concentrations, 4, and $11\%wt/wt$, through isotonic dilution of the initial one ($13\%wt/wt$). Depletion attractive forces were induced in the system by adding non-adsorbing linear chains of a copolymer made of acrylamide and DMA3, at a concentration equal to $1.6\%wt/wt$.

The polymer has molecular weight $M_w = 150\ 000 gr/mol$ and radius of gyration $R_g = 40nm$.

Rheometry

Rheological experiments were performed on an Anton-Paar MCR302 rheometer with cone-plate geometry (50mm and 0.01 rad angle). All measurements were conducted at $T = 20°C$ using a Peltier system. A solvent trap was employed during the experiments to prevent solvent evaporation.

5.1.2 Simulation methods

We also carried out Brownian Dynamics simulations to get both rheological and detailed structural information. The system is exactly the same as presented in chapter 4, with the only difference being the application of a flow or stress, rather than maintaining quiescent conditions. In the investigation of our system's rheology, we imposed steady and oscillatory shear flows, as well as shear stresses.

Steady shear flows

For the start-up flow tests, a linear shear flow is introduced, defined as $u_x^\infty(x, y, z) = \dot{\gamma} y$, by deforming the simulation cell at a predetermined rate and updating the particle positions accordingly. Here, x represents the flow direction, and y the flow gradient direction. As the applied deformation increases linearly, the cell continuously changes shape and gets distorted, while the particles are remapped to remain within the periodic simulation box. The relationship between shear rate and diffusion is captured by the *Peclèt* number, defined as $Pe \equiv \dot{\gamma}\alpha^2/D$, where α is the particle radius and D the diffusivity. We studied weaker flows within the range of $(0.01 \leq Pe \leq 10)$, investigating values that interpolate between regimes governed by Brownian motion and those dominated by advection. Additionally, we explored stronger flows that can completely break the microstructure ($Pe > 100$).

Oscillatory shear flows

For our oscillatory measurements, an oscillatory shear rate was applied, characterized by the following function: $\dot{\gamma} = \dot{\gamma}_0 \cos(\omega t)$, where $\dot{\gamma}_0$ is the amplitude of the oscillation, ω its frequency, and t the time during the oscillatory cycle. The resultant shear stress $\sigma(t)$ can be also expressed by a sinusoidal function:

$$\sigma(t) = \sigma_0 \sin(\omega t + \delta) \tag{5.1}$$

where σ_0 is the stress amplitude, and δ the loss angle. For small deformations, the shear stress $\sigma(t)$ is linear in the strain and strain rate, with coefficients that form the real and imaginary parts of a complex modulus G^* given by: $G^* = G' + iG''$, where G' is the storage modulus representing the elastic component of the material's response and G'' is the loss modulus, representing the viscous component. The degree to which the microstructure is distorted in an oscillatory test is set by two factors: The strength of the imposed flow relative to the Brownian restoring force, $Pe = \dot{\gamma}_0 \alpha^2 / D$, and the speed of oscillation relative to internal relaxations in the gel, $a = \omega / (D/\alpha^2)$. The dimensionless displacement is given by their ratio, $\Gamma \equiv Pe/a$, and the linear-response regime is probed when $\Gamma \ll 1$.

Creep tests

In creep tests, we employed a stress-control method, in order to maintain a constant applied stress to the simulation cell. This control method calculates a difference between the target shear stress and the measured current stress, modulating the shear rate towards the minimization of this difference. It's a proportional controller scheme, coming from the definition of the shear rate:

$$\dot{\gamma} = \frac{\sigma_0 - \sigma_{meas}}{\eta^H} \tag{5.2}$$

where σ_0 is the target shear stress, σ_{meas} the measured stress ($\sigma_{meas} \equiv \Sigma^P$), and η^H the hydrodynamic viscosity independent of the particle microstructure without hydrodynamic interactions, $\eta^H = \eta_s(1 + (5/2)\phi)$. In a freely draining suspension, as already presented in section 2.5.1, the interparticle stress Σ^P averaged over a timescale that is long compared to the momentum relaxation time, has two contributions, the ideal osmotic

pressure $nkT\mathbf{I}$, and the elastic stress $n\langle r\mathbf{F}^P\rangle$ coming from the particle interactions, either repulsive or attractive.

Time scales and simulation protocols

The time scales in the simulations and experiments are expected to differ due to the absence of Hydrodynamic Interactions (HI) in the former. In the experiments, particles within clusters are expected to slow down by approximately an order of magnitude, similar to the behavior observed in dense glasses [88]. Consequently, we adjust the simulation Brownian time scale, $t_B = \frac{6\pi\eta\alpha^3}{k_BT}$, with η being the solvent viscosity, by a factor $\sim 10^{-1}$. This scaling is applied consistently throughout the figures to the non-dimensional shear rate $Pe = \dot{\gamma}t_B$, as well as to the dimensionless frequency $\alpha = \omega(\alpha^2/D)$ and Pe_{dep}.

In all measurements, the gel was aged at rest for a certain time that will be reported in every figure before the application of a shear flow or stress. For oscillatory shear tests, data were averaged over a single oscillation cycle after a waiting period of 5 to 100 cycles, which is generally sufficient to achieve steady state. Similarly, in steady shear simulations, data were collected once the system reached a steady-state shear stress value.

5.2 Results and Discussion

5.2.1 Linear Viscoelastic Response

We start with the linear dynamic frequency sweep, which shows $G' > G''$ over the whole investigated frequency window, indicative of solid-like response (Fig. 5.1). The two panels show the viscoelastic moduli, G' and G'', for two gels of different volume fraction, namely 0.4 and 0.55. The applied strain amplitude is selected as $\gamma_0 = 0.005$, within the range of values in the linear viscoelastic regime, according to what was discussed in section 5.1.2. In both experiments and BD simulations, the moduli are nearly frequency-independent, while, as concentration increases, a slight hardening is observed, indicated by the small increase in the difference between the moduli. For the 4% sample, the simulation curves appear horizontally shifted relative to the experimental ones. This is an effect of

the shifting protocol we employed, where the shifting factors, which as we said account for the absence of HI in the simulations, were chosen to align the Newtonian regime of the flow curves more closely between simulations and experiments. These flow curves will be presented later. Importantly, the same shifting protocol was consistently applied across all measurements. Since the moduli in our frequency sweeps show minimal variation for different frequencies, this horizontal translation does not impact these values.

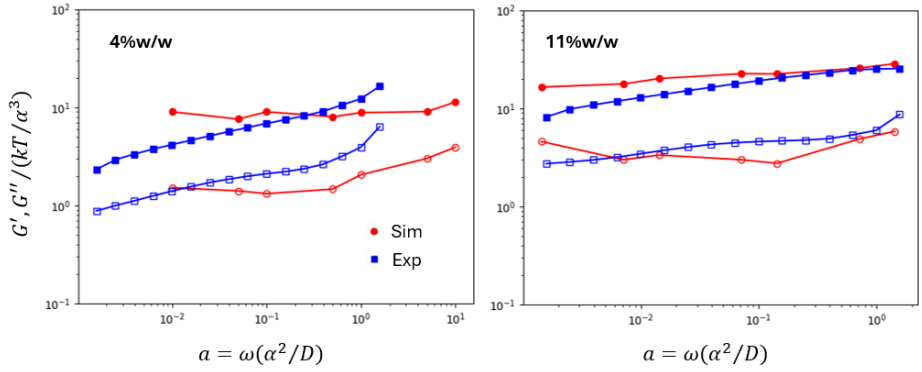

Figure 5.1. Viscoelastic moduli as a function of the angular frequency (frequency sweeps) taken from BD simulations (red circles) and experiments (blue squares). G' is shown by the solid symbols, while the G'' by the open ones. For the gels: $\phi = 0.4/U_{dep} = -4k_BT$ (left panel), and $\phi = 0.55/U_{dep} = -4k_BT$ (right panel).

5.2.2 Steady shear flow

Another key rheological test that can reveal the characteristics and type of our materials is the stress response to varying steady shear rates, commonly known as flow curve. In Fig. 5.2 we present the steady state shear stress response as a function of shear rate taken from both BD simulations and experiments. BD simulations closely match the experimental data, demonstrating the typical response of a colloidal depletion gel that behaves as a yield stress material. At very low Pe, a yield stress plateau emerges. This is the dynamic yield stress of the gel corresponding to the

value of stress that has to be applied to maintain the flow. Conversely, at very high Pe, there is a linear relationship between stress and shear rate implying a viscous response equivalent to that of a Newtonian liquid. Finally, for intermediate values of Pe, a sub-linear relation appears, indicative of shear-thinning behavior.

In the literature [51, 65], these transitions from low to high shear

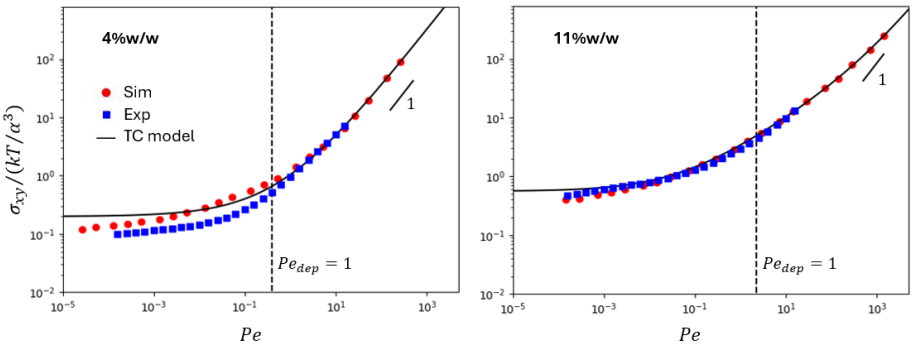

Figure 5.2. Normalized steady-state shear stresses as a function of Pe from BD simulations (solid red circles) and experiments (blue squares) for both samples. The dashed lines correspond to $Pe_{dep} = 1$ and the solid lines to the TC model fits with parameters: $\sigma_y = 0.2$, $\dot{\gamma}_y = 0.14$, and $\eta_{bg} = 0.31$ for the 4% sample, and $\sigma_y = 0.56$, $\dot{\gamma}_y = 0.041$, and $\eta_{bg} = 0.1$ for the 11%. Results are for gels with $U_{dep} = -4k_BT$ and $\phi = 0.4$, 0.55.

rates, corresponding to different macromechanical responses, are detected on the flow curve using a dimensionless number, Pe_{dep}, as follows [51]:

$$Pe_{dep} = \frac{F_{shear}}{F_{dep}} = \frac{6\pi\eta R(2\xi R)\dot{\gamma}}{U_{dep}(2R)/(2\xi R)} = \frac{12\pi\eta\xi R^3\dot{\gamma}}{U_{dep}(2R)} \tag{5.3}$$

When $Pe_{dep} < 1$, shear forces are stronger than attractive forces, which is expected to result in bond breaking. However, when $Pe_{dep} > 1$, attractive forces outweigh shear forces and in this case, shear helps the particles find, through local rearrangements, configurations with lower energy.

Our simulation data are well described by the three component (TC) model [12], a modified version of Heschel-Bulkley model, commonly used to represent the flow curve of a yield stress fluid. The TC model accounts

for the stress dissipation in sheared soft glassy materials as a combination of elastic, plastic and viscous contributions, and its formula is given below:

$$\sigma = \sigma_y + \sigma_y \left(\frac{\dot{\gamma}}{\dot{\gamma}_c} \right)^{1/2} + \eta_{bg} \dot{\gamma} \tag{5.4}$$

with the fitting parameters: σ_y, $\dot{\gamma}_y$, and η_{bg}. Here, σ_y represent the material's yield stress, while $\dot{\gamma}_c$ and σ_y/η_{bg} denote two critical shear rates. The first is linked to the relative magnitude between elasticity and plasticity, while the second relates to the interplay between the viscous and the plastic contributions to the stress.

In fig. 5.3, the flow curve of the gel is accompanied by 2D images of the structure at different shear rates taken from BD simulations. The

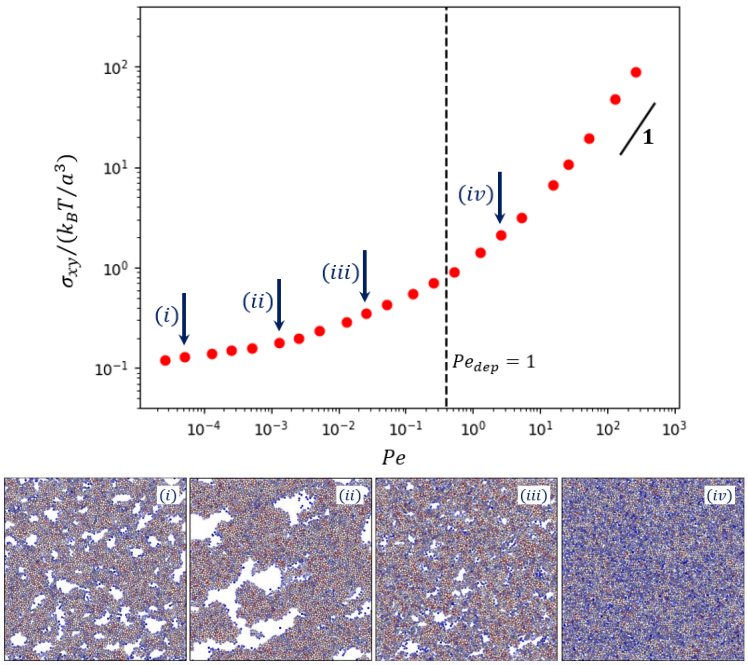

Figure 5.3. Flow curve for a gel with $\phi = 0.4$ and $U_{dep} = -4k_BT$ from BD simulations. Bottom images depict the gel structure under different Pe taken from simulations. Particles are colored based on their number of contacts.

color of the particles corresponds to the number of neighboring particles within the attraction range, defined as bonded state. Shearing at very low shear rates with $Pe_{dep} \ll 1$ results in the formation of heterogeneous structures (snapshot (i)) characterized by dense clusters resembling gels that age under quiescent conditions. With increasing shear rate, the structure experiences shear-induced coarsening with noticeably larger strands and interstitial colloid-poor voids between them, as illustrated in snapshot (ii). As we approach the $Pe_{dep} = 1$ line, the size of these clusters and voids diminishes, which reduces flow resistance and, in turn, decreases the effective viscosity, displaying shear-thinning behavior. Conversely, shearing at high rates ($Pe_{dep} > 1$) breaks the bonds between particles, leading to the formation of relatively homogeneous structures that resemble a hard-sphere liquid with a similar volume fraction. This results in a simple viscous response under shear. Thus, based on Pe, two distinct regimes are observed under shear, as previously shown by Koumakis et al. [51]. In one regime, clusters break up at high shear rates ($Pe_{dep} > 1$), while in the other, clusters densify at low shear rates ($Pe_{dep} < 1$).

5.2.3 Strain sweeps

Figure 5.4 shows the steady-state values of the storage and loss moduli, G' and G'', as a function of the strain amplitude γ_0, for three different angular frequencies ω, obtained from rheological experiments. Across all frequencies, two distinct regimes are evident: an initial regime, where $G' > G''$, indicating a solid-like response of the gel, followed by a second regime, where $G' < G''$, signifying viscous behavior. The first regime is known as the linear viscoelastic regime, since the viscoelastic moduli remain independent of the strain amplitude, while the second regime is non-linear, revealing the gel's response to higher values of deformation. As the angular frequency ω increases, the values of the moduli rise, and the yielding point shifts to higher strain amplitudes.

As has been noted in previous studies [65], two yielding points can be identified in a strain sweep of a gel, at the points where G'' exhibits its maxima. The first one occurs before the crossover point, attributed to the breakup of weakly connected clusters into smaller ones, while the second one takes place after the crossover, reflecting the intra-cluster bond breaking. In our measurements, the second yielding point is clearly evident at

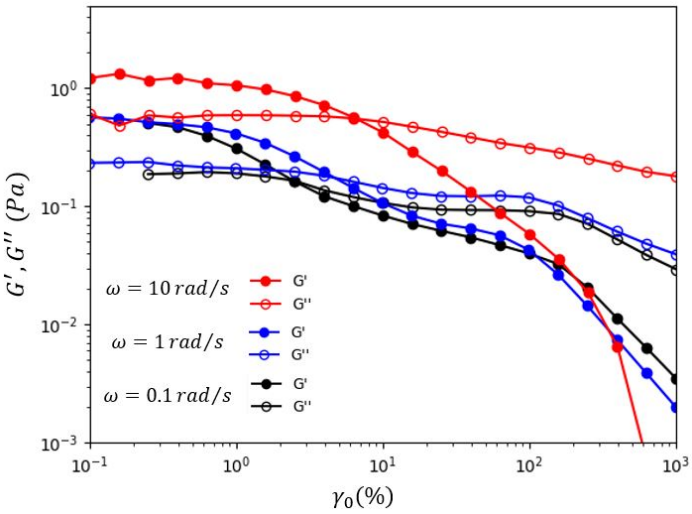

Figure 5.4. Steady-state values of the viscoelastic moduli as a function of the strain amplitude for three different angular frequencies $(0.1, 1, 10 rad/s)$ taken from rheological experiments. For the gel: $\phi = 0.4$ and $U_{dep} = -4k_BT$.

the angular frequencies of 0.1 and 1 rad/s, while the first yielding point is only slightly noticeable for 0.1 rad/s with a small change of the G'' slope.

In the previous section we have shown that BD simulations can effectively capture the macroscopic stress response, as well as the fundamental microstructural changes under steady shear flow, even without the inclusion of hydrodynamic interactions (HI). Focusing now on the oscillatory measurements, in figure 5.5, we plot the steady-state values of the storage and loss moduli, G' and G'', as a function of the strain amplitude, γ_0, for both BD simulations and experiments. The left panel displays the strain sweep for a gel with a volume fraction of $\phi = 0.4$, while the right panel corresponds to a gel of $\phi = 0.55$. For the gel with $\phi = 0.4$, both simulations and experiments, show that a first maximum of G'' appears at a strain amplitude of 5%. This peak represents the first yielding process and as it has already been mentioned, it is associated with the breakup of large, weakly bonded clusters [49, 55, 87]. As the strain amplitude continues to increase, both experiments and BD simulations show a crossover between G' and G'' at $\gamma_0 = 10\%$, after which the sample displays a liquid-like response

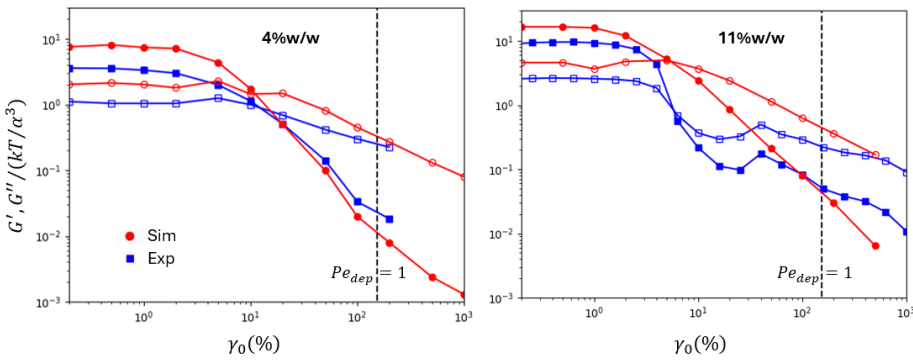

Figure 5.5. Steady-state values of the viscoelastic moduli as a function of the strain amplitude for BD simulations (red circles) and experiments (blue squares). Solid symbols show the G', and open symbols the G''. For the gel on the left panel: $\phi = 0.4$ and $U_{dep} = -4k_BT$. For the gel on the right panel: $\phi = 0.55$ and $U_{dep} = -4k_BT$.

($G'' > G'$). The second yielding process after the crossover point is only evident in the experimental data of the gel with $\phi = 0.55$ (right panel of fig. 5.5). This second peak is not observed in our BD simulations, possibly due to the absence of hydrodynamic interactions, which could influence microstructural changes under shear.

In figure 5.6, the plot of the viscoelastic moduli is accompanied by four slices of the microstructure at different strain amplitudes, marked by four upward arrows. In the linear viscoelastic regime, where the moduli are independent of γ_0, the microstructure shows no difference from the quiescent state. However, beyond the yielding point, at $\gamma_0 = 20\%$, it's clear that the oscillatory shear causes the formation of denser clusters with larger voids. This shear induced cluster densification should result in a higher average number of bonds, as also illustrated by the microstructure slice. The snapshot of the microstructure at $\gamma_0 = 100\%$ reveals a significantly more heterogeneous structure with larger clusters and voids under shear with respect to those observed at smaller strain amplitude. Unsurprisingly, the application of much larger strain amplitudes, $\gamma_0 > 200\%$, leads to the disintegration of the clusters, as shown in snapshot (iv).

As in the case of steady shear flow, structural changes in oscillatory

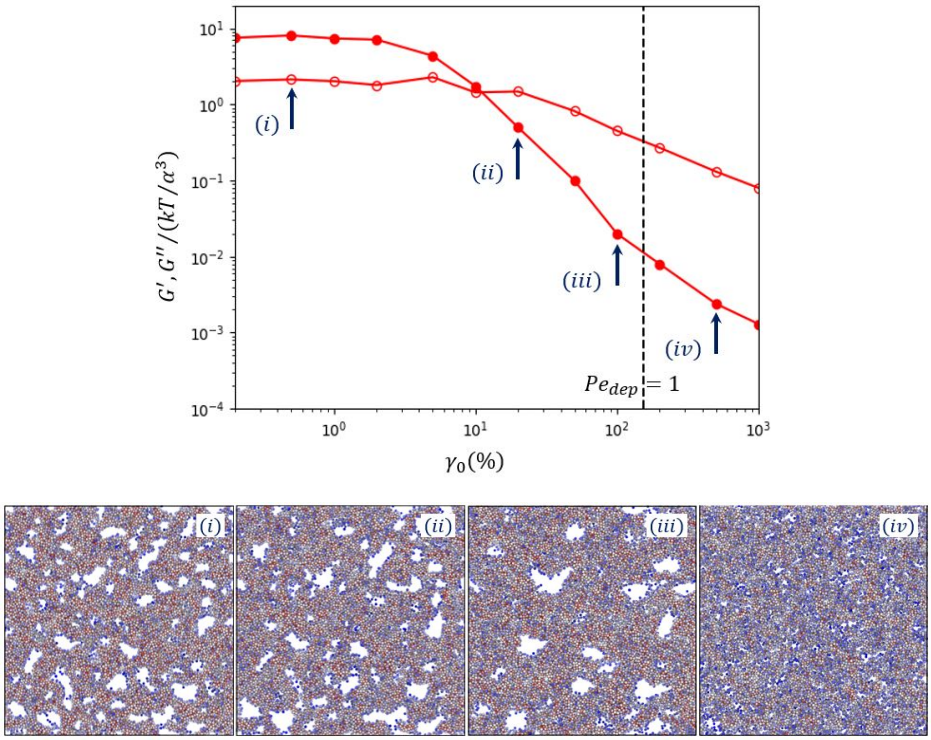

Figure 5.6. Viscoelastic moduli as a function of the strain amplitude at constant angular frequency $\omega = 10 rad/s$ for a gel with $\phi = 0.4$ and $U_{dep} = -4k_BT$ taken from BD simulations. The slices of the microstructure correspond to values of the strain amplitudes marked by the upward arrows and the color of the particles represents the number of bonds.

flows can also be quantified using a modified Peclet number, P_{dep}, introduced by Koumakis et al. [51]. This number accounts for the relative magnitude of shear forces versus attractive forces and, for oscillatory shear, is expressed by the following relationship:

$$Pe_{dep} = \frac{F_{shear}}{F_{dep}} = \frac{6\pi\eta R(2\xi R)}{U_{dep}/(2\xi R)} \frac{\gamma_0\omega}{2\xi R} = \frac{12\pi\eta\xi R^3}{U_{dep}(2R)}\gamma_0\omega \tag{5.5}$$

For $Pe_{dep} > 1$, shear forces are expected to rupture the bonds be-

tween particles, rendering attractive forces essentially inactive as the gel behaves like a liquid. In contrast, when $Pe_{dep} < 1$, inter-particle attractions strongly influence the system, leading to shear-induced rearrangements. This results in the formation of compact clusters, which increases the heterogeneity and the size of voids or clusters compared to the quiescent state, as shown in the BD images of fig. 5.6.

5.2.4 Number of contacts under shear

Apart from the microstructural images, another method to quantify the structural changes under shear is by measuring the average number of contacts [51, 103]. This is essentially a coordination number corresponding to the number of particles within the attraction range from their neighbors, averaged over all particles, as introduced in the previous section. We have

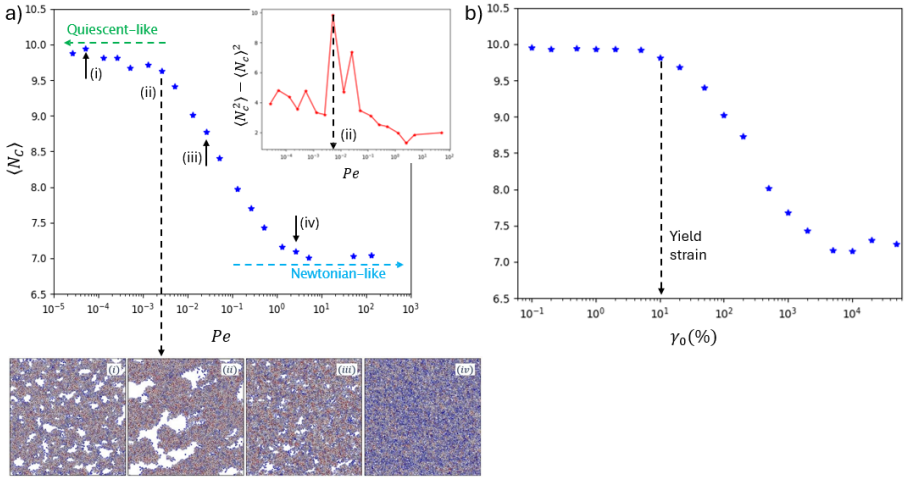

Figure 5.7. a) Average number of contacts as a function of Pe number computed from constant shear rate measurements. The inset shows the fluctuation of the number of contacts, while the snapshots correspond to Pe values marked by the arrows, b) Average number of contacts as a function of the strain amplitude calculated from oscillatory shear rate tests. Results are for a gel with $\phi = 0.4$ and $U_{dep} = -4k_BT$.

plotted (fig. 5.7) the dependence of the average contact number on the Pe

number for the steady shear case, as well as on γ_0 for the oscillatory shear tests. Both cases show a similar dependence with the formation of an initial plateau at small Pe and γ_0, indicating a $\langle N_c \rangle$ value that corresponds to the quiescently-aged gel. As the flow strength increases, the number of contacts drops due to structural breakage. However, in this regime, snapshots of the microstructure revealed a shear-induced coarsening. One might expect this restructuring to result in an increase of $\langle N_c \rangle$, but this does not happen. A possible explanation is that in more heterogeneous structures, not only do the clusters become denser, but the colloid-poor voids also enlarge, leading to an increase in the number of free diffusers ($\langle N_c \rangle \simeq 0$). As a result, the average number of contacts may appear to change little compared to less heterogeneous structures observed in smaller Pe.

To observe this increase in heterogeneity, we need to examine the fluctuations (or variance) of the number of contacts, as shown in the inset of fig. 5.7(a). If the variance is small, then N_c does not fluctuate much around its average, suggesting that the network is relatively homogeneous, while larger values indicate more heterogeneous structures. In our results, a fluctuation peak emerges at the Pe value corresponding to snapshot (ii), where the highest heterogeneity is observed. This suggests that the variance of N_c captures better the changes in the structural heterogeneity compared to the $\langle N_c \rangle$. Ultimately, the drop in $\langle N_c \rangle$ levels off to a second lower plateau, which reflects a particle solution exhibiting Newtonian-like behavior. At these high shear rates and deformations, the gel undergoes complete structural breakdown.

5.2.5 Yielding and flow behavior

Start-up flow

Next, we investigate the nonlinear transient response of our depletion gels during the start-up of a fixed strain rate. Our initial focus will be on understanding the microstructural origins of yield, and how structural and rheological yield relate to the release from kinetic arrest. We will study weak flows ($0.01 \leq Pe \leq 1$), where complete structural breakdown is avoided, imposed on weakly connected gels ($U_{dep} = 5 - 6k_BT$), similar to the ones used in LFEs. We'll examine the connections between bond

dynamics, structure, and rheology and then, apply these insights to interpret the rheological response of our depletion gels. This second part involves simulations encompassing a wide range of parameters, including three volume fractions of $\phi = 0.2, 0.4$ and 0.5, two different attraction strengths $-4k_BT$ and $-16k_BT$, as well as varying shear rates and ages. This analysis will provide a broader understanding of the parameters that influence the yielding behavior of Liquid Fabric Enhancers.

In figure 5.8, we plot the temporal evolution of the macroscopic shear stress response of a gel subjected to different values of shear rate. Regard-

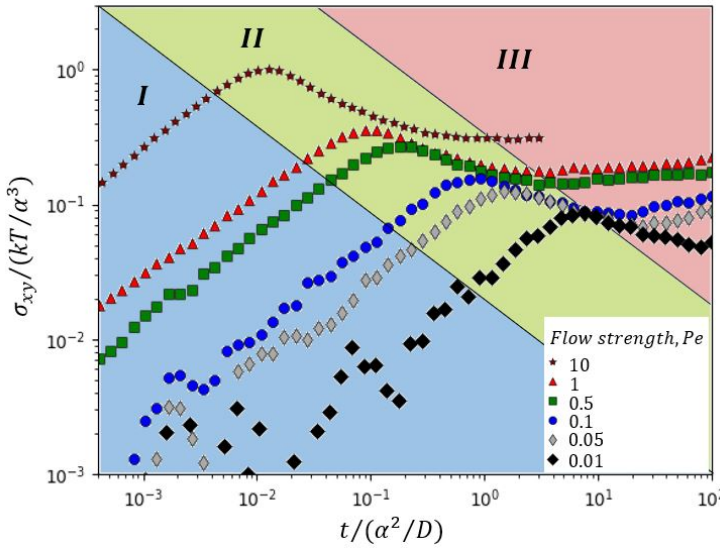

Figure 5.8. Stress normalized with the Brownian stress as a function of the diffusively scaled time for different Pe values. The three regimes are numbered and differently colored. Results are for a gel with $\phi = 0.2$ and $U_{dep} = -5k_BT$.

less of the applied shear rate, we can distinguish three different temporal regimes. In regime I, which is also called "pre-yield regime", stress grows, exhibiting a power law behavior. This stress build-up reaches a maximum stress value, the static yield stress of the gel for the respective Pe, and corresponds to the stress that has to be applied to the material to initiate flow. Regime II is the yield regime, where yielding takes place. Key aspects in this phase include the yield stress, yield strain, and the associated mi-

crostructure. The stress overshoot gives way to a stress decay, after which, regime III follows. This region characterizes the gel's long-term behavior, which is generally assumed to correspond to a steady, viscous flow.

Focusing, now, on the pre-yield regime, we plot the stress response, normalized by the ideal osmotic pressure, as a function of the diffusively scaled time (fig. 5.9). At early times following the onset of the imposed

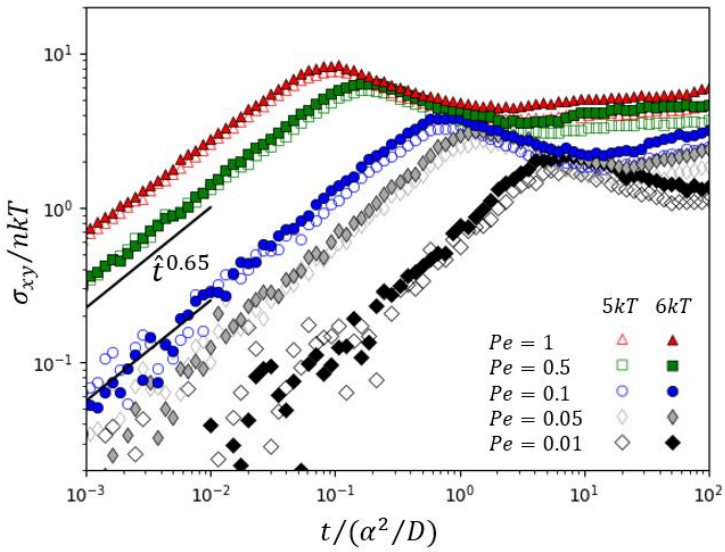

Figure 5.9. Shear stress normalized with the ideal osmotic pressure as a function of time for different Pe values and two attraction strengths 5 and $6k_BT$. The particle volume fraction is $\phi = 0.2$.

strain rate, the macroscopic shear stress rapidly increases and monotonically grows over time, defining the pre-yield regime. Two key factors in this regime are the rate of stress growth and the magnitude of the stress response (vertical shift). The stress growth follows a power law, $\sigma_{xy} \sim \hat{t}^{0.65}$, where $\hat{t} = t/(\alpha^2/D)$ represents the diffusively scaled time. As stronger flows are applied, the magnitude of the pre-yield stress increases, shifting curves upwards. This can be understood by considering stress as a measure of energy density; increasing flow strength adds more energy into the system, resulting in a larger stress response. In an attractive system, like

in our case, this energy is stored enthalpically through bond stretching, and entropically as microstructural distortion.

We also observe that, regardless of the attraction strength and the Pe, all the curves in the pre-yield regime scale with the same time exponent. This indicates that, at early times when microstructural distortion is minimal, Brownian diffusion is the primary influence on particle dynamics, leading to weak structural rearrangements and determining the temporal scaling of stress. When stress is scaled by the applied flow strength, the viscosity is obtained, as illustrated in figure 5.10. The steady-state vis-

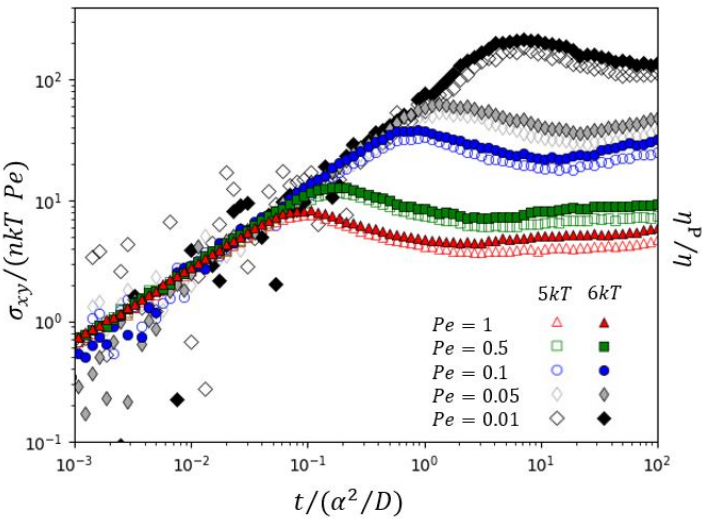

Figure 5.10. Non-dimensional viscosity as a function of time for different Pe values and attraction strengths.The particle volume fraction is $\phi = 0.2$.

cosity values decrease with increasing Pe as expected for a shear-thinning material, like our gels. Additionally, for all Pe values, the pre-yield regime is collapsed onto a single curve. However, as time progresses, the curves begin to diverge, marking the point where microstructural distortion increases and advection becomes dominant.

This macroscopic response can be linked to the gel's microstructure using two key quantities: the average number of contacts, $\langle N_c \rangle$, which represents the average number of neighboring particles within the attraction

range, and the average potential energy, $\langle V \rangle$, which indicates whether the bond between particle pairs is compressed, relaxed, or stretched. Both variables are normalized by their initial values before start-up, $\langle N_c \rangle_0$ and $\langle V \rangle_0$, and their temporal evolution is plotted in figure 5.11, with $\langle N_c \rangle / \langle N_c \rangle_0$ on the right axis and $\langle V \rangle / \langle V \rangle_0$ on the left axis. The normalized $\langle N_c \rangle$ (solid lines) distinguishes bond formation (values greater than one) from bond rupture (values less than one). Similarly, the normalized $\langle V \rangle$ (dashed lines) differentiates between bond stretching (values less than one) and compression (values greater than one).

In figure 5.11, the temporal evolution of these variables is shown across the entire pre-yield regime for the flow strengths depicted, as well as during the peak stress phase in the yield regime. Both the average normalized

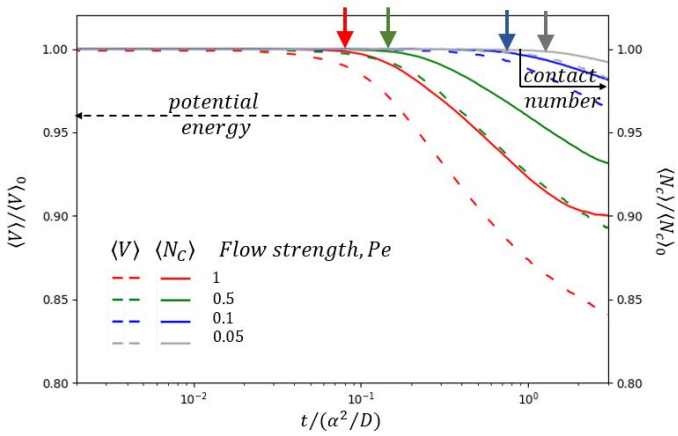

Figure 5.11. Average normalized potential energy (left axis) and average normalized number of contacts (right axis) as a function of time for different flow strengths. The arrows mark the macroscopic yield point for each Pe.

potential energy and the average normalized number of contacts drop below unity at a certain point, indicating bond stretching and bond loss. It is not surprising that the potential energy decreases before the number of contacts, as bonds typically stretch before they break. As expected, higher flow strengths lead to a quicker and greater percentage of bond stretching and loss. The vertical arrows indicate the onset of bond loss.

We can now compare this microstructural evolution with the macro-

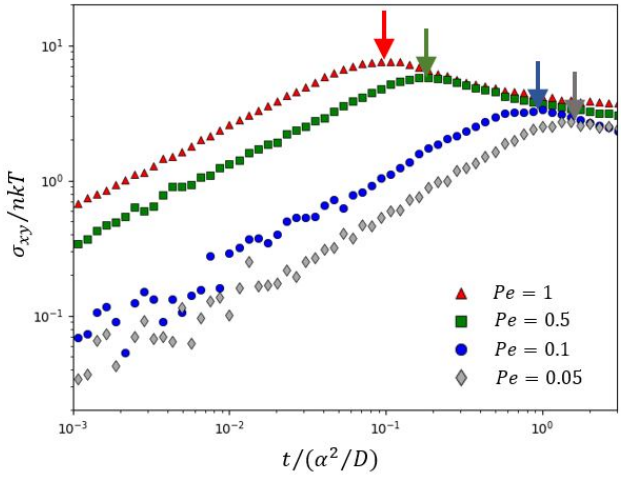

Figure 5.12. Shear stress normalized with the ideal osmotic pressure as a function of time. The arrows mark the peak stresses (macroscopic yield points).

scopic stress response to see if there is any correlation. In figure 5.12, we plot again the temporal evolution of the shear stress, marking the macroscopic yield point—the point where stress reaches its maximum value for the respective Pe—with a downward arrow. The comparison reveals that the time at which the gel starts to lose bonds coincides with the peak stress, suggesting that a certain percentage of stretched and subsequently broken bonds must be reached for the gel to begin yielding.

Another key characteristic of the bonds that can be assessed through BD simulations is their preferable orientation. When dispersions of repulsive hard spheres experience steady shear flow, they tend to accumulate along the compressional axis and deplete along the extensional axis. However, attractive forces alter the relative trajectories of particles, drawing some toward the depleted regions. To identify this behavior, we calculate the fabric tensor $\mathbf{R}$, which tracks the distribution of bonded neighbors:

$$\mathbf{R} = \frac{\phi}{N} \sum_{i=1}^{N} \sum_{j \neq i}^{N} \hat{\mathbf{r}}_{ij} \hat{\mathbf{r}}_{ij} \tag{5.6}$$

where ϕ is the particle volume fraction, N the number of particles, and $\hat{\mathbf{r}}_{ij}$ the orientation vector that points from the center of particle i to the center of particle j, for pairs of particles within the attraction range.

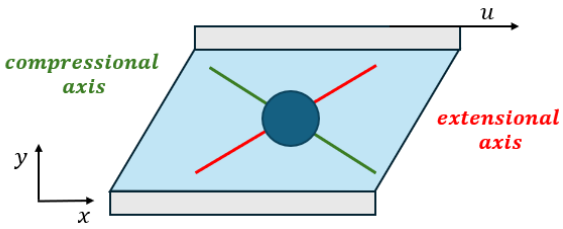

Figure 5.13. Schematic representation of the direction of compressional and extensional axes around a particle in a shear flow.

To measure the anisotropy of particle bond orientation in the flow-flow gradient (xy) plane, we calculate the off-diagonal component of the fabric tensor, R_{xy}. A positive R_{xy} indicates orientation along the extensional axis, while a negative R_{xy} signifies alignment along the compressional axis. We track R_{xy} as an average over all particles, computed over time after the onset of flow. The bond orientation in the flow plane is shown in figure 5.14 for various flow strengths. Initially, when structural distortion is small, $R_{xy} = 0$, indicating an isotropic bond distribution. At such small deformations, only Brownian diffusion affects the dynamics, smoothing out any minor distortions caused by advection.

In the yield regime, both the gel's yield stress and yield strain are key parameters. In figure 5.15 , we plot the shear stress against the shear strain, rather than time. Strain represents the accumulated deformation over time, and the effect is noticeable. While peak stresses spread across different timescales in the time-based plot, now, they nearly align. The strain corresponding to each peak is the yield strain for the respective Pe. The yield strains for the examined Pe values fall within a narrow range of $8\% \leq \gamma_{strain} \leq 13\%$.

We also present the yield stress values, taken as the peak stresses observed in the macroscopic stress response shown in fig. 5.8. We report the static yield stress values for different Pe and aging times (fig. 5.16). As expected, these values increase with stronger flows, as more energy is

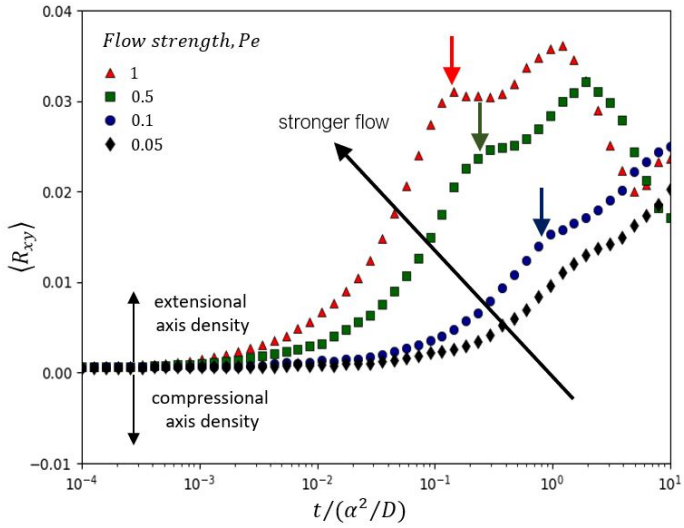

Figure 5.14. XY-component of the fabric tensor as a function of time, with the arrows marking the macroscopic yield point for each Pe.

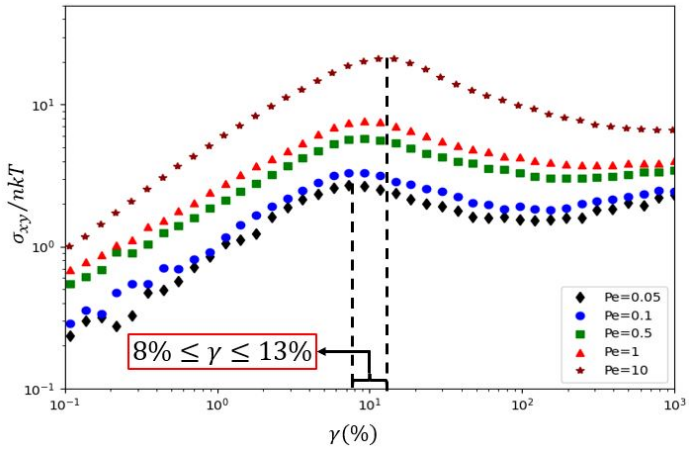

Figure 5.15. Shear stress normalized with the ideal osmotic pressure as a function of strain for different flow strengths.

introduced into the system, which the gel stores either through bonds or microstructural distortion, leading to a higher stress response. Similarly, aging time increases the yield stress due to the age-stiffening of the gel, as a result of the ongoing coarsening process analyzed in chapter 4. Therefore, older gels exhibit larger yield stress values.

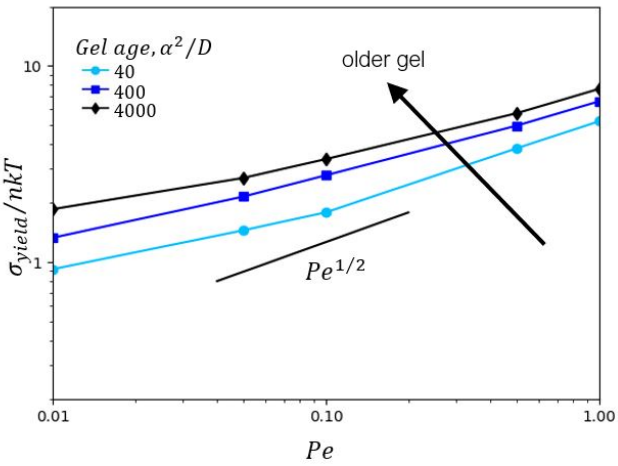

Figure 5.16. Yield stress normalized with the ideal osmotic pressure as a function of Pe for different aging times, as shown in the legend.

We now aim to explore the microstructural changes that occur during the yielding of our gel by examining the evolution of the average normalized potential energy and contact number as functions of the accumulated deformation (strain). Both variables start to decrease below unity after the macroscopic yield point, indicated by the vertical arrows (fig. 5.17). Interestingly, the percentage of lost bonds at this stage is less than 0.1%, suggesting that, during yielding after weak start-up flows, no cluster breakage occurs, unlike what we might expect under stronger flows. In this type of rheological yield, breaking even a small fraction of bonds can lead to the relaxation of many more, reducing the glassy frustration within clusters and facilitating viscous flow.

The snapshots in figure 5.18 provide a visual representation of the gel's microstructure at various deformation levels, as noted. The microstructure at 10% strain, which corresponds to the yield strain for this gel, shows no

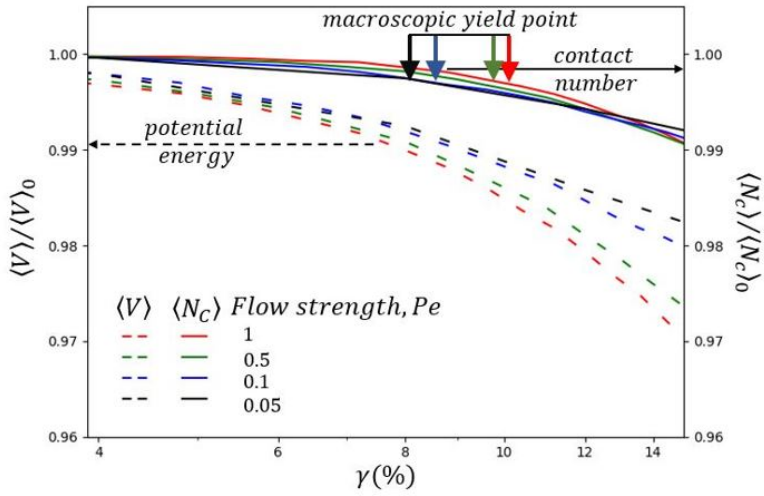

Figure 5.17. Average normalized potential energy (left axis) and average normalized number of contacts (right axis) as a function of strain for different Pe values. The arrows mark the macroscopic yield points for the respective Pe.

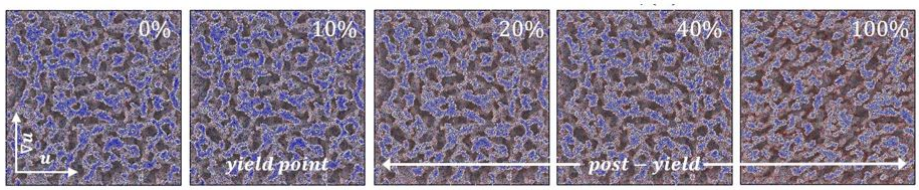

Figure 5.18. Microstructure snapshots at different deformation levels under a shear flow of $Pe = 1$. The corresponding deformation levels are written on the snapshots.

significant change compared to the initial structure, confirming that the gel yields with an intact network. To observe noticeable structural changes, we must look at higher deformations, as illustrated in the final snapshot at 100% strain.

Finally, in order to evaluate the terminal behavior of our gel, we need to observe its evolution at later times and higher deformations. Figure 5.19 gives snapshots of the structure prior to flow ($\gamma = 0\%$), at the yield point

($\gamma = 10\%$), and post-yield ($\gamma = 800\%$), in the flow-flow gradient plane, for $Pe = 1$ (upper snapshots) and $Pe = 0.05$ (lower snapshots). At the

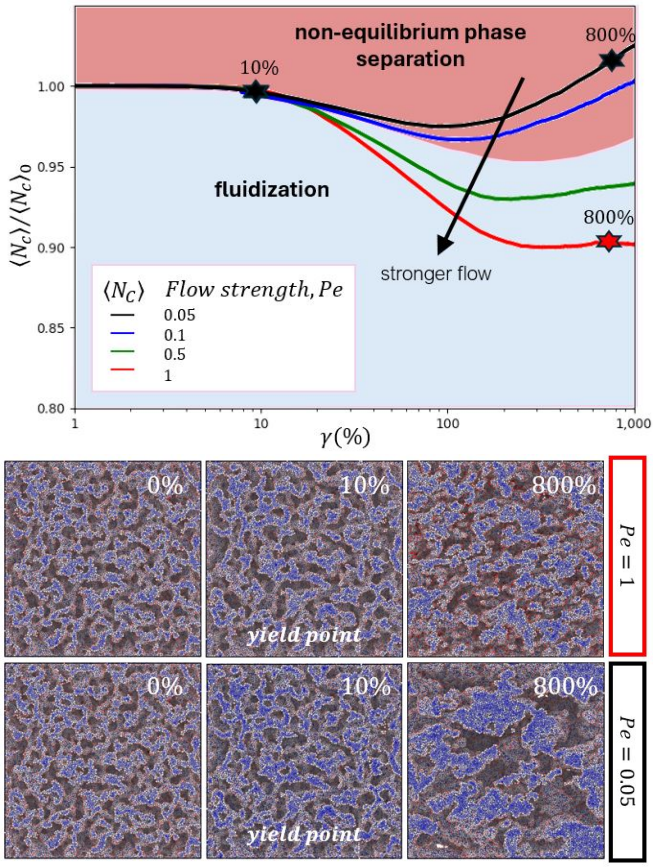

Figure 5.19. Microstructure snapshots for two different strain levels and $Pe = 1$ (upper row of left panel), as well as $Pe = 0.05$ (lower row of left panel). Average normalized number of contacts as a function of strain for different Pe values (right panel). The asterisks denote the deformation levels shown in the snapshots.

yield point, the network shows no noticeable difference compared to its state prior to the start-up. Well after the yield, following the overshoot in the stress response, pronounced structural evolution at the network-length

scale emerges. The flow strength influences the structural alignment, and the network length scale changes in two different ways, as shown in the rightmost images. For a weaker flow, $Pe = 0.05$, the network appears to remain connected, with some pores enlarging and the particle strands condensing into slightly larger, thicker structures aligned with the flow direction. This indicates that the gel does not transition into a dispersion-like state; instead, it maintains large, partially connected structures. However, for $Pe = 1$, the structural image reveals significant coarsening compared to the initial state. At this Pe number, the gel undergoes shear-induced restructuring, where the flow promotes the densification of the particle strands, resulting in a more heterogeneous gel morphology.

These microstructural changes are further verified by the plot of the average normalized contact number, which reflects bond formation or loss. Across the range of applied flow strengths, two distinct terminal regimes emerge. For Peclet numbers close to one, bond loss begins at 10% strain, leading to a decrease in the number of contacts before eventually stabilizing. This behavior is indicative of the viscous characteristics of a liquid. In contrast, under weaker flows ($Pe = 0.05, 0.1$), a different response is observed. Following the initial bond rupture, the flow facilitates the reformation of bonds, leading to flow-induced coarsening of the structure and resulting in a non-equilibrium phase separation. This behavior resembles the restructuring process taking place during the phase separation of a gel under quiescent conditions, as shown in chapter 4. However, in this case, the applied flow amplifies the process, leading to even more coarsened gel structures, as verified by the snapshots.

We derived some key insights from our previous study on the relationship between bond dynamics, microstructure, and rheology, during the application of a start-up flow. Our focus was on flows at relatively low Pe numbers, which do not completely break down the structure, but significantly influence the energy and structural evolution of the gel. In this second phase of our analysis on start-up flows, we will interpret results from BD simulations across various parameters, including volume fractions, attraction strengths, as well as shear rates and ages.

Fig. 5.20 shows start-up flow measurements taken from BD simulations at different Pe values for three volume fractions of $\phi = 0.2, 0.4$ and 0.5, constant attraction strength $-4k_BT$, and two different ages. First, we

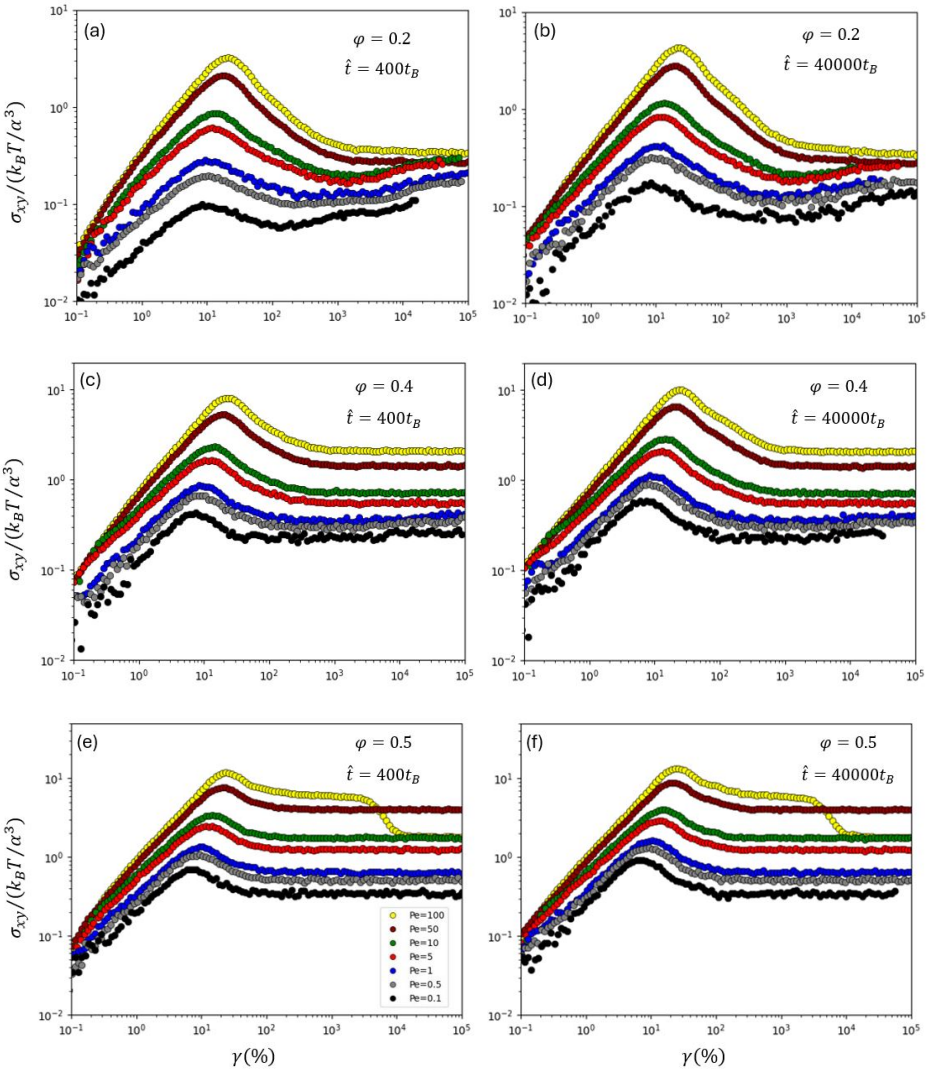

Figure 5.20. Start-up shear flow measurements from BD simulations at different Pe numbers as indicated for the gel with $U_{dep} = -4k_BT$ and (a) $\phi = 0.2$ at the age of $400t_B$, (b) $\phi = 0.2$ at the age of $40000t_B$, (c) $\phi = 0.4$ at the age of $400t_B$, (d) $\phi = 0.4$ at the age of $40000t_B$, (e) $\phi = 0.5$ at the age of $400t_B$, and (f) $\phi = 0.5$ at the age of $40000t_B$.

discuss the results for young and low-particle volume fraction ($\phi = 0.2$) gels (fig. 5.20(a)). In the range of shear rates examined here, the relationship between stress and strain reveals a peak known as the yielding point. In some works, this yielding point has been related to the disconnection of the links between clusters [49, 55]. However, Johnson et al. [43] interpreted this overshoot as a transition from energy storage to energy dissipation, rather than the occurrence of significant changes in the microstructure. This transition takes place while the network remains fully intact; only a small fraction of bonds needs to break to ease the glassy frustration of the particles. This phenomenon leads to a type of rheological yield, which we also observed in our results.

The long-time behavior following the stress overshoot reveals two distinct shear regimes. At low shear rates ($0.1 \leq Pe \leq 10$), a rise of stress is observed for strains exceeding approximately 100%. This increase in stress at large strains is attributed to cluster densification under shear, as discussed in the previous section. As clusters grow larger, they provide greater resistance to flow, resulting in an increase in stress. In contrast, at higher shear rates ($Pe \geq 50$), this stress increase at large strains is suppressed, leading to the emergence of a stress plateau. For higher volume fractions ($\phi = 0.4, 0.5$), cluster densification is not observed; instead, the stress overshoot immediately transitions to a constant stress value. Notably, at $\phi = 0.5$ and $Pe = 100$, a sudden decrease in the stress response occurs at higher deformation values. This drop is an artifact stemming from the absence of hydrodynamic interactions in our simulations, which causes particle layering and, consequently, a significant reduction in stress values.

A secondary yield or second overshoot, observed experimentally in dense, reversible gels [49, 55] is not present in the post-yield response of our results. One possible explanation is that a secondary yield may occur if the structural growth from flow-induced coarsening—following the first overshoot—breaks, thereby forming a second overshoot. It is also plausible that hydrodynamic interactions, which are not accounted for in this study, contribute to the breakdown of structures formed after the first yield peak due to flow-induced coarsening.

In fig. 5.21, we illustrate the effect of aging time at two different Pe values, representing weak and strong flows. In both cases, aging time re-

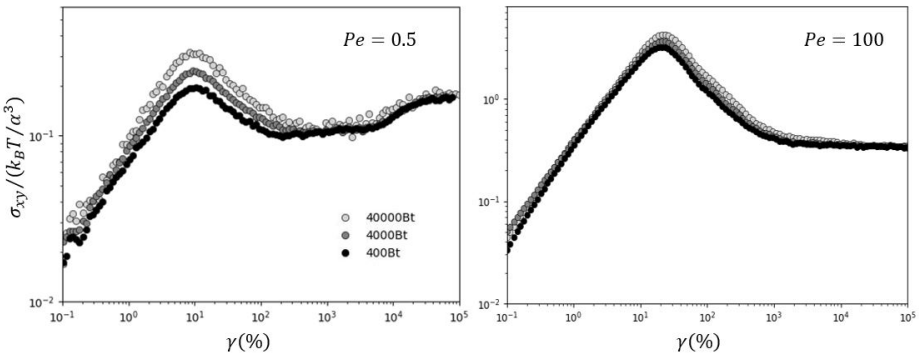

Figure 5.21. Start-up shear flow measurements from BD simulations for two different Pe values at different ages as indicated, for the gel with $\phi = 0.4$ and $U_{dep} = -4k_BT$.

sults in a vertical shift of the curves in the pre-yield and yield regime, while the curves converge in the terminal region. As the gel becomes stiffer over time, it is expected that its yield stress will increase, requiring a greater applied stress to achieve rheological yield. In the terminal regime, where high applied deformation leads to structural breakdown, the stress response remains the same regardless of aging time.

We now examine the effect of attraction strength on the yielding behavior of our gels under start-up flows. Fig 5.22 shows the shear start-up flows for gels with $\phi = 0.2$ at two different aging times and attraction strengths of $-4k_BT$ and $-16k_BT$. Notably, the stronger gel exhibits a higher stress response compared to the weaker gel with the most significant difference occurring in the terminal regime. In this region, the steady-state stress values differ by nearly an order of magnitude, while the peak stresses of both gels are relatively similar. Additionally, for the gel with $-16kBT$ attraction strength, we observe an increase in stress at large deformation values across all investigated Pe numbers. In contrast, the $-4kBT$ gel reaches a plateau in stress at high Pe. This signifies that cluster densification can occur in the stronger gel over a wider range of flow strengths, as shown in the lower panels of fig. 5.22. Finally, there is a slight horizontal shift of the peak stress for the stronger gel, indicating that yielding occurs at smaller strains compared to the weaker gel.

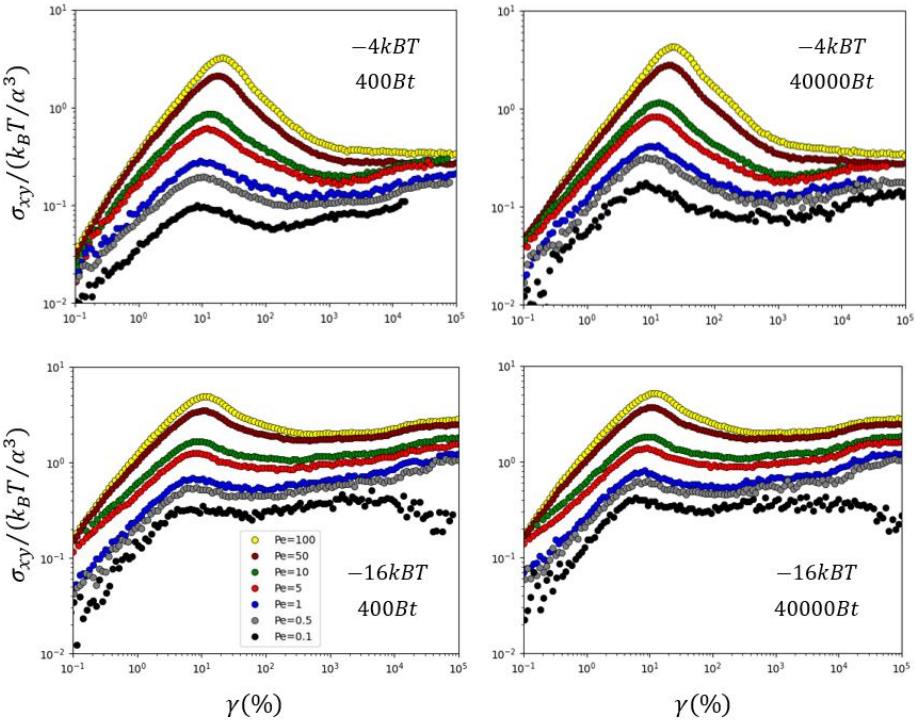

Figure 5.22. Start-up flow measurements taken from BD simulations for different Pe values as indicated, at two different aging times, 400 and $40000t_B$, and two different attraction strengths, $-4k_BT$ and $-16k_BT$.

Creep tests

Fabric enhancers can be subjected to stresses during manufacturing, transportation or consumer use. Therefore, understanding how these gels respond to varying stress levels is crucial. Additionally, creep tests offer an alternative method for estimating the yield stress of these materials, a property that is vital for the stability of LFEs, as previously discussed.

The yield stress of such materials is relatively low, approximately $0.01Pa$. Therefore, we investigate stress levels ranging from $0.005Pa \leq \sigma_{xy} \leq 1Pa$, to capture the full spectrum of the gel's behavior, from solid-like to viscous-dominated. One effective method for assessing the response of complex fluids is by measuring their deviation from the ideal elastic response, quanti-

fied here by the creep compliance, $J(\Delta t) = \gamma(\Delta t)/\sigma_{xy}$, where γ represents the deformation and Δt is the time elapsed after the stress application. As the material becomes more compliant, it softens, indicating a transition from solid-like to liquid-like behavior.

In this study, we monitored the temporal evolution of the creep compliance over an aging period of $400\alpha^2/D$. The plotted curves (fig. 5.23) represent a range of applied stress values, made dimensionless using the Brownian stress. At early times, the creep compliance is independent of

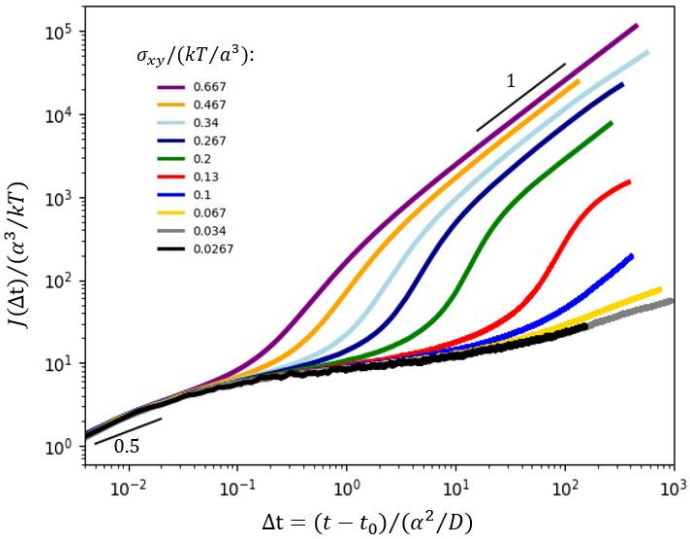

Figure 5.23. Creep compliance normalized with the inverse of the Brownian stress as a function of time for different Pe values shown in the legend.

the applied stress and scales with the square root of time, $J(\Delta t) \sim (\Delta t)^{1/2}$, regardless of gel age. This stress insensitivity suggests that no structural deformation occurs during these short times. As time progresses, a rapid increase in creep compliance is observed, marking a shift from elastic to viscous-dominated behavior. Prior to this transition, there is a delay period that decreases as the applied stress increases. For the weakest stresses, the transition may not occur at all, indicating long-term creep without yielding.

To identify the different regimes that the gel goes through under the

application of a shear stress, we track the temporal evolution of the deformation rate (fig. 5.24). The rate of deformation can exhibit two extreme behaviors: that of a Newtonian solvent, which appears as a horizontal line, and that of an elastic solid, which decays exponentially to zero. In the case of a solid, deformation occurs instantaneously, whereas a liquid continues to deform at a constant rate after the shear stress is applied.

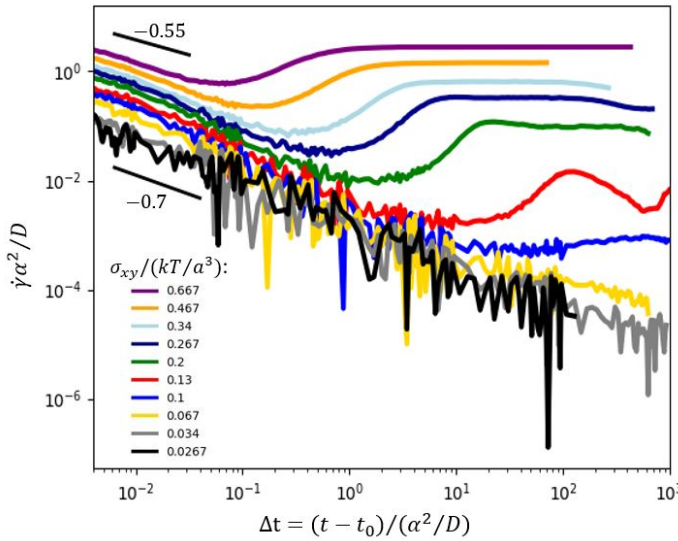

Figure 5.24. Rate of deformation normalized with the Brownian time as a function of time for different applied stresses.

The curves display an intermediate behavior that depends on the applied stress. Initially, the gel deforms at a rate that decreases over time, which is characteristic of a solid-like response. Power-law fits to the curves, $\dot{\gamma} \sim (\Delta t)^{-\beta}$, are shown on the plots. Under weak stresses, this creeping behavior persists throughout the entire time window examined, with a monotonic decrease in shear rate. However, at intermediate stresses, a change in the slope occurs. This shift from a negative to a positive slope corresponds to the gel's yielding, marking the yield point. After yielding, when a higher stress is applied, a plateau forms, indicating viscous flow. The duration of the plateau increases with higher stress levels. Interestingly, at intermediate stress levels, after a brief plateau—such as in the

case of $\sigma_{xy}/(kT/\alpha^3) = 0.13$—the deformation rate slows again, signaling a re-entrant solid-like phase.

To illustrate these states, we provide snapshots of the microstructure at various times (fig. 5.25) under the same applied stress. We chose

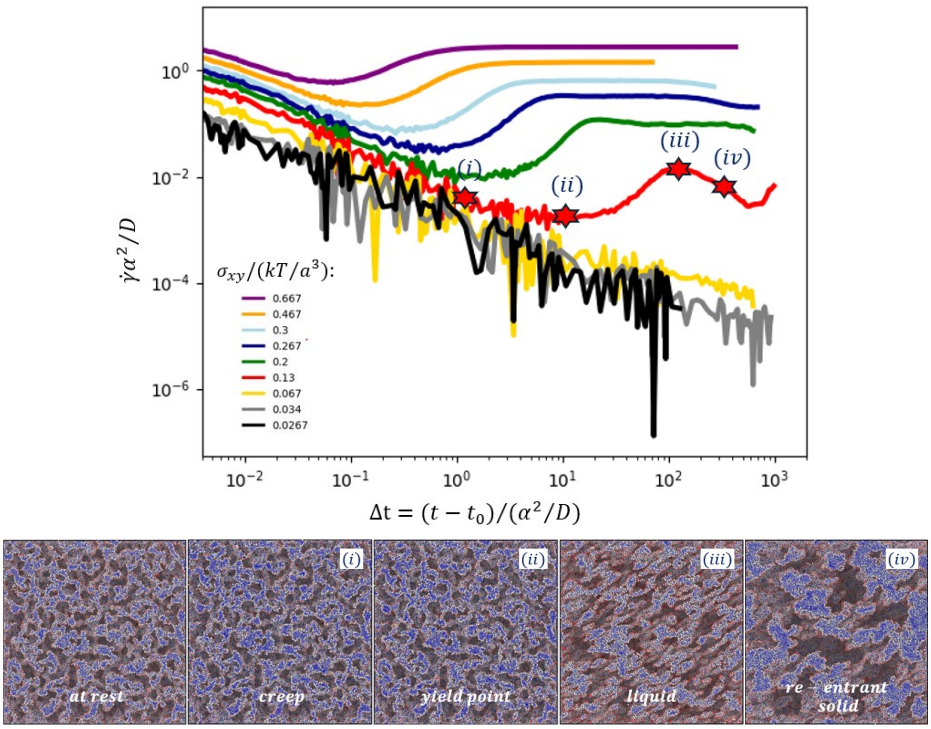

Figure 5.25. Rate of deformation normalized with the Brownian time as a function of time for different applied stress levels (top plot) accompanied by snapshots of the microstructure at times marked by asterisks.

$\sigma_{xy}/(kT/\alpha^3) = 0.13$, as this stress level allows the gel to exhibit all the distinct behaviors. Initially, the gel deforms like a solid until it reaches $t/(\alpha^2/D) = 10$, at which point it yields. After yielding, it flows briefly before resolidifying. The snapshots align with our predictions. Notably, at the yield point, there is no significant change in the microstructure, similar to what we observed during yielding after weak start-up flows. This suggests that only a small number of bond breakages are necessary to re-

lax other bonds, alleviating the glassy frustration of particles within the clusters. At $t/(\alpha^2/D) = 100$ (snapshot (iii)), the clusters align with the imposed flow, indicating viscous behavior, while at $t/(\alpha^2/D) = 300$ (snapshot (iv)), shear-induced coarsening becomes evident.

As we previously mentioned, creep tests constitute another way of measuring the gel yield stress. This can be extracted from the creep compliance plot (fig 5.23) as the value of stress where the system transitions from the linear regime (curves collapsing) to the non-linear regime (curves start peeling away from one another). In our case, we define $\sigma_{xy}/(kT/\alpha^3) \simeq 0.1$ as the gel yield stress. This value can now be compared to the dynamic yield stress obtained from the flow curve.

Unifying start-up flows with creep tests

In figure 5.26, we show the flow curve for our gel with $\phi = 0.4$ (red circles), along with the steady-state shear values (blue asterisks) derived from the creep tests. In a creep test, the system only reaches a steady-state in the viscous regime (at high applied stresses), while at lower stresses, the rate of deformation continues to evolve, and a steady state is never attained. In the viscous flow region, both types of tests result in the same steady-state values, in terms of shear rate or stress response.

The dynamic and creep yield stress values are similar; below these values, both tests predict that the gel will not yield, but instead maintain its solid-like response. The resolidification regime is defined from the rate of deformation plot (fig. 5.24), within the stress range where a second decay occurs, signifying a re-entrant solid process. In our gel, this regime extends above the dynamic yield stress plateau, in contrast with a previous study presented in section 1.8.3 [66], where it extended below the yield stress plateau. However, as can be seen from the start-up flows at small Pe (fig. 5.27), and our previous study of gel's terminal behavior under weak flows (fig. 5.19), both the stress and the average contact number increase over time, signifying a cluster densification and in turn, a restructuring (coarsening) process. We conclude that the start-up flows and the creep tests can be unified in a single plot, since both predict the same types of behavior: solid-like response, viscous flow, or resolidification for the same flow conditions (Pe and stress values).

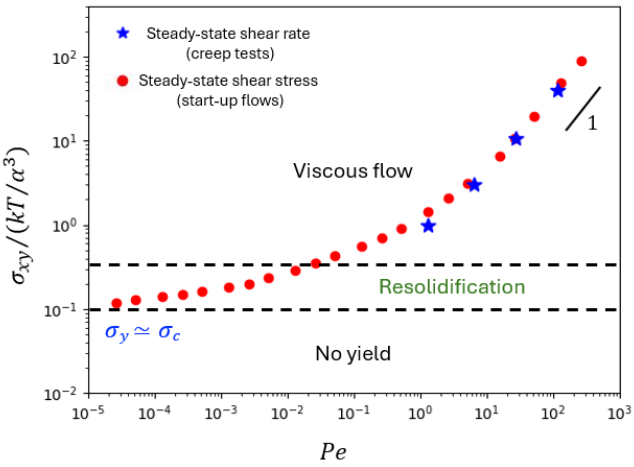

Figure 5.26. Steady shear stress response as a function of Pe derived from constant shear rate measurements (red circles). Steady shear response at different applied shear stresses taken from creep tests (blue asterisks). The dashed lines represent the borderlines between the different reported regimes. Results for a gel with $\phi = 0.4$, and $U_{dep} = -4k_BT$.

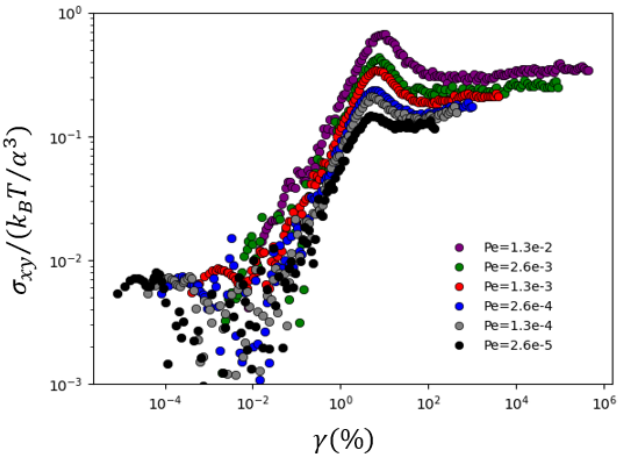

Figure 5.27. Start-up flows as a function of deformation for low Pe values, that correspond to the resolidification regime according to fig. 5.26.

Chapter 6

Conclusions

In this dissertation, we examined the microscopic dynamics and rheological properties of colloidal depletion gels that are relevant in industrial applications, i.e., fabric enhancers. Our study employed a combination of rheometry, Differential Dynamic Microscopy measurements, and computer simulations. We focused on two experimental systems: the first, a vesicular dispersion, forms the basis of LFEs, while the second system is obtained through mixing of the white bases with non-adsorbing polymer chains, representing the structural gel network found in fabric enhancers.

The investigation of the thermal dynamics of vesicle dispersions by means of Brownian Dynamics simulations revealed that parameters like particle volume fraction and salt content significantly affect the relaxation dynamics. In particular, at high salt concentrations—where the EDL interactions are weaker and shorter-range—glassy dynamics were observed at the upper boundary of the explored volume fraction. In contrast, at the lowest salt concentration, the onset of glassy dynamics occurred at a volume fraction of approximately $\phi \simeq 0.15$, which is notably smaller than that found for hard-spheres. The hallmark of this glassiness was the appearance of a plateau in both SISF and MSD during intermediate times, separating a ballistic from a Fickian diffusive regime. This behavior is explained through the cage-jump model: early relaxation is caused by particles rattling within cages formed by neighboring particles, while the later relaxation is due to particles escaping from their cages through diffusion. Overall, our results suggest that charged vesicle suspensions can be con-

sidered as Wigner glasses, where the glass transition can occur even in low-density suspensions due to the presence of long-range interactions.

The same system was also studied through DDM experiments, focusing on its thermal dynamics across various length scales and concentration regimes. In the dilute regime, we observed two distinct diffusive processes at different wavevector ranges, each corresponding to the diffusion of particles with specific sizes. At lower q values, larger particles with a radius of $R_1 = 2\mu m$ were detected, while at higher q values, smaller particles of size $R_2 = 1\mu m$ dominated the signal, in line with scattering theory predictions. In concentrated samples, we identified two regimes with different dynamics, separated by the typical cage size $q^\star$. For wavevectors larger than $q*$, the in cage diffusive dynamics is observed, characterized by a concentration-dependent diffusion coefficient. At larger length scales, the intermediate scattering function showed partial decorrelation with a constant characteristic time and a monotonically increasing amplitude, associated with the in cage motion, along with a second subdiffusive decorrelation process. This second process represents the terminal relaxation of vesicles, as it corresponds to length scales significantly larger than the particle size.

The main focus of this dissertation, however, includes the development of a simulation framework that accurately captures the rheological and yielding behavior of charged vesicle gels under various rheological tests. These tests include steady and oscillatory shear flows, as well as the application of shear stresses. In the linear viscoelastic regime, both experiments and simulations revealed a solid-like response of our gels, as expected for colloidal depletion gels at volume fractions of $\phi = 0.4 - 0.55$. By conducting strain sweeps, we examined both the linear and non-linear responses of our material. In the linear regime, the viscoelastic moduli showed an initial amplitude-independent plateau, followed by their crossover, and a subsequent viscous region where $G'' > G'$. In both simulations and experiments, we observed a yielding point before the crossover, marked by a local maximum of G'', typically attributed to the disconnection of large weakly connected clusters. A second yielding point, as noted by previous experiments [49], was observed only in the experiments of the gel with $\phi = 0.55$, indicating intra-cluster bond breakage. Additionally, our flow curves showed the characteristic yield stress behavior, consistent with colloidal depletion gels at these volume fractions. The simulations closely

match the experimental data with the formation of a plateau at low Pe, signaling the presence of a dynamic yield stress. This plateau is followed by a sublinear stress growth, indicative of a shear-thinning response, that gives way to a pure Newtonian scaling at even larger Pe.

BD simulations can, additionally, provide detailed structural images and allow for structural characterization through the measurement of quantities like the number of contacts. Both oscillatory and steady shear flow tests have similar effects on gel's morphology. At low Pe numbers or strain amplitudes γ_0, the gel structure is comparable to a quiescently aged gel. As the flow strength increases, shear-induced coarsening occurs, leading to denser particle clusters, and the enlargement of the colloid-poor voids. This increased heterogeneity is eventually disrupted under even stronger deformation, where the gel structure breaks down completely, resulting in a homogeneous particle distribution in the solvent. Interestingly, we found that while the increase in heterogeneity at intermediate Pe values was not reflected by the average number of contacts, it was captured by its variance, exhibiting a peak at the Pe with the highest heterogeneity, in agreement with the snapshots.

An extensive section of the study focused on the yielding properties of depletion gels under steady-shear flows and stresses. The temporal evolution of shear stress under the application of a constant shear rate revealed the emergence of three distinct regimes: i) an initial stress growth, where energy is stored both enthalpically (through bond stretching) and entropically (due to microstructural deformation), ii) a second yield regime, where the stress reaches a peak value, marking the static yield stress for the given Pe. At this point energy storage shifts to energy dissipation. And iii) the final regime, where the stress decreases and levels off to a plateau, indicative of the gel yield and its viscous flow.

A creep test can be useful for the estimation of our gels' yield stress, as well as the identification of the different behaviors that a gel exhibits under constant shear stress. The yield stress is defined as the stress, at which the creep compliance curves begin to diverge from the others within the observed time window. This divergence marks the system's transition from a linear to a non-linear response, which occurs after a certain delay time, that shortens as stress increases. By tracking the deformation rate over time under a wide range of applied stresses, three behaviors were

identified: i) when the applied stress is below the yield stress, the gel undergoes a creeping solid-like deformation that never transitions to yield, ii) if the applied stress is much higher, then after the initial solid-like regime, yielding occurs, characterized by a shift from a negative to a positive slope, eventually stabilizing at a plateau, indicative of viscous flow. However, at intermediate stresses, iii) after yielding, a temporary plateau forms, followed again by a decrease in the deformation rate, signaling a re-entrant solid behavior.

The gel's behavior as predicted by creep tests, aligns well with the results from start-up flows. Both tests indicate that the gel behaves like a solid below a certain yield stress, without yielding, and this critical stress is consistent across both testing methods. In the regime where the steady-state stress from start-up flows matches the steady-state shear rate from creep tests, the gel undergoes viscous flow. Additionally, both tests show a resolidification regime within the same Pe number range, where the gel experiences structural changes, resulting in increased heterogeneity over time.

Our modeling framework effectively captures the rheological behavior of LFEs under shear flows and stresses, using parameters that match real formulations. As a perspective, this model could be extended to include additional rheological tests, such as shear cessation or step strain tests, as well as different operating conditions and system parameters. Having a model that can accurately compute key properties, like the yield stress, the viscosity, or the viscoelasticity, while providing detailed structural insights, would be a valuable tool for the desing of LFEs with improved mechanical properties.

Bibliography

[1] D G A L Aarts, R Tuinier, and H N W Lekkerkerker. Phase behaviour of mixtures of colloidal spheres and excluded-volume polymer chains. *Journal of Physics: Condensed Matter*, 14(33):7551–7561, August 2002.

[2] Sho Asakura and Fumio Oosawa. On interaction between two bodies immersed in a solution of macromolecules. *The Journal of Chemical Physics*, 22(7):1255–1256, July 1954.

[3] Phil Attard. Recent advances in the electric double layer in colloid science. *Current Opinion in Colloid amp; Interface Science*, 6(4):366–371, August 2001.

[4] Pierre Ballesta, Nick Koumakis, Rut Besseling, Wilson C. K. Poon, and George Petekidis. Slip of gels in colloid–polymer mixtures under shear. *Soft Matter*, 9(12):3237, 2013.

[5] Howard A. Barnes. The yield stress—a review or 'παντα ρει'—everything flows? *Journal of Non-Newtonian Fluid Mechanics*, 81(1–2):133–178, February 1999.

[6] Alexandra V. Bayles, Todd M. Squires, and Matthew E. Helgeson. Dark-field differential dynamic microscopy. *Soft Matter*, 12(8):2440–2452, 2016.

[7] J. Bergenholtz and M. Fuchs. Nonergodicity transitions in colloidal suspensions with attractive interactions. *Physical Review E*, 59(5):5706–5715, May 1999.

[8] J. Bergenholtz, W. C. K. Poon, and M. Fuchs. Gelation in model colloid-polymer mixtures. *Langmuir*, 19(10):4493–4503, April 2003.

[9] Daniel Bonn and Morton M. Denn. Yield stress fluids slowly yield to analysis. *Science*, 324(5933):1401–1402, June 2009.

[10] J. Bosse and S. D. Wilke. Low-density ionic glass. *Physical Review Letters*, 80(6):1260–1263, February 1998.

[11] G. Brambilla, D. El Masri, M. Pierno, L. Berthier, L. Cipelletti, G. Petekidis, and A. B. Schofield. Probing the equilibrium dynamics of colloidal hard spheres above the mode-coupling glass transition. *Physical Review Letters*, 102(8):085703, February 2009.

[12] Marco Caggioni, Veronique Trappe, and Patrick T. Spicer. Variations of the herschel–bulkley exponent reflecting contributions of the viscous continuous phase to the shear rate-dependent stress of soft glassy materials. *Journal of Rheology*, 64(2):413–422, March 2020.

[13] Marina Carpineti and Marzio Giglio. Spinodal-type dynamics in fractal aggregation of colloidal clusters. *Physical Review Letters*, 68(22):3327–3330, June 1992.

[14] M E Cates, M Fuchs, K Kroy, W C K Poon, and A M Puertas. Theory and simulation of gelation, arrest and yielding in attracting colloids. *Journal of Physics: Condensed Matter*, 16(42):S4861–S4875, October 2004.

[15] Roberto Cerbino, Fabio Giavazzi, and Matthew E. Helgeson. Differential dynamic microscopy for the characterization of polymer systems. *Journal of Polymer Science*, 60(7):1079–1089, June 2021.

[16] Roberto Cerbino and Veronique Trappe. Differential dynamic microscopy: Probing wave vector dependent dynamics with a microscope. *Physical Review Letters*, 100(18):188102, May 2008.

[17] Gregor Cevc. Lipid vesicles and other colloids as drug carriers on the skin. *Advanced Drug Delivery Reviews*, 56(5):675–711, March 2004.

[18] Hubert K. Chan and Ali Mohraz. Two-step yielding and directional strain-induced strengthening in dilute colloidal gels. *Physical Review E*, 85(4):041403, April 2012.

[19] Yeng-Long Chen and Kenneth S. Schweizer. Microscopic theory of gelation and elasticity in polymer–particle suspensions. *The Journal of Chemical Physics*, 120(15):7212–7222, April 2004.

[20] Massimo Pica Ciamarra, Raffaele Pastore, and Antonio Coniglio. Particle jumps in structural glasses. *Soft Matter*, 12(2):358–366, 2016.

[21] Jacinta C. Conrad and Jennifer A. Lewis. Structure of colloidal gels during microchannel flow. *Langmuir*, 24(15):7628–7634, June 2008.

[22] Ke-Ming Corominas, KM Quan, Yunpeng Yang, and Kenny Peers. Method of producing a fabric softener composition. *US Patent App. 12/984,663*, 2014.

[23] Edwin-Joffrey Courtial, Clément Perrinet, Arthur Colly, David Mariot, Jean-Marc Frances, René Fulchiron, and Christophe Marquette. Silicone rheological behavior modification for 3d printing: Evaluation of yield stress impact on printed object properties. *Additive Manufacturing*, 28:50–57, August 2019.

[24] P. Coussot and J. M. Piau. On the behavior of fine mud suspensions. *Rheologica Acta*, 33(3):175–184, 1994.

[25] K. Dawson, G. Foffi, M. Fuchs, W. Götze, F. Sciortino, M. Sperl, P. Tartaglia, Th. Voigtmann, and E. Zaccarelli. Higher-order glass-transition singularities in colloidal systems with attractive interactions. *Physical Review E*, 63(1):011401, December 2000.

[26] B. Derjaguin. On the repulsive forces between charged colloid particles and on the theory of slow coagulation and stability of lyophobe sols. *Transactions of the Faraday Society*, 35:203, 1940.

[27] Clare J. Dibble, Michael Kogan, and Michael J. Solomon. Structure and dynamics of colloidal depletion gels: Coincidence of transitions and heterogeneity. *Physical Review E*, 74(4):041403, October 2006.

[28] T. Eckert and E. Bartsch. Re-entrant glass transition in a colloid-polymer mixture with depletion attractions. *Physical Review Letters*, 89(12):125701, August 2002.

[29] Paolo Edera, Matteo Brizioli, Giuliano Zanchetta, George Petekidis, Fabio Giavazzi, and Roberto Cerbino. Deformation profiles and microscopic dynamics of complex fluids during oscillatory shear experiments. *Soft Matter*, 17(37):8553–8566, 2021.

[30] Eugene c. Bingham. *Fluidity And Plasticity.* Mcgraw-Hill Book Company,Inc., 1922.

[31] L. Fabbian, W. Götze, F. Sciortino, P. Tartaglia, and F. Thiery. Ideal glass-glass transitions and logarithmic decay of correlations in a simple system. *Physical Review E*, 59(2):R1347–R1350, February 1999.

[32] S M Fielding. Shear banding in soft glassy materials. *Reports on Progress in Physics*, 77(10):102601, October 2014.

[33] Gerard J. Fleer and Remco Tuinier. Analytical phase diagram for colloid-polymer mixtures. *Physical Review E*, 76(4):041802, October 2007.

[34] Yongxiang Gao, Juntae Kim, and Matthew E. Helgeson. Microdynamics and arrest of coarsening during spinodal decomposition in thermoreversible colloidal gels. *Soft Matter*, 11(32):6360–6370, 2015.

[35] Fabio Giavazzi, Paolo Edera, Peter J. Lu, and Roberto Cerbino. Image windowing mitigates edge effects in differential dynamic microscopy. *The European Physical Journal E*, 40(11), November 2017.

[36] M. C. Grant and W. B. Russel. Volume-fraction dependence of elastic moduli and transition temperatures for colloidal silica gels. *Physical Review E*, 47(4):2606–2614, April 1993.

[37] Vincenzo Guida. Thermodynamics and kinetics of vesicles formation processes. *Advances in Colloid and Interface Science*, 161(1):77–88, 2010. Physico-chemical and flow behaviour of droplet based systems.

[38] Jean-Pierre Hansen and I. R. McDonald. *Theory of Simple Liquids: with Applications to Soft Matter*. Academic Press, August 2013. Google-Books-ID: BEuYUhaDvIgC.

[39] R. Harich, T. W. Blythe, M. Hermes, E. Zaccarelli, A. J. Sederman, L. F. Gladden, and W. C. K. Poon. Gravitational collapse of depletion-induced colloidal gels. *Soft Matter*, 12(19):4300–4308, 2016.

[40] Winslow H. Herschel and Ronald Bulkley. Konsistenzmessungen von gummi-benzollösungen. *Kolloid-Zeitschrift*, 39(4):291–300, August 1926.

[41] Jacob N. Israelachvili. *Intermolecular and Surface Forces*. Academic Press, July 2011.

[42] Sara Jabbari-Farouji, Gerard H. Wegdam, and Daniel Bonn. Gels and glasses in a single system: Evidence for an intricate free-energy landscape of glassy materials. *Physical Review Letters*, 99(6):065701, August 2007.

[43] Lilian C. Johnson, Benjamin J. Landrum, and Roseanna N. Zia. Yield of reversible colloidal gels during flow start-up: release from kinetic arrest. *Soft Matter*, 14(24):5048–5068, 2018.

[44] Lilian C. Johnson, Roseanna N. Zia, Esmaeel Moghimi, and George Petekidis. Influence of structure on the linear response rheology of colloidal gels. *Journal of Rheology*, 63(4):583–608, May 2019.

[45] Fardin Khabaz, Bruno Flavio Di Dio, Michel Cloitre, and Roger T. Bonnecaze. Transient dynamics of soft particle glasses in startup shear flow. part i: Microstructure and time scales. *Journal of Rheology*, 65(2):241–255, March 2021.

[46] Juntae Kim, Dimitri Merger, Manfred Wilhelm, and Matthew E. Helgeson. Microstructure and nonlinear signatures of yielding in a heterogeneous colloidal gel under large amplitude oscillatory shear. *Journal of Rheology*, 58(5):1359–1390, September 2014.

[47] N. Koumakis, M. Laurati, S. U. Egelhaaf, J. F. Brady, and G. Petekidis. Yielding of hard-sphere glasses during start-up shear. *Physical Review Letters*, 108(9):098303, March 2012.

[48] N. Koumakis, M. Laurati, A. R. Jacob, K. J. Mutch, A. Abdellali, A. B. Schofield, S. U. Egelhaaf, J. F. Brady, and G. Petekidis. Start-up shear of concentrated colloidal hard spheres: Stresses, dynamics, and structure. *Journal of Rheology*, 60(4):603–623, May 2016.

[49] N. Koumakis and G. Petekidis. Two step yielding in attractive colloids: transition from gels to attractive glasses. *Soft Matter*, 7(6):2456, 2011.

[50] N. Koumakis, A. B. Schofield, and G. Petekidis. Effects of shear induced crystallization on the rheology and ageing of hard sphere glasses. *Soft Matter*, 4(10):2008, 2008.

[51] Nick Koumakis, Esmaeel Moghimi, Rut Besseling, Wilson C. K. Poon, John F. Brady, and George Petekidis. Tuning colloidal gels by shear. *Soft Matter*, 11(23):4640–4648, 2015.

[52] Takehito Koyama and Hajime Tanaka. Volume-shrinking kinetics of transient gels as a consequence of dynamic interplay between phase separation and mechanical relaxation. *Physical Review E*, 98(6):062617, December 2018.

[53] Benjamin J. Landrum, William B. Russel, and Roseanna N. Zia. Delayed yield in colloidal gels: Creep, flow, and re-entrant solid regimes. *Journal of Rheology*, 60(4):783–807, June 2016.

[54] Ronald G. Larson. *The Structure and Rheology of Complex Fluids*. OUP USA, January 1999. Google-Books-ID: Vt9fw_pf1LUC.

[55] M. Laurati, S. U. Egelhaaf, and G. Petekidis. Nonlinear rheology of colloidal gels with intermediate volume fraction. *Journal of Rheology*, 55(3):673–706, May 2011.

[56] M. Laurati, G. Petekidis, N. Koumakis, F. Cardinaux, A. B. Schofield, J. M. Brader, M. Fuchs, and S. U. Egelhaaf. Structure, dynamics, and rheology of colloid-polymer mixtures: From liquids to gels. *The Journal of Chemical Physics*, 130(13), April 2009.

[57] Matthew Leivers, John M. Seddon, Marc Declercq, Eric Robles, and Paul Luckham. Measurement of forces between supported cationic bilayers by colloid probe atomic force microscopy: Electrolyte concentration and composition. *Langmuir*, 35(3):729–738, December 2018.

[58] H. M. Lindsay and P. M. Chaikin. Elastic properties of colloidal crystals and glasses. *The Journal of Chemical Physics*, 76(7):3774–3781, April 1982.

[59] Stefan B. Lindström, Thomas E. Kodger, Joris Sprakel, and David A. Weitz. Structures, stresses, and fluctuations in the delayed failure of colloidal gels. *Soft Matter*, 8(13):3657, 2012.

[60] Peter J. Lu, Emanuela Zaccarelli, Fabio Ciulla, Andrew B. Schofield, Francesco Sciortino, and David A. Weitz. Gelation of particles with short-range attraction. *Nature*, 453(7194):499–503, May 2008.

[61] S. Manley, J. M. Skotheim, L. Mahadevan, and D. A. Weitz. Gravitational collapse of colloidal gels. *Physical Review Letters*, 94(21):218302, June 2005.

[62] T. G. Mason and D. A. Weitz. Linear viscoelasticity of colloidal hard sphere suspensions near the glass transition. *Physical Review Letters*, 75(14):2770–2773, October 1995.

[63] Kasper Masschaele, Jan Fransaer, and Jan Vermant. Direct visualization of yielding in model two-dimensional colloidal gels subjected to shear flow. *Journal of Rheology*, 53(6):1437–1460, November 2009.

[64] Jan Mewis and Norman J. Wagner. *Colloidal Suspension Rheology*. Cambridge Series in Chemical Engineering. Cambridge University Press, Cambridge, 2011.

[65] Esmaeel Moghimi, Alan R. Jacob, Nick Koumakis, and George Petekidis. Colloidal gels tuned by oscillatory shear. *Soft Matter*, 13(12):2371–2383, 2017.

[66] Esmaeel Moghimi, Andrew B Schofield, and George Petekidis. Yielding and resolidification of colloidal gels under constant stress. *Journal of Physics: Condensed Matter*, 33(28):284002, June 2021.

[67] Chinedum O. Osuji, Chanjoong Kim, and David A. Weitz. Shear thickening and scaling of the elastic modulus in a fractal colloidal system with attractive interactions. *Physical Review E*, 77(6):060402, June 2008.

[68] John P. Pantina and Eric M. Furst. Elasticity and critical bending moment of model colloidal aggregates. *Physical Review Letters*, 94(13):138301, April 2005.

[69] Raffaele Pastore, Giuseppe Pesce, Antonio Sasso, and Massimo Pica Ciamarra. Many facets of intermittent dynamics in colloidal and molecular glasses. *Colloids and Surfaces A: Physicochemical and Engineering Aspects*, 532:87–96, November 2017.

[70] C. Patrick Royall, Stephen R. Williams, Takehiro Ohtsuka, and Hajime Tanaka. Direct observation of a local structural mechanism for dynamic arrest. *Nature Materials*, 7(7):556–561, June 2008.

[71] K. N. Pham, G. Petekidis, D. Vlassopoulos, S. U. Egelhaaf, W. C. K. Poon, and P. N. Pusey. Yielding behavior of repulsion- and attraction-dominated colloidal glasses. *Journal of Rheology*, 52(2):649–676, March 2008.

[72] K. N. Pham, A. M. Puertas, J. Bergenholtz, S. U. Egelhaaf, A. Moussaıd, P. N. Pusey, A. B. Schofield, M. E. Cates, M. Fuchs, and W. C. K. Poon. Multiple glassy states in a simple model system. *Science*, 296(5565):104–106, April 2002.

[73] Adrian-Marie Philippe, Domenico Truzzolillo, Julian Galvan-Myoshi, Philippe Dieudonné-George, Véronique Trappe, Ludovic Berthier, and Luca Cipelletti. Glass transition of soft colloids. *Physical Review E*, 97(4):040601, 2018.

[74] D. Pontoni, T. Narayanan, J.-M. Petit, G. Grübel, and D. Beysens. Microstructure and dynamics near an attractive colloidal glass transition. *Physical Review Letters*, 90(18):188301, May 2003.

[75] G Porpora, F Rusciano, V Guida, F Greco, and R Pastore. Understanding charged vesicle suspensions as wigner glasses: dynamical aspects. *Journal of Physics: Condensed Matter*, 33(10):104001, December 2020.

[76] Antonio M. Puertas, Matthias Fuchs, and Michael E. Cates. Comparative simulation study of colloidal gels and glasses. *Physical Review Letters*, 88(9):098301, February 2002.

[77] Antonio M. Puertas, Matthias Fuchs, and Michael E. Cates. Dynamical heterogeneities close to a colloidal gel. *The Journal of Chemical Physics*, 121(6):2813–2822, August 2004.

[78] P.N. Pusey, A.D. Pirie, and W.C.K. Poon. Dynamics of colloid-polymer mixtures. *Physica A: Statistical Mechanics and its Applications*, 201(1–3):322–331, December 1993.

[79] Srinivasa R. Raghavan and Saad A. Khan. Shear-induced microstructural changes in flocculated suspensions of fumed silica. *Journal of Rheology*, 39(6):1311–1325, November 1995.

[80] J. M. Rallison and E. J. Hinch. The effect of particle interactions on dynamic light scattering from a dilute suspension. *Journal of Fluid Mechanics*, 167(1):131, June 1986.

[81] S. Ramakrishnan, Y.-L. Chen, K. S. Schweizer, and C. F. Zukoski. Elasticity and clustering in concentrated depletion gels. *Physical Review E*, 70(4):040401, October 2004.

[82] William Bailey Russel, W. B. Russel, D. A. Saville, and W. R. Schowalter. *Colloidal Dispersions*. Cambridge University Press, 1991. Google-Books-ID: 3shp8Kl6YoUC.

[83] Francesco Sciortino. One liquid, two glasses. *Nature Materials*, 1(3):145–146, November 2002.

[84] Eleonora Secchi, Stefano Buzzaccaro, and Roberto Piazza. Time-evolution scenarios for short-range depletion gels subjected to the gravitational stress. *Soft Matter*, 10(29):5296, 2014.

[85] Mansi Seth, Arun Ramachandran, and L. Gary Leal. Dilution technique to determine the hydrodynamic volume fraction of a vesicle suspension. *Langmuir*, 26(19):15169–15176, August 2010.

[86] S. A. Shah, Y.-L Chen, K. S. Schweizer, and C. F. Zukoski. Viscoelasticity and rheology of depletion flocculated gels and fluids. *The Journal of Chemical Physics*, 119(16):8747–8760, October 2003.

[87] Zhen Shao, Ajay Singh Negi, and Chinedum O. Osuji. Role of interparticle attraction in the yielding response of microgel suspensions. *Soft Matter*, 9(22):5492, 2013.

[88] Asimina Sierou and John F. Brady. Accelerated stokesian dynamics simulations. *Journal of Fluid Mechanics*, 448:115–146, November 2001.

[89] Hajime Tanaka and Takeaki Araki. Simulation method of colloidal suspensions with hydrodynamic interactions: Fluid particle dynamics. *Physical Review Letters*, 85(6):1338–1341, August 2000.

[90] Aidan P. Thompson, H. Metin Aktulga, Richard Berger, Dan S. Bolintineanu, W. Michael Brown, Paul S. Crozier, Pieter J. in 't Veld, Axel Kohlmeyer, Stan G. Moore, Trung Dac Nguyen, Ray Shan, Mark J. Stevens, Julien Tranchida, Christian Trott, and Steven J. Plimpton. Lammps - a flexible simulation tool for particle-based materials modeling at the atomic, meso, and continuum scales. *Computer Physics Communications*, 271:108171, February 2022.

[91] Emma S. Thompson, Marc Declercq, Pieter Saveyn, Vincenzo Guida, Eric S.J. Robles, and Melanie M. Britton. Phase separation and collapse in almost density matched depletion induced colloidal gels in presence and absence of air bubbles: An mri imaging study. *Journal of Colloid and Interface Science*, 582:201–211, January 2021.

[92] V. Trappe, V. Prasad, Luca Cipelletti, P. N. Segre, and D. A. Weitz. Jamming phase diagram for attractive particles. *Nature*, 411(6839):772–775, June 2001.

[93] Nynke A.M. Verhaegh, Daniela Asnaghi, Henk N.W. Lekkerkerker, Marzio Giglio, and Luca Cipelletti. Transient gelation by spinodal decomposition in colloid-polymer mixtures. *Physica A: Statistical Mechanics and its Applications*, 242(1–2):104–118, August 1997.

[94] J Vermant and M J Solomon. Flow-induced structure in colloidal suspensions. *Journal of Physics: Condensed Matter*, 17(4):R187–R216, January 2005.

[95] Evert Johannes Willem Verwey, Jan Theodoor Gerard Overbeek, and K. van Nes. *Theory of the Stability of Lyophobic Colloids: The Interaction of Sol Particles Having an Electric Double Layer*. Elsevier Publishing Company, 1948. Google-Books-ID: 0vOcjgEACAAJ.

[96] Peter Walde and Sosaku Ichikawa. Enzymes inside lipid vesicles: preparation, reactivity and applications. *Biomolecular Engineering*, 18(4):143–177, October 2001.

[97] Eric R. Weeks, J. C. Crocker, Andrew C. Levitt, Andrew Schofield, and D. A. Weitz. Three-dimensional direct imaging of structural relaxation near the colloidal glass transition. *Science*, 287(5453):627–631, January 2000.

[98] D. A. Weitz, J. S. Huang, M. Y. Lin, and J. Sung. Limits of the fractal dimension for irreversible kinetic aggregation of gold colloids. *Physical Review Letters*, 54(13):1416–1419, April 1985.

[99] E. Zaccarelli, G. Foffi, K. A. Dawson, S. V. Buldyrev, F. Sciortino, and P. Tartaglia. Confirmation of anomalous dynamical arrest in attractive colloids: A molecular dynamics study. *Physical Review E*, 66(4):041402, October 2002.

[100] Emanuela Zaccarelli. Colloidal gels: equilibrium and non-equilibrium routes. *Journal of Physics: Condensed Matter*, 19(32):323101, July 2007.

[101] Emanuela Zaccarelli, Stefan Andreev, Francesco Sciortino, and David R. Reichman. Numerical investigation of glassy dynamics in low-density systems. *Physical Review Letters*, 100(19):195701, May 2008.

[102] Alessio Zaccone, Daniele Gentili, Hua Wu, Massimo Morbidelli, and Emanuela Del Gado. Shear-driven solidification of dilute colloidal suspensions. *Physical Review Letters*, 106(13):138301, March 2011.

[103] Roseanna N. Zia, Benjamin J. Landrum, and William B. Russel. A micro-mechanical study of coarsening and rheology of colloidal gels: Cage building, cage hopping, and smoluchowski's ratchet. *Journal of Rheology*, 58(5):1121–1157, September 2014.